Air Force Institute of Technology

AFIT Scholar

Theses and Dissertations | Student Graduate Works

12-1994

# Compressible Turbulence Measurements in a Supersonic Boundary Layer Including Favorable Pressure Gradient Effects

Raymond S. Miller

Follow this and additional works at: https://scholar.afit.edu/etd

Part of the Aerodynamics and Fluid Mechanics Commons

## Recommended Citation

Miller, Raymond S., "Compressible Turbulence Measurements in a Supersonic Boundary Layer Including Favorable Pressure Gradient Effects" (1994). *Theses and Dissertations*. 6350.
https://scholar.afit.edu/etd/6350

This Thesis is brought to you for free and open access by the Student Graduate Works at AFIT Scholar. It has been accepted for inclusion in Theses and Dissertations by an authorized administrator of AFIT Scholar. For more information, please contact AFIT.ENWL.Repository@us.af.mil.

DTIC
ELECTE
JAN 05 1995
S G D

19950103 074

# COMPRESSIBLE TURBULENCE MEASUREMENTS IN A SUPERSONIC BOUNDARY LAYER INCLUDING FAVORABLE PRESSURE GRADIENT EFFECTS

THESIS

Raymond S. Miller
Captain, USAF

AFIT/GAE/ENY/94D-19

DEPARTMENT OF THE AIR FORCE
AIR UNIVERSITY
AIR FORCE INSTITUTE OF TECHNOLOGY

Wright-Patterson Air Force Base, Ohio

DISTRIBUTION STATEMENT A
Approved for public release;

AFIT/GAE/ENY/94D-19


| Accesion For | | |
|---|---|---|
| NTIS CRA&I | | ☒ |
| DTIC TAB | | ☐ |
| Unannounced | | ☐ |
| Justification | | |
| By | | |
| Distribution / | | |
| Availability Codes | | |
| Dist | Avail and / or Special | |
| A-1 | | |


# COMPRESSIBLE TURBULENCE MEASUREMENTS IN A SUPERSONIC BOUNDARY LAYER INCLUDING FAVORABLE PRESSURE GRADIENT EFFECTS

THESIS


Raymond S. Miller
Captain, USAF


AFIT/GAE/ENY/94D-19

DTIC QUALITY INSPECTED 3

The views expressed in this thesis are those of the author and do not reflect the official policy or position of the Department of Defense or the U. S. Government.

AFIT/GAE/ENY/94D-19

# COMPRESSIBLE TURBULENCE MEASUREMENTS IN A SUPERSONIC BOUNDARY LAYER INCLUDING FAVORABLE PRESSURE GRADIENT EFFECTS

THESIS

Presented to the Faculty of the School of Engineering

of the Air Force Institute of Technology

Air University

In Partial Fulfillment of the

Requirements for the Degree of

Master of Science in Aeronautical Engineering

Raymond S. Miller, B.S.

Captain, USAF

December 13, 1994

...

The people most important to the completion to an experimental thesis are many. First is always my very supportive wife that has seen me through night school, full time school, and was willing to come back for another bought of the ghost husband. Thank you Connie for the years of unending support that seemed to well up continuously and without which I could not have completed so much.

On the less sentimental note, thanks go to my advisor Maj. Tom Buter, and Dr. Rodney Bowersox for their guidance and knowledge from which I tapped into continuously. I would also like to acknowledge the technical people at AFIT, Andy Pitts particularly, who was always willing to listen, to a new problem, our suggestions, discard them and fix it right. Appreciation goes out to the infamous model shop where all good wind tunnels are built and corrected from the impossible to the manageable. John of the model shop was of particular help in engineering items to make them more useful and simple.

Thank you to all of the other individuals who lent support and tolerated my relentless nagging about it being done yesterday.

*Table of Contents*


| | Page |
|---|---|
| List of Figures | vi |
| List of Tables | xi |
| List of Symbols | xii |
| Abstract | xv |
| I. Introduction | 1-1 |
| 1.1 Motivation | 1-1 |
| 1.2 Objective | 1-4 |
| 1.3 Summary | 1-4 |
| II. Equation Development | 2-1 |
| 2.1 Forms of the Governing Equations | 2-1 |
| 2.2 Modeling Issues | 2-2 |
| 2.3 Turbulence Analysis | 2-3 |
| III. Test Apparatus | 3-1 |
| 3.1 Experimental Facility | 3-1 |
| 3.2 Air Supply | 3-1 |
| 3.3 Test Section Design | 3-1 |
| 3.4 Data Acquisition | 3-4 |
| 3.5 Traversing Equipment | 3-4 |
| 3.6 Shadowgraph and Schlieren Optics | 3-6 |
| 3.7 Pressure Probes | 3-7 |
| 3.8 Temperature Measurement | 3-7 |
| 3.9 Hot Film Probes | 3-8 |

Page

3.10 Computers Used . . . . . 3-11

3.11 Settings . . . . . 3-11

3.12 Error Analysis . . . . . 3-12

3.12.1 Conventional Probes . . . . . 3-12

3.12.2 Hot Wire Probes . . . . . 3-12

IV. Data Reduction . . . . . 4-1

4.1 Use of Shadowgraphs and Schlierens . . . . . 4-1

4.2 Mean Flow Data Reduction . . . . . 4-1

4.3 Hot-Wire Data Reduction . . . . . 4-2

4.3.1 Separation of Turbulence Variables . . . . . 4-8

4.3.2 Single Overheat . . . . . 4-8

4.4 Turbulence Transformation . . . . . 4-10

V. Results and Discussion . . . . . 5-1

5.1 Shadowgraph and Schlieren Photography . . . . . 5-1

5.2 Conventional Data . . . . . 5-2

5.3 Repeatability of Data . . . . . 5-3

5.4 Hot Wire Constants . . . . . 5-4

5.5 Zero Pressure Gradient Region . . . . . 5-10

5.6 Favorable Pressure Gradient Region . . . . . 5-13

5.7 Heat Flux . . . . . 5-18

VI. Conclusions and Recommendations . . . . . 6-1

6.1 Conclusions . . . . . 6-1

6.2 Recommendations . . . . . 6-2

Appendix A. Conventional Probe Data Plots . . . . . A-1

Appendix B. SOH Mean Values . . . . . B-1

Page

Appendix C. SOH Cross Correlations . . . . . C-1

Appendix D. SOH RMS Values . . . . . D-1

Appendix E. Turbulence Intensities and Separated Turbulence Intensities E-1

E.1 Turbulence Intensities . . . . . E-1

E.2 Separated Turbulence Intensities . . . . . E-3

Appendix F. Shear Stress . . . . . F-1

F.1 RANS . . . . . F-1

F.2 FANS . . . . . F-3

F.3 Plots of Cxy . . . . . F-5

Appendix G. Compressible Shear Stress . . . . . G-1

Appendix H. Separated Favré Turbulence Intensities . . . . . H-1

Appendix I. Heat Flux and Related Plots . . . . . I-1

Appendix J. Velocity-Density and Velocity-Velocity Correlations . . . . . J-1

Appendix K. Procedure . . . . . K-1

K.1 Mean Flow Data . . . . . K-1

K.2 SOH Data . . . . . K-1

K.3 MOH Data . . . . . K-3

K.4 Midway . . . . . K-4

K.5 Tables of Favré and Reynolds Shear Terms . . . . . K-6

Bibliography . . . . . BIB-1

Vita . . . . . VITA-1

*List of Figures*


| Figure | | Page |
|---|---|---|
| 3.1. | Wind Tunnel and Computers | 3-2 |
| 3.2. | Wind Tunnel Schematic | 3-2 |
| 3.3. | Wind Tunnel and Computers | 3-2 |
| 3.4. | Test Section Profile | 3-3 |
| 3.5. | Picture of Expansion Ramp | 3-3 |
| 3.6. | UniSlide Model 2500 | 3-4 |
| 3.7. | Traverse Assembly | 3-5 |
| 3.8. | Traverse Assembly | 3-5 |
| 3.9. | Schlieren Camera and Mirror Setups | 3-6 |
| 3.10. | Unstart Condition | 3-8 |
| 3.11. | UV Hot Film Probe, Model 1243-20 | 3-8 |
| 3.12. | UV Hot Film Probe, Model 1243AN-20 | 3-9 |
| 5.1. | Test Section Shlieren Image | 5-1 |
| 5.2. | Test Section Shadowgraph Image | 5-1 |
| 5.3. | Test Section Mach Profile x = 71.5 cm | 5-2 |
| 5.4. | Test Section Pressure Profile $P_{t2}/P_{t\infty}$ x = 71.5 cm | 5-3 |
| 5.5. | Test Section | 5-3 |
| 5.6. | UW RMS Voltage Wire 1(x = 44 cm) | 5-4 |
| 5.7. | UW RMS Voltage Wire 2(x = 44 cm) | 5-5 |
| 5.8. | Mach Profile (x = 44 cm) | 5-5 |
| 5.9. | Shear Stress (x = 44 cm) | 5-6 |
| 5.10. | Hot Wire Mean Voltage(x = 44 cm) | 5-6 |
| 5.11. | Hot Wire Probe Sensitivities | 5-7 |
| 5.12. | UV Probe Turbulence Intensities ($\kappa = 0$ x = 44 cm) | 5-8 |

Figure Page


5.13. UV Probe Turbulence Intensities ($\kappa = .4$ x = 44 cm) . . . . . 5-8

5.14. UV Probe Turbulence Intensities ($\kappa = 1$ x = 44 cm) . . . . . 5-9

5.15. UW Probe Turbulence Intensities ($\kappa = 1$ x = 44 cm) . . . . . 5-9

5.16. UW Probe Turbulence Intensities ($\kappa = 0$ x = 44 cm) . . . . . 5-11

5.17. UV Probe Separated Turbulence Intensities (x = 44 cm) . . . . . 5-11

5.18. UW Probe Separated Turbulence Intensities (x = 44 cm) . . . . . 5-12

5.19. UV Probe Shear (x = 44 cm) . . . . . 5-12

5.20. UW Probe Shear (x = 44 cm) . . . . . 5-14

5.21. UV Probe Turbulence Intensities (x = 71.5 cm) . . . . . 5-14

5.22. UW Probe Turbulence Intensities (x = 71.5 cm) . . . . . 5-15

5.23. UV Probe Separated Turbulence Intensities (x = 71.5 cm) . . . . . 5-15

5.24. UW Probe Separated Turbulence Intensities (x = 71.5 cm) . . . . . 5-16

5.25. UV Probe Shear (x = 71.5 cm) . . . . . 5-16

5.26. UW Probe Shear (x = 71.5 cm) . . . . . 5-19

5.27. UV Probe Shear (x = 44 cm) . . . . . 5-19

5.28. UV Probe Shear (x = 71.5 cm) . . . . . 5-20

5.29. UV Probe Shear (x = 44 cm) . . . . . 5-20

5.30. UW Probe Shear (x = 44 cm) . . . . . 5-21

A.1. Upstream Pressure Profile $P_{t2}/P_{t1}$ x = 44 cm . . . . . A-1

A.2. Test Section Pressure Profile $P_{t2}/P_{t1}$ x = 71.5 cm . . . . . A-1

A.3. Mach Profile (x = 44 cm) . . . . . A-2

A.4. Mach Profile (x = 71.5 cm) . . . . . A-2

B.1. UV Mean Voltage Wire 1(x = 44 cm) . . . . . B-1

B.2. UW Mean Voltage Wire 1(x = 44 cm) . . . . . B-1

B.3. UV Mean Voltage Wire 1(x = 71.5 cm) . . . . . B-2

B.4. UW Mean Voltage Wire 1(x = 71.5 cm) . . . . . B-2

Figure Page


B.5. UV Mean Voltage Wire 2(x = 44 cm) . . . . . B-3

B.6. UW Mean Voltage Wire 2(x = 44 cm) . . . . . B-3

B.7. UV Mean Voltage Wire 2(x = 71.5 cm) . . . . . B-4

B.8. UW Mean Voltage Wire 2(x = 71.5 cm) . . . . . B-4

C.1. UV Cross Correlation Voltage(x = 44cm) . . . . . C-1

C.2. UW Cross Correlation Voltage(x = 44cm) . . . . . C-1

C.3. UV Cross Correlation Voltage(x = 71.5cm) . . . . . C-2

C.4. UW Cross Correlation Voltage(x = 71.5cm) . . . . . C-3

D.1. UV RMS Voltage Wire 1(x = 44 cm) . . . . . D-1

D.2. UW RMS Voltage Wire 1(x = 44 cm) . . . . . D-1

D.3. UV RMS Voltage Wire 1(x = 71.5 cm) . . . . . D-2

D.4. UW RMS Voltage Wire 1(x = 71.5 cm) . . . . . D-2

D.5. UV RMS Voltage Wire 2(x = 44 cm) . . . . . D-3

D.6. UW RMS Voltage Wire 2(x = 44 cm) . . . . . D-3

D.7. UV RMS Voltage Wire 2(x = 71.5 cm) . . . . . D-4

D.8. UW RMS Voltage Wire 2(x = 71.5 cm) . . . . . D-4

E.1. UV Probe Turbulence Intensities (x = 44 cm) . . . . . E-1

E.2. UV Probe Turbulence Intensities (x = 71.5 cm) . . . . . E-1

E.3. UW Probe Turbulence Intensities (x = 44 cm) . . . . . E-2

E.4. UW Probe Turbulence Intensities (x = 71.5 cm) . . . . . E-2

E.5. UV Probe Separated Turbulence Intensities (x = 44 cm) . . . . . E-3

E.6. UV Probe Separated Turbulence Intensities (x = 71.5 cm) . . . . . E-3

E.7. UW Probe Separated Turbulence Intensities (x = 44 cm) . . . . . E-4

E.8. UW Probe Separated Turbulence Intensities (x = 71.5 cm) . . . . . E-4

F.1. UV Probe Shear (x = 44 cm) . . . . . F-1

F.2. UV Probe Shear (x = 71.5 cm) . . . . . F-1

Figure Page


F.3. UW Probe Shear (x = 44 cm) . . . . . F-2

F.4. UW Probe Shear (x = 71.5 cm) . . . . . F-2

F.5. UV Probe Shear (x = 44 cm) . . . . . F-3

F.6. UV Probe Shear (x = 71.5 cm) . . . . . F-3

F.7. UW Probe Shear (x = 44 cm) . . . . . F-4

F.8. UW Probe Shear (x = 71.5 cm) . . . . . F-4

F.9. UV Probe Shear (x = 44 cm) . . . . . F-5

F.10. UV Probe Shear (x = 71.5 cm) . . . . . F-5

F.11. UW Probe Shear (x = 44 cm) . . . . . F-6

F.12. UW Probe Shear (x = 71.5 cm) . . . . . F-6

G.1. UV Probe Shear (x = 44 cm) . . . . . G-1

G.2. UV Probe Shear (x = 71.5 cm) . . . . . G-1

G.3. UW Probe Shear (x = 44 cm) . . . . . G-2

G.4. UW Probe Shear (x = 71.5 cm) . . . . . G-2

H.1. UV Separated Turbulence Intensities (x = 44 cm) . . . . . H-1

H.2. UV Separated Turbulence Intensities (x = 71.5 cm) . . . . . H-1

H.3. UW Separated Turbulence Intensities (x = 44 cm) . . . . . H-2

H.4. UW Separated Turbulence Intensities (x = 71.5 cm) . . . . . H-2

I.1. UV Mass Flux-Total Temperature Correlations (x = 44 cm) . . . . . I-1

I.2. UW Mass Flux-Total Temperature Correlations (x = 44 cm) . . . . . I-1

I.3. UV Specific Turbulent Heat Flux (x = 44 cm) . . . . . I-2

I.4. UW Specific Turbulent Heat Flux (x = 44 cm) . . . . . I-2

J.1. Turbulence Correlations (x = 44 cm) Velocity-Velocity Correlations . . J-1

J.2. Turbulence Correlations (x = 71.5 cm) Velocity-Velocity Correlations . J-1

J.3. UV Probe Turbulence Correlations (x = 44 cm) Velocity-Density Correlations . . . . . J-2

Figure Page

J.4. UW Probe Turbulence Correlations (x = 44 cm) Velocity-Density Correlations . . . . . J-2

J.5. UV Probe Turbulence Correlations (x = 71.5 cm) Velocity-Density Correlations . . . . . J-3

J.6. UW Probe Turbulence Correlations (x = 71.5 cm) Velocity-Density Correlations . . . . . J-3

K.1. UW Probe Turbulence Intensities (x = 53.5 cm) . . . . . K-5

K.2. UW Probe Separated Turbulence Intensities (x = 53.5 cm) . . . . . K-5

K.3. UW Probe Shear (x = 53.5 cm) . . . . . K-7

*List of Tables*


| Table | | Page |
|---|---|---|
| 3.1. | Hot Film Probe Operating Resistance | 3-9 |
| 3.2. | MOH Operating Resistance | 3-10 |
| 3.3. | Approximate System Error | 3-12 |
| K.1. | Favré terms from multiple overheat data | K-6 |
| K.2. | Favré terms from multiple overheat data | K-6 |
| K.3. | Reynolds terms from multiple overheat data | K-7 |
| K.4. | Reynolds terms from multiple overheat data | K-7 |

## *List of Symbols*

| Symbol | |
|---|---|
| $\overline{()}$ | = Reynolds averaged quantity |
| $()'$ | = Reynolds fluctuating quantity |
| $\tilde{()}$ | = Favre averaged quantity |
| $()''$ | = Favre fluctuating quantity |
| $U$ | = Favre averaged velocity |
| $p$ | = pressure |
| $\rho$ | = density |
| $u$ | = x component of velocity |
| $v$ | = y component of velocity |
| $w$ | = z component of velocity |
| $f, g$ | = hot wire sensitivities |
| $\kappa$ | = Strong Reynolds analogy constant |
| $CFD$ | = computational fluid dynamics |
| IFA | = intelligent flow analyzer |
| $MOH$ | = multiple overheat |
| $SOH$ | = single overheat |
| $UV$ | = x-y plane probe data |
| $UW$ | = x-z plane probe data |
| $\tau_{xy}$ | = shear stress in x-y plane |
| $\tau_{xz}$ | = shear stress in x-z plane |
| $\tau_{ij}$ | = shear stress in i-j plane |
| x | = positive in flow direction |
| y | = positive normal to the test section ceiling |
| z | = spanwise third direction of right handed coord. system |
| $m$ | = mass flux |
| $q$ | = heat flux |
| $k$ | = turbulent kinetic energy |
| K | = Kelvin Temperature |

| | |
|---|---|
| C | = Celcius Temperature |
| $e_{\rho u}$ | = mass flux error |
| $e_{Tt}$ | = temperature error |
| $e_f$ | = f sensitivity error |
| $e_g$ | = g sensitivity error |
| $e_{()'()'}$ | = cross-wire shear and total temperature flux correlation error |
| $e_{TI}$ | = turbulence intensity error |
| $e_{p_{t1}}$ | = wind tunnel inflow air pressure |
| $e_{T_{t1}}$ | = wind tunnel inflow air temperature |
| M | = mach number |
| $p_c$ | = cone static pressure |
| $p_{t2}$ | = Pitot probe pressure |
| $p_\infty$ | = stagnation pressure |
| $T_t$ | = total temperature |
| $T_{ref}$ | = reference total temperature |
| $T_w$ | = wire temperature |
| $T_e$ | = equilibrium temperature |
| $T_o$ | = stagnation temperature |
| Pr | = Prandtl number |
| Nu | = Nusselt number |
| $q_w$ | = wire heat transfer |
| $i_w$ | = amperage through wire |
| $V_w$ | = voltage through wire |
| $R_w$ | = resistance of wire |
| $R_s$ | = series resistance of IFA 100 |
| $R_L$ | = lead resistance |
| $R_{ref}$ | = reference resistance |
| $k_t$ | = viscosity |
| $k_o$ | = reference viscosity |
| $\mu_t$ | = thermal conductivity |

| | |
|---|---|
| $\mu_o$ | = reference thermal conductivity |
| $Re_e$ | = effective cooling Reynolds number |
| $Reo_e$ | = effective cooling Reynolds number with $\mu = 0$ |
| $Re_n$ | = normal Reynolds number |
| $Re_t$ | = tangential Reynolds number |
| $Re_x$ | = x-direction Reynolds number |
| $Re_y$ | = y-direction Reynolds number |
| $\phi$ | = incidence angle of cross-wire |
| $\delta$ | = boundary layer thickness |
| $\tau$ | = temperature loading factor |
| L | = length |
| D,d | = diameter |

AFIT/GAE/ENY/94D-19


*Abstract*

The effect of a favorable pressure gradient on the turbulent flow structure in a Mach 2.9 boundary layer ($R_e/m \approx 1.5 \times 10^7$) is investigated experimentally. Conventional flow and hot film measurements of turbulent fluctuation properties have been made upstream of and along an expansion ramp. Upstream measurements were taken in a zero pressure gradient boundary layer 44 cm from the nozzle throat in a 6.35 cm square test section. Measurements are obtained in the boundary layer, above the expansion ramp, 71.5 cm from the nozzle throat. Mean flow and turbulent flow characteristics are measured in all three dimensions. Comparisons are made between data obtained using single and multiple-overheat cross-wire anemometry as well as conventional mean flow probes. Conventional flow measurements were taken using a Pitot probe and a 10 degree cone static probe. Flow visualization was conducted via imaging techniques (Schlieren and shadowgraph photographs). Results suggest that compressibility effects, as seen through the density fluctuations in the Reynolds shear stress are roughly 10% relative to the mean velocity and are large relative to the velocity fluctuations. This is also observed in the total Reynolds shear stress; compressibility accounts for $50 - 75\%$ of the total shear. This is particularly true in the favorable pressure gradient region, where though the peak fluctuation intensities are diminished, the streamwise component of the mean flow is larger, hence the contribution of the compressibility term, $\overline{u}\overline{\rho' v'}$, is significant in the Reynolds shear.

# COMPRESSIBLE TURBULENCE MEASUREMENTS IN A SUPERSONIC BOUNDARY LAYER INCLUDING FAVORABLE PRESSURE GRADIENT EFFECTS

## *I. Introduction*

### *1.1 Motivation*

Given the increasing number of transport and military aircraft designed for supersonic and hypersonic flight, the lack of available supersonic and hypersonic wind tunnel facilities has necessitated heavier use of Computational Fluid Dynamics (CFD) as a means to evaluate system performance. Though CFD techniques have evolved to the point where they provide a significant amount of insight into configuration design, difficulties persist in accurately modeling the turbulent flow present in most high speed situations. In particular, the accurate resolution of turbulence requires sufficient resolution to capture motions on the order of the Kolmogoroff (8) length scales for domains with length scales on the order of complete aircrafts. Simply put, the solution of high speed turbulent flows using the turbulent form of the Navier Stokes equations is beyond the scope of present day computers. White (18) cites the example of a 10 cm thick volume of turbulent flow over a 1.2 m by 2.4 m plate. As the smallest structure of the flow is 0.04 mm, 5 trillion mesh points would be needed to resolve this relatively simple flow. Resolution of the flow is only the first hurdle; there is also the number of operations required to solve turbulence problems. For example, a flow over a cylinder of $Re_D = 10^7$, would require $10^{22}$ numerical operations. A computer capable of one operation per nanosecond would require 320,000 years to complete this calculation! Credible complete solutions of the full set of Navier-Stokes equations have been obtained using a supercomputer on 10 million mesh points, however such calculations are restricted to very low Reynolds numbers, i.e. $Re_\theta = 225$, 300, 670, and 1410 (18). Therefore, these issues preclude the direct solution of the Navier-Stokes equations and dictate that approximate methods be employed.

These approximate methods are typically based upon the solution of an averaged form of the governing equations wherein the dependent variables are cast in terms of a mean and a fluctuation about that mean. The equations are then solved for the mean values of the dependent variables (velocity, pressure, density, etc.) provided a "suitable" closure model representing the fluctuation quantities is introduced. This then is the heart of the turbulence closure problem. The selection of an appropriate model is based not only upon the form of the averaging but also upon the importance of accounting for some or all of the fluctuation quantities. The latter issue has historically been driven by the following considerations: 1) the relative importance of each of the fluctuation terms as determined by experiments and 2) the ease of implementation. The difficulty of describing and analyzing turbulent flows led to the use of many different closure methods applied to two basic formulations of the governing equations; the Reynolds Averaged Navier Stokes (RANS) and the Favré Averaged Navier Stokes (FANS). Closure of these methods typically are developed based upon empirical data and to this degree suffer from a lack of versatility.

Most current compressible turbulent models are extended incompressible formulations and are thus limited in their applicability. Morkovin's hypothesis states that "the turbulence structure is unaffected by compressibility as long as the fluctuation Mach number is much less than unity"(11). A large quantity of work has been based on this hypothesis. However, evidence suggests that these type of models perform poorly for flows with adverse pressure gradients, shock waves and favorable pressure gradients(9). In fact, Morkovin (11) showed that at the Mach number of 1.77, the density-velocity correlations are of the same order as the Reynolds shear stress. The many ad hoc methods employed have only helped to emphasize the difficulty of modeling these types of flows.

The current investigation is aimed at helping to fill a void in the experimental data regarding turbulent interactions in high speed boundary layers having favorable pressure gradients. There currently is very little turbulence data available in the literature for flows of this type (favorable pressure gradient, non-separated supersonic). All data that this researcher found was of gross flow effects. Many studies provided mean flow data with skin friction values, but failed to resolve any of the crucial turbulent components. Lack of resolution of this data limits the usefulness of the majority of the data for judging

the relative importance of the turbulence terms. As the use of computational solutions increases, the need for more accurate models of flow persists. The particular area of interest is the intermediate Mach region (M = 3 - 5) where the flow contains large areas of expansion/shock wave boundary layer interaction. Most of the available empirical data in this flow regime is not of the "building block" variety and thus is not appropriate for turbulence development(6).

The current study investigates the turbulent flow structure over a gradually sloped, favorable pressure gradient surface. More specifically, several terms which appear in the FANS and RANS form of the N-S equations will be measured to provide closure approximations. The lack of quality turbulent data for supersonic flows has caused a great deal of frustration in the aerospace community. Some organizations have gone to great lengths to select the most valuable data and find some criteria to apply so that future experiments would be of value in validating computer models of turbulent flows. As concerns have been raised regarding much of the high-speed experimental turbulence data presently available in the literature, this research was conducted with the criterion established by Settles and Dodson (6) as a guideline. As such, a synopsis of the criteria for experiments suitable for high-speed turbulence model development and validation are given below:

1. *Baseline Applicability:* All candidate studies for use must be experiments involving turbulent flows in either the supersonic or hypersonic Mach number range (i.e., M $\approx$ 3.0 or higher).
2. *Simplicity:* experimental geometries must be sufficiently simple that they may be modeled by CFD methods "without enormous difficulty".
3. *Specific applicability:* All candidate studies passing this criterion must be capable of providing some useful test of turbulence modeling.
4. *Well-defined experimental boundary conditions:* All incoming conditions (especially the state of the incoming boundary layer) be carefully documented. For studies claiming "two-dimensional" flow, data indicating the extent of the spanwise flow variations should be provided.

5. *Well-defined experimental error bounds:* The experimentor must provide an analysis of the accuracy and repeatability of the data, or error bars on the data themselves. Further, error bounds on the data must be substantiated in a quantifiable manner.

6. *Adequate documentation of data:* Data must be documented in a tabulated and machine-readable form.

7. *Adequate spatial resolution of data:* Experiments must present data of sufficiently high resolution, compared with the scale of the flow in question, such that the key features of the flow are clearly resolved.

The geometry of the gradually sloped surface is easily coded; thus it may be readily used for code validation in CFD. By experimentally determining turbulence under more varied experimental conditions, the understanding of the nature of turbulent flows can be expanded leading to more accurate and versatile modeling techniques.

### *1.2 Objective*

The objectives of this thesis are: The identification of the important density-velocity correlations in a supersonic boundary layer with and without a pressure gradient. A secondary objective is to provide a simple geometry test case for CFD model development and validation.

### *1.3 Summary*

Chapter two covers the details regarding the various approximate forms of the governing equations, basic theory pursuant to turbulence modeling. The experimental apparatus is detailed, including the wind tunnel geometries, photographs of test apparatus, test equipment descriptions, probe designs, data acquisition equipment specifications are in chapter three. Chapter four identifies the flow conditions surveyed and provides details regarding flow visualization and error analysis. Chapter five is the presentation of the results showing relative importance of the various turbulent terms. The effect of the pressure gradient is examined. In chapter six conclusions from this work are presented and recommendations for further study outlined.

## *II. Equation Development*

### *2.1 Forms of the Governing Equations*

Computational fluid dynamics (CFD) is playing an ever increasing role in modern supersonic and hypersonic aerodynamics. Turbulent flows are characterized by temporal and spatial scales that range over several orders of magnitude. Direct analytical and numerical solutions to the unsteady N-S equations for turbulent problems of practical interest are highly unlikely in the foreseeable future. Thus, engineers must rely on approximate methods to provide solutions to practical high Reynolds number problems. The two most prevalent approximate methods are the Reynolds time-averaged and Favré mass-weighted-time averaged forms of the N-S equations (RANS and FANS). In either case, additional fluctuation cross-correlation terms due to the nonlinear nature of the N-S equations appear in the averaged form of the equations. Therefore, the averaged systems have more unknowns than equations, requiring that some form of turbulence modeling be employed to close the system. In the past, researchers have often made use of ad hoc assumptions to achieve closure. While these simplified turbulence models do serve a purpose and have had a degree of success, they are inadequate for predictions of compressible flow phenomena such as shock wave-boundary layer interaction and expansion fans (9). For example, the Mach 1.77 expansion fan/boundary layer interaction data of Morkovin (12) suggests that the $\overline{u}\overline{\rho' v'}$ term in the Reynolds shear stress is of the same order as the typical incompressible $\overline{\rho}\overline{u' v'}$ term.

The form of the closure model depends on the type of averaging, FANS or RANS. The Reynolds averaged equations are obtained by un-coupling the instantaneous flow properties into a time average mean value plus a fluctuating turbulent contribution, e.g.,

$$u(x, y, z, t) = \overline{u(x, y, z)} + u'(x, y, z, t)$$

where $\overline{u}$ is the time averaged velocity, and $u'$ is the instantaneous turbulent fluctuating component. The Favré-averaged velocity is given by

$$U = \frac{\overline{\rho u}}{\overline{\rho}}$$

and

$$u = U(x, y, z) + u''(x, y, z, t)$$

where U is the mass-weighted-time averaged mean velocity, and $u''$ is the Favré-averaged turbulent fluctuation. The form of the FANS are very similar in appearance to the *incompressible* RANS. This coupled with Morkovin's hypothesis has led to the current virtually universal trend of adopting the FANS for high speed compressible flows. As a result, practically all compressible turbulence models represent direct extensions of incompressible formulations, where constants are adjusted and the density allowed to vary. Such corrections do little more than correlate the data upon which the models are based (5). The differences between the two averaging methods is very important. For example, by definition the average Reynolds fluctuation is zero; however, the mean Favré fluctuation is non-zero. Care must be taken when comparisons between numerical and experimental results are made. For instance, questions remain as to what type of averaging is inherent to Pitot pressure probes. However, it is clear that cross-wire anemometry responds to time averaged mass fluxes and total temperatures. The present study uses modern, multiple-overheat thermal anemometry to measure the compressible Reynolds data in a Mach 2.9($Re/m = 15 \times 10^6$) boundary layer. Detailed three-dimensional surveys of the Reynolds apparent mass, shear stress, heat flux, and turbulence intensities were obtained. In addition, conventional mean flow probes (Pitot and cone-static) and shadowgraph/schlieren flow visualization were utilized. The data of the present study not only provides insight into the nature of the high-speed compressible pressure gradient turbulence, but also, based on the criteria established by Settles and Dodson (6), serves as excellent CFD validation cases.

### *2.2 Modeling Issues*

The most prevalent methods of applying CFD to compressible turbulent flows utilizes the Favré-averaged form of the N-S equations. Various forms of separation of equations and closure have been applied to simulate turbulence in these equations. With this type of averaging, the density fluctuations are inherently included in the mean Favré velocities,

thus explicit compressibility terms are absent. For example, a paper by Marvin (10) presented the following form for the governing equations:

Continuity:

$$\frac{\partial \overline{\rho}}{\partial t} + \frac{\partial(\overline{\rho}\tilde{u}_i)}{\partial x_i} = 0$$

Momentum:

$$\frac{\partial(\overline{\rho}\tilde{u}_i)}{\partial t} + \frac{\partial(\overline{\rho}\tilde{u}_i\tilde{u}_j)}{\partial x_j} = -\frac{\partial \tilde{p}}{\partial x_i} + \frac{\partial(\overline{\tau}_{ij} - \overline{\rho u_i'' u_j''})}{\partial x_j} \tag{2.1}$$

Energy:

$$\frac{\partial \overline{\rho}\tilde{h}}{\partial t} + \frac{\partial(\overline{\rho}\tilde{h}\tilde{u}_j)}{\partial x_j} = \frac{\partial \tilde{p}}{\partial t} + \tilde{u}_j\frac{\partial \tilde{p}}{\partial x_j} + \overline{u_j''\frac{\partial p}{\partial x_j}} + \frac{\partial(-\overline{q}_j - \overline{\rho h'' u_j''})}{\partial x_j} + \overline{\tau_{ij}\frac{\partial u_i''}{\partial x_j}}$$

Turbulent Kinetic Energy:

$$\frac{\partial(\rho k)}{\partial t} + \frac{\partial(\rho\tilde{u}_j k)}{\partial x_j} = -\overline{\rho u_i'' u_k''}\frac{\partial \tilde{u}_k}{\partial x_k} - \frac{\partial(\overline{\rho u_k'' k})}{\partial x_j} - \frac{\partial(\overline{u_i'' p})}{\partial x_i} + \overline{p\frac{\partial u_i''}{\partial x_i}} + \frac{\partial(\overline{u_i''\tau_{ik}})}{\partial x_k} - \overline{\tau_{ik}\frac{\partial(u_i'')}{\partial x_k}} \tag{2.2}$$

Reynolds stress transport:

$$\begin{aligned}\frac{\partial(\overline{\rho u_i'' u_j''})}{\partial t} + \frac{\partial(\tilde{u}_j\overline{\rho u_i'' u_k''})}{\partial x_j} = {} & (\overline{\rho u_i'' u_j''})\frac{\partial(\tilde{u}_k)}{\partial x_j} - (\overline{\rho u_k'' u_j''})\frac{\partial(\tilde{u}_i)}{\partial x_j} \\ & - \frac{\partial(\overline{\rho u_i'' u_k'' u_j''})}{\partial x_j} - \frac{\partial(\overline{u_i'' p})}{\partial x_j} - \frac{\partial(\overline{u_j'' p})}{\partial x_k} + \overline{p\frac{\partial(u_k'')}{\partial x_i} + \frac{\partial(u_k'')}{\partial x_k}} + \frac{\partial(\overline{u_k''\tau_{ij}})}{\partial x_j} \\ & + \frac{\partial(\overline{u_i''\tau_{ki}})}{\partial x_j} - \overline{\tau_{ij}\frac{\partial(u_k'')}{\partial x_j}} - \overline{\tau_{ki}\frac{\partial(u_i'')}{\partial x_j}}\end{aligned} \tag{2.3}$$

Eqn 2.1 has the same form as the typical incompressible Reynolds averaged N-S equations. Numerical analysts using the Favré-averaged form cite as a benefit the simplification induced by the absence of the fluctuating density-generated terms. The lack of an explicit fluctuating density component in the turbulent shear stresses can be one of the specific shortcomings of this model in that the means by which compressibility effects can be incorporated into a turbulence model is less clear.

### *2.3 Turbulence Analysis*

The compressible, conservative form of the RANS equations, written in Cartesian coordinates are given by

Continuity:

$$\frac{\partial \overline{\rho}}{\partial t} + \frac{\partial(\bar{\rho}\bar{u}_j + \overline{\rho' u'_j})}{\partial x_j} = 0$$

Momentum:

$$\frac{\partial(\bar{\rho}\bar{u}_i + \overline{\rho' u'_i})}{\partial t} + \frac{\partial(\bar{\rho}\bar{u}_i\bar{u}_j)}{\partial x_j} = -\frac{\partial \overline{p}}{\partial x_i} + \frac{\partial(\tau_{ij} + \tau^T_{ij})}{\partial x_j} \tag{2.4}$$

Energy:

$$\frac{\partial(\bar{\rho}\bar{e}_0 + \overline{\rho' h'_0})}{\partial t} + \frac{\partial(\overline{\rho}\overline{h_0}\overline{u_j})}{\partial x_j} = \frac{\partial(\bar{u}_i\bar{\tau}_{ij} + \overline{u'\tau'_{ij}} - q_j - q^T_j)}{\partial x_j}$$

where the compressible RANS turbulence terms or correlations are written as

$$m^T_i = -\overline{\rho' u'_i}$$

$$\tau^T_{ij} = -\overline{\rho}\overline{u'_i u'_j} - \overline{u_i}\overline{\rho' u'_j} - \overline{u_j}\overline{\rho' u'_i} - \overline{\rho' u'_i u'_j} \tag{2.5}$$

$$q^T_i = \overline{\rho}\overline{h'_o u'_i} + \bar{h}_o\overline{\rho' u'_i} + \overline{u_i}\overline{\rho' h'_o} + \overline{\rho' h'_o u'_i}$$

were $e_o$ and $h_o$ are the stagnation conditions (ie., $e_o = e + \frac{1}{2}u_i u_i$) and i,j = x,y or z. The turbulent apparent mass flux ($m^T_i$), turbulent shear stress ($\tau^T_{ij}$), and turbulent heat flux ($q^T_i$) are associated with the continuity, momentum and energy equations, respectively. For incompressible flows, the apparent mass and the last three terms in the shear stress and heat flux are zero.

Note that the compressible FANS turbulence terms are expressed as

$$m''_i = 0$$

$$\tau''_{ij} = -\overline{\rho u''_i u''_j} \tag{2.6}$$

$$q''_i = \overline{\rho h''_o u''_i}$$

As previously noted, the Favré averaged terms are similar in appearance to those of the incompressible Reynolds averaged equations. Bowersox and Schetz (4) have shown that cross-wire anemometry is well suited for measurement of RANS turbulent terms. In particular, they have shown that the total shear stress can be directly measured for thin

layer type flows. Further, if the effects of the pressure fluctuations on the hot-wire response are small, then the multiple overheat cross-wire results can be decomposed into all of the terms in equation (5). This assumption has been verified by Bowersox and Schetz (4) for a Mach 4.0 free mixing layer, and Kistler (7) suggested this is valid for supersonic boundary layers up to Mach 4.7.

# III. Test Apparatus

## 3.1 Experimental Facility

The present experimental work was performed in the AFIT Supersonic Wind Tunnel Facility, see Figure 3.1 and the schematic in Figure 3.2 for the picture of the AFIT Supersonic Facility. The wind tunnel is a combination blow-down and draw-down facility.

## 3.2 Air Supply

The mass flow capacity of the Atlas Compco brand compressor facility is approximately 0.45 kg/sec. The system passes its air through two Pioneer Air Systems Inc. model R500A refrigeration-type air dryers, a centrifugal moisture and particle separator and a filament-reinforced paper filter before entering the wind tunnel. The tank capacity of the vacuum system is approximately 20 cubic meters. The three vacuum pumps are manufactured by Stokes Penwalt, model 212-11 MicoVac pumps. They are powered by 7.6 metric hp Reliance electrical motors, Figure 3.3.

## 3.3 Test Section Design

The test section of the wind tunnel is 6.35 cm by 6.35 cm. The test section, diffuser and nozzle are all constructed from 1.905 cm thick aluminum alloy. The test section side walls are constructed of 1.905 cm thick optical grade Plexiglas, to allow for photographic analysis of the flow. The overall test section is of a modular design. Each of the four sections are 33.02 cm long with rubber gaskets on one end joining sections together. (Hex-headed bolts were used for the Plexiglas of the test section, instead of standard screws, to prevent tool slippage and marring the Plexiglas finish). High vacuum grease was used on the gaskets and sealing surfaces. Side plate bolt holes of the test sections were drilled oversized 0.8 mm. The oversized holes allow the adjustment of the floor and ceiling to minimize unwanted upstream shocks due to misaligned interconnection seams. This also allowed for some adjustment, side to side, of the wind tunnel walls, which minimized discontinuities in the wall seams. Modeling clay was used as necessary to block the remaining seam leakage.

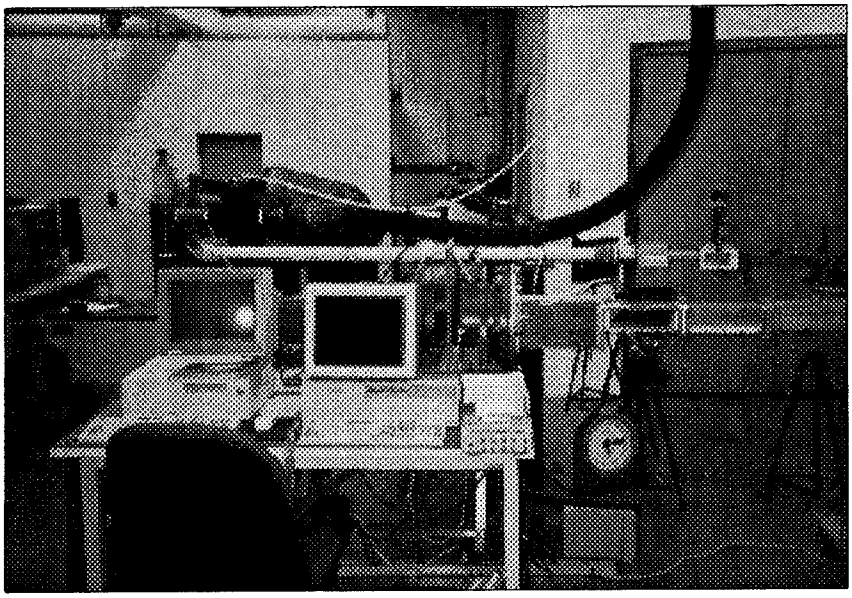

Figure 3.1 Wind Tunnel and Computers

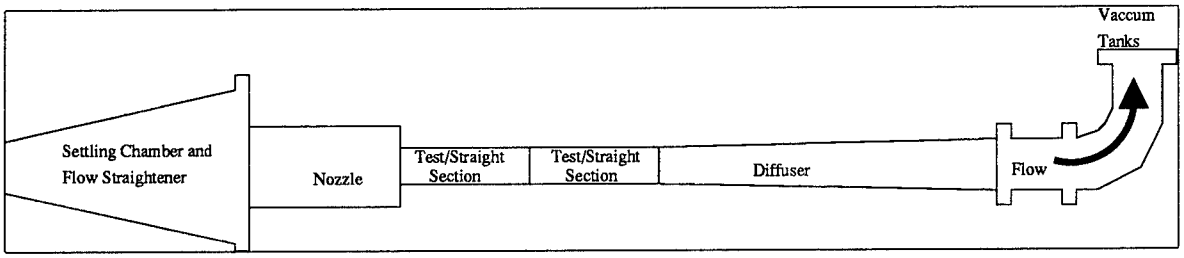


Figure 3.2 Wind Tunnel Schematic

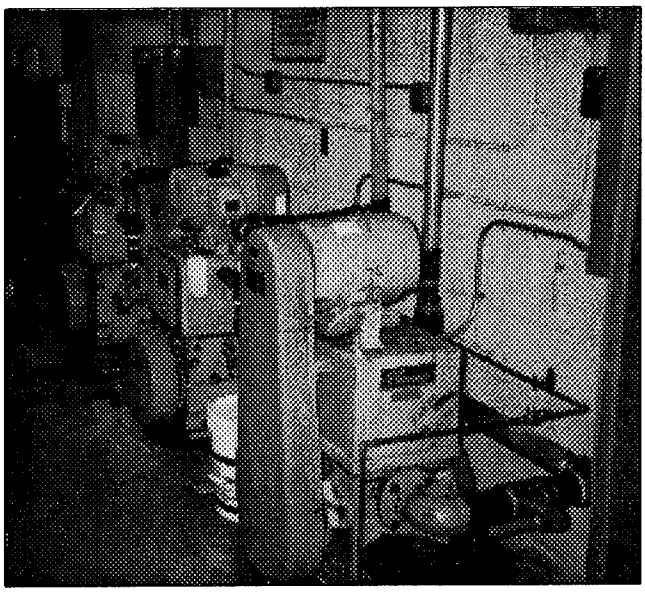

Figure 3.3 Wind Tunnel and Computers

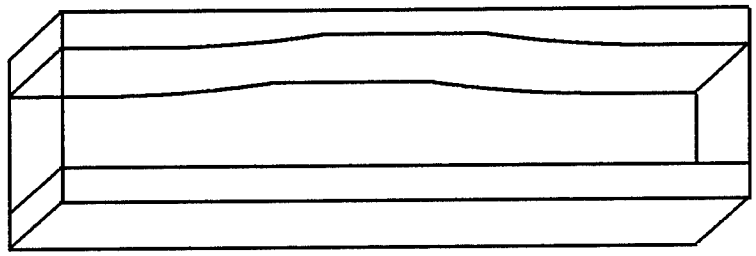

Figure 3.4 Test Section Profile

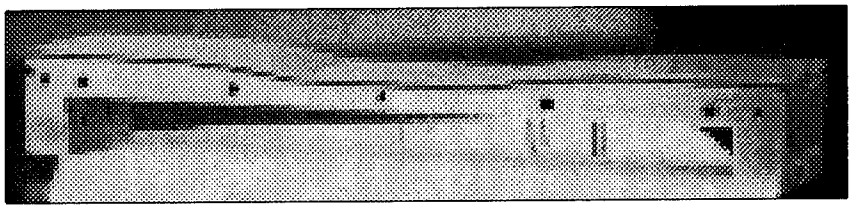

Figure 3.5 Picture of Expansion Ramp

The expansion ramp portion of the test section geometry is a recessed ceiling shown in Figures 3.4 and 3.5.

A gradual slope is used to provides a favorable pressure gradient region while avoiding flow separation. The approximate slope of the design is a one degree change in slope every 0.8467 cm. The test section contour matches the curve fit:

$$Y = 2.54 * (a_o + a_1(x/2.54) + a_2(x/2.54)^2 + a_3(x/2.54)^3) \tag{3.1}$$

where $a_0 = -0.0818011, a_1 = 0.0897045, a_2 = -0.0240686$, and $a_4 = -0.000232096$. This curve fit has a standard deviation of 0.00081 cm and $x$ and $Y$ are in cm. The $x$ coordinate is measured from the beginning of the contour.

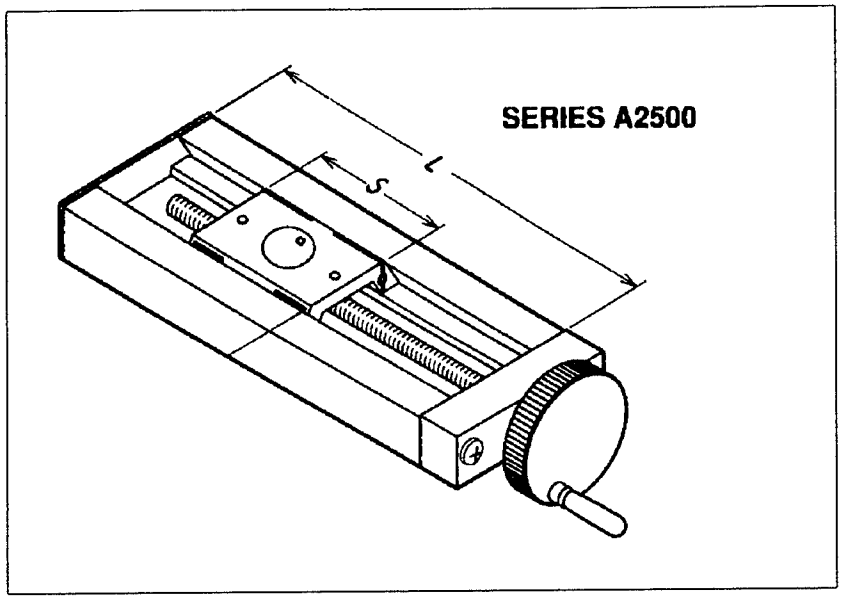


Figure 3.6 UniSlide Model 2500

### *3.4 Data Acquisition*

Instrumentation for the wind tunnel is attached to a Multipro data acquisition system manufactured by Nicolet Instrument Corp. The Multipro has four model 120 data acquisition boards installed with 1 megabyte of memory per board. Bus triggering was used on the Multipro to assure data acquisition synchronization.

### *3.5 Traversing Equipment*

The stepper motor used is a MD-2 with 400 steps per revolution. The probe traverse slide is made by UniSlide and has a total travel distance of 16.51 cm. The slide moves on a shaft of 40 threads per 2.54 cm. The Figure 3.6 shows the schematic of the unit, S is 6.35 cm and L is 22.86 cm. A picture of the traversing assembly is provided in Figures 3.7 and 3.8. The hand cranks in the Figures provide manual control of horizontal and vertical alignment. The maximum speed of the MD-2 is approximately 0.25cm/sec. The circular plate is used to vary the angle of the probe traversing the flow so that it remains perpendicular to the surface of interest. The LVDT (Linear Voltage Displacement Transducer) used is TRANS TEK model 0217-0000 F-90 (Not Shown). The power supply for the LVDT is a Hewlett Packard 6205C. Traverse control was accomplished using a

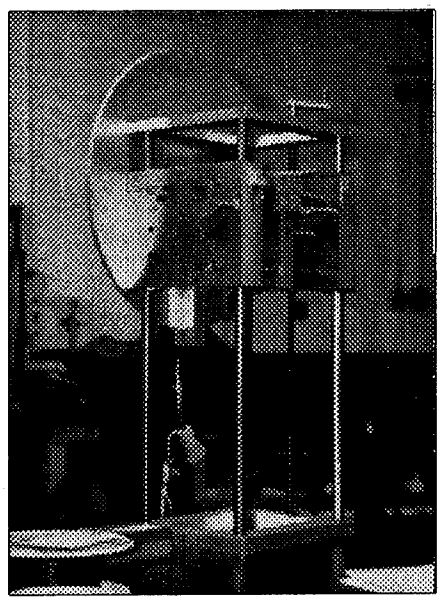

Figure 3.7 Traverse Assembly

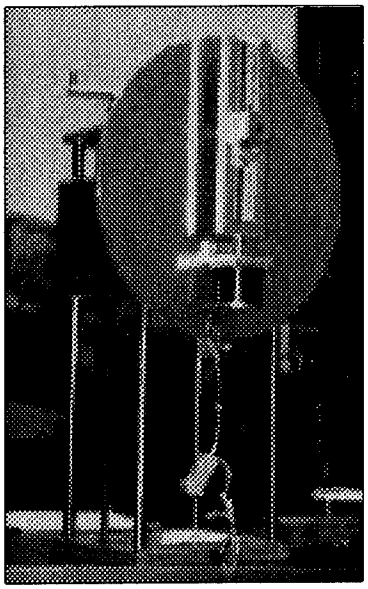

Figure 3.8 Traverse Assembly

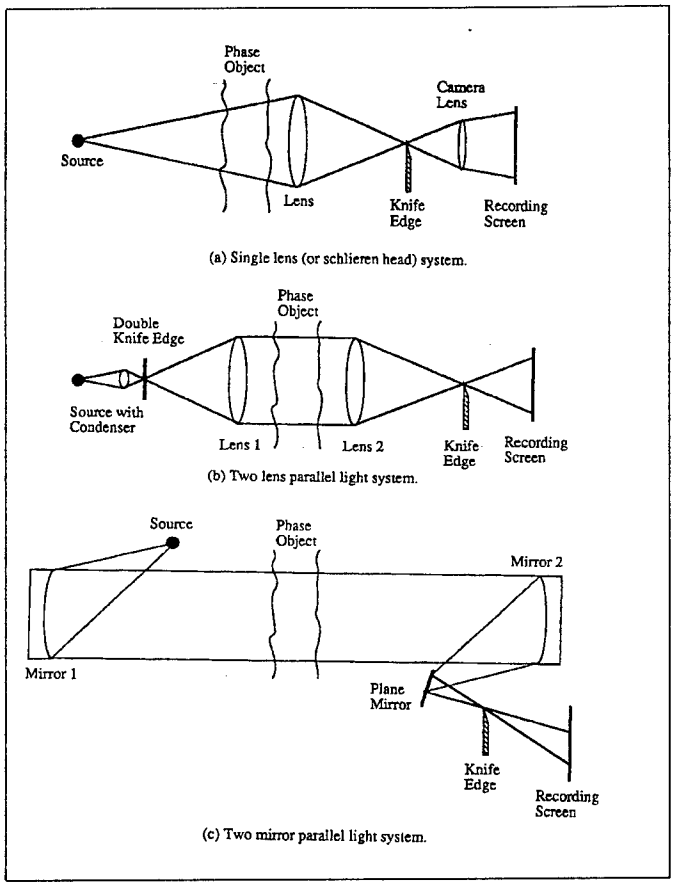


Figure 3.9 Schlieren Camera and Mirror Setups

Zenith 386 computer. Linking of the traverse equipment to trigger the data acquisition allows accurate location versus data tracking.

### *3.6 Shadowgraph and Schlieren Optics*

The shadowgraphs were acquired using an arc light source made by Cordin model 5401 with a spark duration of 600 nanoseconds. The light is reflected from a 101.6 cm focal length mirror and photographed with series 52 Polaroid film. The schlierens used the same light source but used an additional mirror and knife edge to split the incoming light to the film. The diagrams for the schlieren layout are provided in Figure 3.9c.

### *3.7 Pressure Probes*

Measurement of the $P_{t\infty}$ and $T_{t\infty}$ are accomplished using Pitot tube and thermocouple located upstream of the nozzle in the settling chamber. Mean flow in the test section is acquired by the use of a Pitot tube to obtain the total pressure ($P_{t2}$), and conical probe for the static pressure ($P_c$). For most of the test runs signal filtering for the pressure transducers were passed through an ENDEVCO model 4225 signal conditioner before passing into the Multipro. During the multiple overheat runs the pressure transducers are connected to an ENDEVCO Model 4428A signal processor and calibrator. This unit uses the maximum range of the pressure transducer and spreads the range of response linearly over 5 volts. The unit is self-zeroing and connects directly to the Multipro. The pressure transducers documentation assures that accuracy is below a maximum error of 0.5% of full scale and guarantees linear behavior. A 1.0206 atm transducer is used for the Pitot and cone static probes with an $\pm$ 0.0051 atm error. The upstream transducer, 6.804 atm, has a error $\pm$ 0.017 atm. Atmospheric pressure is recorded using a Tranamerica Delaval digital barometer model number 2500-0101.

The conventional probes, Pitot and cone-static, are both machined from stainless steel and are curved to the same approximate length as the hot wire probes. The length is matched so that the data taken would be as close as possible to the same streamwise location. The original 0.64 cm diameter probe holder created excessive blockage causing the tunnel to unstart, Figure 3.10. This probe effectively blocked off more than 8.0% of the flow. This lead to the development of a variable diffuser and a smaller probe holder (0.3175 cm diameter). The smaller size was still rigid enough to minimize deflections of the probe yet not choke the flow.

### *3.8 Temperature Measurement*

The temperature transducer used is made by Omega Engineering, Incorporated and is part number SEFE-K-5 and has an accuracy of $\pm 1°$ K (15). The transducer is connected to a temperature display, also made by Omega, the Digicator model.

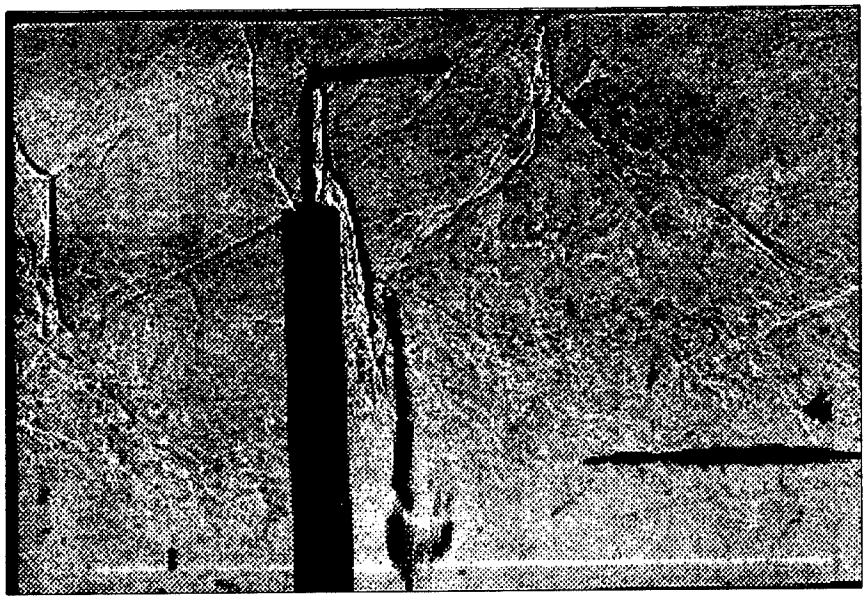

Figure 3.10 Unstart Condition

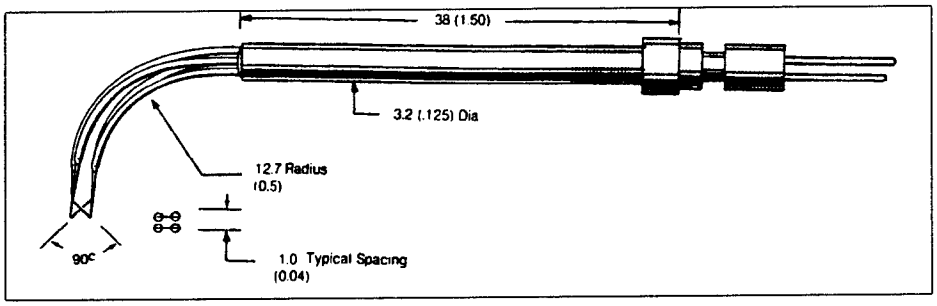


Figure 3.11 UV Hot Film Probe, Model 1243-20

### *3.9 Hot Film Probes*

The cross wire probes used are TSI brand, model 1243-20 and 1243AN-20 with a platinum hot film (Figures 3.11 and 3.12). The coefficient of resistance is $0.24\%/°C$. They are connected to a TSI brand IFA Intelligent Flow Analyzer 100 with internal bus resistance of 50 ohms. A Tektronix 2454B oscilloscope is used to view and tune the frequency response shape of the probe. A list of resistances of the probes is given in Table 3.1, where (R) stands for repaired probe.

For multiple overheat work an external resistor setup is used which is similar to the one outlined by Bowersox (2). The LVDT power light is wired to trigger a Wavetek model 278 function signal generator. This in turn set the cycling frequency of the resistors

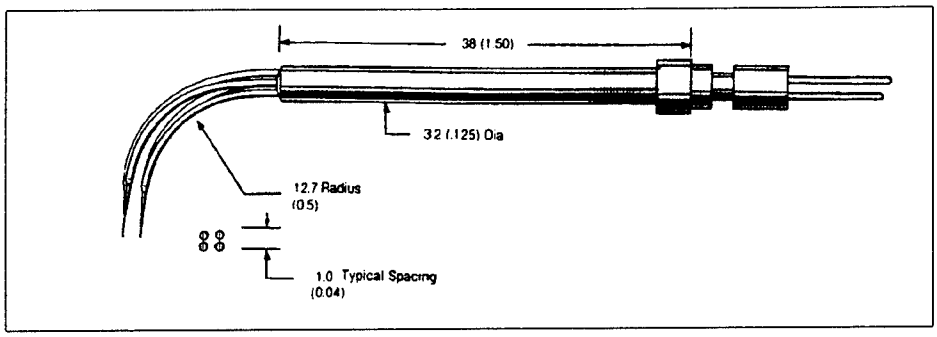


Figure 3.12 UV Hot Film Probe, Model 1243AN-20

Table 3.1 Hot Film Probe Operating Resistance

| Probe type | *S/N* | Channel 1 | Channel 2 |
|---|---|---|---|
| 1243AN | 944012 | 4.80 | 4.78 |
| 1243AN | 944010 | 4.80 | 4.73 |
| 1243AN(R) | 944012 | 5.608 | 5.031 |
| 1243 | 943011 | 5.19 | 5.21 |
| 1243 | 943009 | 6.48 | 6.25 |
| 1243 | 943008 | 6.44 | 6.34 |

at 4 Hz. Single overheat (SOH) measurements were obtained from a 1:1 bridge using an external resistor to set the overheat level. A resistor of 10 ohms was used. When tested for accuracy, the two resistors used measured as 10.000 ohms. Cable resistance was measured at 0.4 ohms. Thus, the total overheat was based on 10.4 ohm total resistance. This level of resistance was above that listed in any of the probe literature. The higher overheat resistance gives a more accurate response to mass flux and thus less susceptible to temperature fluctuations. TSI recommended overheat is estimated at approximately 1.6. The SOH for this investigation, range between 1.6 and 2.2. The external resistance used for the multiple overheat (MOH) is listed in Table 3.2, all values in Tables 3.2 and 3.1 must have 0.4 Ohms added to them to get accurate overheat ratios.

The tuning of the frequency response is the most difficult part of hot wire usage. The probes have to be tuned at or near test conditions. The only available test source is the tunnel itself, which only has a usable run time of 20 to 25 seconds. Tuning each channel took about one day. The consistency of the channel response was verified multiple times,

Table 3.2 MOH Operating Resistance

| Overheat No. | Resistance |
|---|---|
| 1 | 10.000 |
| 2 | 9.524 |
| 3 | 9.091 |
| 4 | 8.750 |
| 5 | 8.333 |
| 6 | 7.778 |
| 7 | 7.500 |
| 8 | 7.143 |

especially when switching from the UV to the UW probes. Channel 1 bridge compensation was set to 1340 and channel 2 was set to 740.

During single overheat runs the data acquisition is triggered by the sharp increase in tunnel pressure at start. The pressurization of the wind tunnel is the last event before the IFA is started and the traverse is started across the flow. Using this single event to trigger the other channels for data collection, the LVDT, upstream pressure, and two channels for the hot wire, all are simultaneous. Data was manipulated in groups of 1024 points for the SOH. Details regarding the operating procedures for the facility are contained in Appendix J. MOH anemometry is more fatiguing on the hot wire probes. The higher overheat ratios and the cycling of overheat ratios are more detrimental to the survival of the hot wire. The short run time of the tunnel necessitates a very quick cycling of the overheat ratios. The circuit outlined in Bowersox (2) is used to cycle the overheat ratios. Samples are taken while the traverse pauses for three seconds in even increments as it traveled through the boundary layer. The trigger for data acquisition in this case is the traverse stopping. This event triggers the the Wavetek signal generator which cycled the resistors at a 4 Hz cycle speed through the multiple overheat circuit. The sampling rate of the Multipro is set at 10 kHz. As a result, it captures 2500 data points for each overheat. Of these data points, approximately 2056 centered over the sample time were used. The remaining points were neglected to eliminate any transients due to scanning.

### *3.10 Computers Used*

Data is stored on a Compaq 386/25m, and a Zenith 486. The traverse equipment is run from a Zenith 386. The data reduction is done on an Amiga 2000 and on Sun Sparc 20's. The Amiga is used for the conventional probe mean flow pressure data breakdown. The Sparc 20's are used for all other data analysis.

### *3.11 Settings*

A pressure of approximately 1.5 atm (to achieve two atmospheres in the wind tunnel due to back pressure losses) is used as an air source and is exhausted into an evacuated tank, initially drawn down to approximately 18 mm of mercury absolute. The vacuum system initially takes 15 minutes to draw down, and then subsequent runs take from 8 to 10 minutes to draw down. The compressor facility had no problems keeping up with the demand.

The traverse equipment speed has a range of speeds from 0 to 32000, 0 being the fastest. Speeds faster than 370 are not used due to system response losses. For the conventional probe usage the speed is set at 1200, which corresponds to .127 cm/sec. As the hot wire data is sampled at a higher rate, the traversed speed is increased to 370, leading to a speed of .254 cm/sec. The multiple overheat runs are restricted to the first 1.27 cm of the boundary layer due to the need to stop and sample at each location for three seconds. Samples are taken every 0.254 cm for the multiple overheat data.

The sampling rate of the Nicolet Multipro is set to 200 Hz for the sampling of the conventional probes. The sampling rate for the hot-wire probes is set to 10 kHz.

The frequency of the sampling rate was also a major concern. The frequency of 10 kHz was chosen to capture the overall energy of the flow. The signal was not filtered and a spectral analysis was not necessary for the current study and the energy of the flow could be captured without resolving where the frequency of the energy originated. Based on the work of Smits and Muck (14), the energy spectra range of our sampling should be able to capture the flow character very well.

### 3.12 Error Analysis

Based on the analysis presented in (2) a Euclidean (or $L_2$) norm are presented as measures of the error. The $L_2$ norm is given by

$$e_x = \left[\sum_{i=1}^{n} e_i^2\right]^{\frac{1}{2}} \tag{3.2}$$

where i indexes the various errors associated with measurement x.

*3.12.1 Conventional Probes.* Volluz (17) reports that turbulence induces about $\pm 0.0068$ atm error for both probe types, Pitot and cone static. The calibration error $e_{p_{ts}}$=0.005 atm is for both probes. Upstream pressure has an error of $e_{p_{t1}}$=0.017 atm. The temperature error is $e_{T_{t1}} = 1°$ K

The probe location errors are estimated as $\pm 0.5\%$. Therefore, the error in the Mach number at M = 2.9 is approximately $\pm 0.1$ or $\pm 3\%$, respectively. The error in the local mean mass flux is $\pm 2.0\%$.

*3.12.2 Hot Wire Probes.* The linearizations errors have been shown by Bowersox (2) to be negligible compared to the above mentioned calibration errors. Perturbation analysis also shows that probe misalignment errors are very small, primarily due to the procedure of re-calibrating the probes at each new station and thereby accounting for any misalignment. The following errors were documented for this equation model in Table 3.3. Where $e_{\rho u}$ is the mass flux error, $e_{Tt}$ is the temperature error, $e_f$ is the f sensitivity error,

Table 3.3 Approximate System Error

| Identifier | Percentage |
|---|---|
| $e_{\rho u}$ | 2.0 |
| $e_{Tt}$ | 0.3 |
| $e_f$ | 1.0 |
| $e_g$ | 0.3 |
| $e_{()'()'}$ | 8.33 |
| $e_{TI}$ | 4.17 |

$e_g$ is the g sensitivity error, $e_{()'()'}$ errors for the cross-wire shear and total temperature

flux correlation terms, and $e_{TI}$ is the error of the turbulence intensities. Based upon the analysis presented in reference (2). This results in a total hot wire error of 8.5%.

# *IV. Data Reduction*

## *4.1 Use of Shadowgraphs and Schlierens*

Shadowgraphs and schlieren photographs were taken to afford examination of some general flow characteristics. From these photographs the boundary layer thickness was estimated to be 1.25 cm thick at x = 59 cm (before the expansion). The thickness of the boundary layer over the expansion ramp was estimated as 1.9 cm at x = 75 cm (at the end of expansion ramp). No separation was observed, thus all probes use were angled (i.e. perpendicular to the surface) assuming that the flow followed the contour of the wall within the boundary layer.

## *4.2 Mean Flow Data Reduction*

A least squares curve fit for the solution of the Mach number from the ratio of the pressure obtained from a 10° axisymmetric cone and a Pitot probe (2) is given by:

$$\frac{1}{M} = -0.052976 + 4.6840x - 18.678x^2 + 50.7006x^3 - 54.1577x^4 \tag{4.1}$$

where x represents $P_c/P_{t2}$ to calculate the Mach number and is good in the Mach number range from 1.5 to 4.4. The curve fit has a standard deviation of 0.0006. The remaining flow properties were computed from the typical compressible gas dynamic relations (1). The data from the conventional probes is processed primarily on an Amiga 2000 running at 28 MHz. Data points were averaged together in groups of 100. Data obtained using the Pitot probe is obtained closer to the surface than that garnered using the cone-static probe. The cone static probe data is extrapolated using a third degree polynomial curve fit. To match the data, procedures for interpolation and extrapolation are used from "Numerical Recipes in C"(13). This process adds two points to the Mach number profile near the wall. The lowest data point for the hot wire data is lower than the lowest cone static probe data. The extrapolation of the cone static data below the cross wire data proved invaluable. Approximately 10-12 data points in the hot film data were added by this small addition of the first of these two points in the conventional data (the lowest point is not used for

the hot wire data analysis). The profiles for the upstream test location were done with multiple passes to insure repeatability from one run to the next.

### *4.3 Hot-Wire Data Reduction*

Hot film measurements are obtained at each station. Because of the fragility of the probes, the second run at a given station is usually the calibration run. All hot wire measurements, UV and UW, are taken for a set configuration assembly to remove anomalies induced by configuration changes. Single overheat (SOH) and multiple overheat (MOH) measurements were obtained. Eight overheat ratios were employed at each MOH point, but in most cases the six higher ratios are used to reduce the data. Lower overheat ratios are less sensitive to mass flux fluctuations and will sometimes become oscillatory, rendering their response meaningless. The oscillatory behavior increases as the wire temperature approaches the flow total temperature. The multiple overheat cross-wire data reduction techniques developed in Bowersox (2) and Bowersox and Schetz (4) were used in the present study. A summary of their basic formulation is presented in this Section. Multiple overheat cross-wire anemometry in supersonic flow provides the following "conservative" variable turbulence data

$$\overline{(\rho u_i)'(\rho u_j)'}, \quad \overline{T_t'^2}, \quad \overline{(\rho u_i)'T_t'}$$

The basic form of a hot wire is a cylinder and the form of the Nusselt number for compressible flow in dimensionless heat transfer is:

$$Nu = F(L/d, M, Pr, Re_e, \tau) \tag{4.2}$$

L/d is the wire aspect ratio; M is the Mach number; Pr is the Prandtl Number; $Re_e$ is the effective cooling Reynolds number (base on wire diameter); and $\tau$ is the temperature loading factor. The temperature loading factor can be expressed as $\tau = (T_w - T_e)/T_t$ where $T_w$ is the wire temperature are $T_e$ the temperature the unheated wire would attain if placed in the flow, called the equilibrium temperature. For Reynolds numbers greater than about 20, $T_e$ is about 97% of $T_t$. When the Mach number normal to the wire is greater than 1.2, or $M sin\phi \geq 1$; Pr is constant; and the aspect ratio $\gg 1$, the function for the Nusselt

number becomes:

$$Nu = f(Re_e, \tau) \tag{4.3}$$

Following the assumptions and development of Bowersox and Schetz (4)

$$Nu = a\sqrt{Re_e} + b \tag{4.4}$$

and equal to

$$Nu = \frac{q_w}{\pi k_t L(T_w - T_t)} \tag{4.5}$$

where $q_w = {i_w}^2 R_w$ and $i_w = V_w/(R_w + R_s + R_L)$ from anemometer circuit analysis. Assuming $T_e = T_t$ this equation reduces to

$$Nu = \frac{{V_w}^2 R_w}{(R_w + R_s + R_L)^2} \frac{1}{\pi k_t L(T_w - T_t)} \tag{4.6}$$

The power laws for viscosity and thermal conductivity were used

$$k_t = k_o \left(\frac{T_t}{T_o}\right)^{n_k} \; and \; \mu_t = \mu_o \left(\frac{T_t}{T_o}\right)^{n_\mu} \tag{4.7}$$

with $n_\mu = 0.77$ and $n_k = 0.89$ (2). Combining the previous equations, the hot wire response equation is

$$\frac{{V_w}^2}{C_o} = \left(\frac{T_t}{T_o}\right)^{n_k} \left[a\sqrt{Reo_e}\,(T_t/T_o)^{-n_\mu/2} + b\right](T_w - T_t) \tag{4.8}$$

$Reo_e$ is the effective Reynolds number with $\mu = \mu_o$, and

$$C_o = \frac{(R_w + R_s + R_L)^2}{R_w} \pi L k_o \tag{4.9}$$

Replacing $V_w$, $Reo_e$, and $T_t$ by their mean plus fluctuating components, using the binomial theorem, retaining only the first order terms, and noting that

$$\frac{\overline{V_w}^2}{C_o} = \left(\frac{\overline{T_t}}{T_o}\right)^{n_k} \left[a\sqrt{\overline{Reo_e}} + b\right](T_w - \overline{T_t}) \tag{4.10}$$

then solving for $V_w'/\overline{V_w}$, the hot wire fluctuation equation is derived in the form

$$\frac{V_w'}{\overline{V_w}} = f\left(\frac{Reo_e{}'}{\overline{Reo_e}}\right) + g\left(\frac{T_t{}'}{\overline{T_t}}\right) \tag{4.11}$$

and the hot wire sensitivities are

$$f = \frac{1}{4}\left(1 + \frac{b}{a\sqrt{\overline{Re_e}}}\right)^{-1} \quad and\ g = \frac{-\overline{T_t}}{2(T_w - \overline{T_t})} + \frac{n_k}{2} - fn_\mu \tag{4.12}$$

Rewriting equation 4.8

$$\sqrt{\overline{Re_e}} + x_i\overline{T_t}\sqrt{\overline{Re_e}} + y_i\overline{T_t} = z_i \tag{4.13}$$

where $x_i = -1/T_{wi}$, $y_i = -b_i/(a_iT_{wi})$, and $z_i = \overline{V_{wi}}^2/(C_ia_iT_{wi}) - b_i/a_i$. C is $C_o$ and $k_o$ is $k_t$. The subscript i indexes over the overheat ratios. At a minimum two wire overheats are needed to solve for the unknowns $\sqrt{\overline{Re_e}}$ and $\overline{T_t}$. If more overheats are available a least squares analysis is used (2).

$$\begin{gathered} N\sqrt{\overline{Re_e}} + \overline{T_t}(\sum y_i - \sum x_iz_i) + 2\overline{T_t}\sqrt{\overline{Re_e}}\sum x_i + \\ \overline{T_t}^2\sum x_iy_i + \overline{T_t}^2\sqrt{\overline{Re_e}}\sum x^2{}_i = \sum z_i \end{gathered} \tag{4.14}$$

$$\begin{gathered} \sqrt{\overline{Re_e}}(\sum y_i - \sum x_iz_i) + \overline{T_t}\sum y_i^2 + 2\overline{T_t}\sqrt{\overline{Re_e}}\sum x_iy_i + \sqrt{\overline{Re_e}}^2\sum x_i \\ +\overline{T_t}\sqrt{\overline{Re_e}}^2\sum x_i^2 = \sum y_iz_i \end{gathered} \tag{4.15}$$

N represents the number of overheat ratios. Summations cover the i overheat ratios. The solution was reached iteratively using the secant method. Squaring and averaging equation (4.11) yields

$$f_i{}^2\overline{\left(\frac{Reo_e{}'}{\overline{Reo_e}}\right)^2} + 2f_ig_i\overline{\left(\frac{Reo_e{}'}{\overline{Reo_e}}\frac{T_t{}'}{\overline{T_t}}\right)} + g_i{}^2\overline{\left(\frac{T_t{}'}{\overline{T_t}}\right)^2} = \overline{\left(\frac{V_w'}{\overline{V_w}}\right)_i^2} \tag{4.16}$$

Three overheat ratios are required to solve this equation. If more overheat ratios are available a least squares approach is employed. The method used for solution of this problem is Quadratic Least Squares (QLS). It assumes that the errors in the hot-wires are purely random and all bias resides in f and g. Therefore, the new wire temperature loading

factor is

$$\tau^* = \frac{(T_w - \overline{T_t})}{\overline{T_t}} \tag{4.17}$$

and the new sensitivities can be expressed as

$$f = f_o + m_f \frac{1}{\tau^*}$$

$$g = g_o + m_g \frac{1}{\tau^*} \tag{4.18}$$

where $f_o$ and $m_f$ are determined from wire calibration and $g_o = n_k/2 - f_o n_\mu$, $m_g = -(.5 + n_\mu m_f)$.

Through extensive manipulation of variable and constants, a three by three system of equations results

$$\overline{\left(\frac{V'_w}{\overline{V_w}}\right)^2} = a_o + a_1\left(\frac{1}{\tau^*}\right) + a_2\left(\frac{1}{\tau^*}\right)^2 \tag{4.19}$$

$$\begin{bmatrix} {f_o}^2 & 2f_o g_o & {g_o}^2 \\ 2f_o m_f & 2(f_o m_g + g_o m_f) & 2g_o m_g \\ {m_f}^2 & 2m_f m_g & {m_g}^2 \end{bmatrix} \begin{pmatrix} \overline{\left(\frac{Reo_e'}{\overline{Reo_e}}\right)^2} \\ \overline{\left(\frac{Reo_e'}{\overline{Reo_e}}\frac{T_t'}{\overline{T_t}}\right)} \\ \overline{\left(\frac{T_t'}{\overline{T_t}}\right)^2} \end{pmatrix} = \begin{pmatrix} a_o \\ a_1 \\ a_2 \end{pmatrix} \tag{4.20}$$

and the temperature is calculated using

$$T_w = T_{ref} + \frac{100}{\gamma_{ref} R_{ref}}(R_w - R_{ref}) + 273.15 \tag{4.21}$$

The response of the cross wires are independent of Mach number as long as $M\sin(\phi) \geq 1$, but they are still dependent on the normal component of the Reynolds number. To derive the formulas for analysis, the effective Reynolds number must be used in the x and y coordinate system and related to oblique shock theory.

$$\begin{pmatrix} Re_n \\ Re_t \end{pmatrix} = \begin{bmatrix} \cos(\phi) & \sin(\phi) \\ -\sin(\phi) & \cos(\phi) \end{bmatrix} \begin{pmatrix} Re_x \\ Re_y \end{pmatrix} \tag{4.22}$$

$$Re_e{}^2 = Re_n{}^2 + k_c{}^2 Re_t{}^2 = A_1 Re_x{}^2 + 2A_2 Re_x Re_y + A_3 Re_y{}^2 \tag{4.23}$$

where $A_i$ are given by

$$\begin{aligned} A_1 &= \cos^2(\phi) + k_c{}^2 \sin^2(\phi) \\ A_2 &= (1 - k_c{}^2)\cos(\phi)\sin(\phi) \\ A_3 &= k_c{}^2 \cos^2(\phi) + \sin^2(\phi) \end{aligned} \tag{4.24}$$

and $\phi$ is the incidence angle of the hot wire to the flow. Using first order assumptions $k_c$ can be shown to be (2)

$$k_c = \frac{\overline{\rho_1}}{\overline{\rho_2}} k \tag{4.25}$$

where $k$ = f(L/d)

$$Re_{t2} = \frac{\rho_2}{\rho_1} Re_{t1} \tag{4.26}$$

the subscript "1" refers to the condition just prior to the oblique shock, "2" refers to the condition after the shock and $k$ is to be determined experimentally from the calibration data.

Replacing $Reo_e$, $Reo_x$ and $Reo_y$ by their mean fluctuating components and applying the binomial theorem and using

$$\begin{aligned} R_o &\equiv \frac{\overline{Reo_y}}{\overline{Reo_x}} \\ B_1 &\equiv \frac{A_1}{B_3} \\ B_2 &\equiv \frac{A_2}{B_3} \\ B_3 &\equiv A_1 + 2A_2 R_o \end{aligned} \tag{4.27}$$

$$\begin{aligned} \overline{Reo_{ej}} &\equiv \overline{Reo_x}\sqrt{B_{3j}} \\ \left(\frac{Reo_e{}'}{\overline{Reo_e}}\right)_j &\equiv B_{1j}\left(\frac{Reo_x{}'}{\overline{Reo_x}}\right) + B_{2j}\left(\frac{Reo_y{}'}{\overline{Reo_x}}\right) \end{aligned} \tag{4.28}$$

$R_o^2 \ll 1$ is assumed. J indexes as either the one or the two wire on the cross-wire probe. Solving this set of equations and decomposing into x and y components

$$\begin{aligned} \overline{Reo_x}^2 &= \frac{\overline{Reo_{e1}}^2/A_{21} - \overline{Reo_{e2}}^2/A_{22}}{A_{11}/A_{21} - A_{12}/A_{22}} \\ \overline{Reo_y} &= \frac{1}{2\overline{Reo_x}} \frac{\overline{Reo_{e1}}^2/A_{11} - \overline{Reo_{e2}}^2/A_{12}}{A_{21}/A_{11} - A_{22}/A_{12}} \end{aligned} \tag{4.29}$$

$$\overline{\left(\frac{Reo_x{}'}{\overline{Reo_x}}\right)^2} = \frac{1}{D_2{}^2}\left[\frac{1}{B_{21}{}^2}\overline{\left(\frac{Reo_e{}'}{\overline{Reo_e}}\right)^2_1} - \frac{2}{B_{21}B_{22}}\overline{\left(\frac{Reo_e{}'}{\overline{Reo_e}}\right)_1\left(\frac{Reo_e{}'}{\overline{Reo_e}}\right)_2} + \frac{1}{B_{22}{}^2}\overline{\left(\frac{Reo_e{}'}{\overline{Reo_e}}\right)^2_2}\right] \tag{4.30}$$

$$\overline{\left(\frac{Reo_y{}'}{\overline{Reo_x}}\right)^2} = \frac{1}{D_1{}^2}\left[\frac{1}{B_{11}{}^2}\overline{\left(\frac{Reo_e{}'}{\overline{Reo_e}}\right)^2_1} - \frac{2}{B_{11}B_{12}}\overline{\left(\frac{Reo_e{}'}{\overline{Reo_e}}\right)_1\left(\frac{Reo_e{}'}{\overline{Reo_e}}\right)_2} + \frac{1}{B_{12}{}^2}\overline{\left(\frac{Reo_e{}'}{\overline{Reo_e}}\right)^2_2}\right] \tag{4.31}$$

$$\overline{\left(\frac{Reo_x{}'}{\overline{Reo_x}}\frac{Reo_y{}'}{\overline{Reo_x}}\right)} = \frac{1}{2B_{11}B_{21}}\left[\overline{\left(\frac{Reo_e{}'}{\overline{Reo_e}}\right)^2_1} - B_{11}^2\overline{\left(\frac{Reo_x{}'}{\overline{Reo_x}}\right)^2} + B_{21}^2\overline{\left(\frac{Reo_y{}'}{\overline{Reo_x}}\right)^2}\right] \tag{4.32}$$

where $D_1 = (B_{21}/B_{11} - B_{22}/B_{12})$ and $D_2 = (B_{11}/B_{21} - B_{12}/B_{22})$. The covariance of the two wires can be expressed as

$$\overline{\left(\frac{v_w{}'}{\overline{V_w}}\right)_1\left(\frac{v_w{}'}{\overline{V_w}}\right)_2} = f_1 f_2\overline{\left(\frac{Reo_e{}'}{\overline{Reo_e}}\right)_1\left(\frac{Reo_e{}'}{\overline{Reo_e}}\right)_2} + g_1 g_2\overline{\left(\frac{T_t{}'}{\overline{T_t}}\right)} + f_1 g_2\overline{\left(\frac{Reo_e{}'}{\overline{Reo_e}}\frac{T_t{}'}{\overline{T_t}}\right)_1} + f_2 g_1\overline{\left(\frac{Reo_e{}'}{\overline{Reo_e}}\frac{T_t{}'}{\overline{T_t}}\right)_2} \tag{4.33}$$

The fluctuation of the Reynolds number can now be computed. The Reynolds number total temperature correlations result in

$$\overline{\frac{Reo_x{}'}{\overline{Reo_x}}\frac{T_t{}'}{\overline{T_t}}} = \frac{1}{D_2}\left[\frac{1}{B_{21}}\overline{\left(\frac{Reo_e{}'}{\overline{Reo_e}}\frac{T_t{}'}{\overline{T_t}}\right)_1} - \frac{1}{B_{22}}\overline{\left(\frac{Reo_e{}'}{\overline{Reo_e}}\frac{T_t{}'}{\overline{T_t}}\right)_2}\right] \tag{4.34}$$

$$\overline{\frac{Reo_y{}'}{\overline{Reo_x}}\frac{T_t{}'}{\overline{T_t}}} = \frac{1}{D_1}\left[\frac{1}{B_{11}}\overline{\left(\frac{Reo_e{}'}{\overline{Reo_e}}\frac{T_t{}'}{\overline{T_t}}\right)_1} - \frac{1}{B_{12}}\overline{\left(\frac{Reo_e{}'}{\overline{Reo_e}}\frac{T_t{}'}{\overline{T_t}}\right)_2}\right] \tag{4.35}$$

To obtain measurements in the x-z plane replace v by w and z replaces y. Also $\phi$ becomes $90 - \phi$ to remain consistent with a right hand coordinate system.

*4.3.1 Separation of Turbulence Variables.* The formulas used for the separation of turbulent quantities are

$$\begin{aligned} \frac{u'}{\overline{u}} &= \frac{(\rho u)'}{\overline{\rho u}} - \frac{\rho'}{\overline{\rho}} \\ \frac{v'}{\overline{u}} &= \frac{(\rho v)'}{\overline{\rho u}} - R_o \frac{\rho'}{\overline{\rho}} \\ \frac{\rho'}{\overline{\rho}} &= \frac{1}{\alpha+\beta}\left[\beta\left(\frac{(\rho u)'}{\overline{\rho u}} + R_o \frac{(\rho v)'}{\overline{\rho u}}\right) - \frac{T_t'}{\overline{T_t}} + \alpha \frac{p'}{\overline{p}}\right] \end{aligned} \tag{4.36}$$

where $\alpha \equiv [1 + 0.5(\gamma - 1)M^2]^{-1}$ and $\beta \equiv (\gamma - 1)\alpha M^2$. If $p'$ is assumed to be zero, which may be problematical, the cross-wire variable may be separated using equation 4.36. Note, Kistler (7) has suggested that $p'$ is proportional to $u'^2$; thus it is second order. In addition, Bowersox and Schetz (4) have experimentally verified the validity of this assumption for a Mach 4.0 free mixing layer. The six equations for the separated variables is given by:

$$\begin{bmatrix} 1 & 0 & 1 & 2 & 0 & 0 \\ 0 & 1 & R_o^2 & 0 & 2R_o & 0 \\ \beta^2 & \beta^2 R_o^2 & \alpha^2 & -2\alpha\beta & -2\alpha\beta R_o & 2\beta^2 R_o \\ 0 & 0 & R_o & R_o & 1 & 1 \\ \beta & 0 & -\alpha & \beta - \alpha & \beta R_o & \beta R_o \\ 0 & \beta R_o & -\alpha R_o & \beta R_o & \beta R_o^2 - \alpha & \beta \end{bmatrix} \begin{pmatrix} \overline{\left(\frac{u'}{\overline{u}}\right)^2} \\ \overline{\left(\frac{v'}{\overline{u}}\right)^2} \\ \overline{\left(\frac{\rho'}{\overline{\rho}}\right)^2} \\ \overline{\frac{\rho'}{\overline{\rho}}\frac{u'}{\overline{u}}} \\ \overline{\frac{\rho'}{\overline{\rho}}\frac{v'}{\overline{u}}} \\ \overline{\frac{u'}{\overline{u}}\frac{v'}{\overline{u}}} \end{pmatrix} = \begin{pmatrix} \overline{\left(\frac{(\rho u)'}{\overline{\rho u}}\right)^2} \\ \overline{\left(\frac{(\rho v)'}{\overline{\rho u}}\right)^2} \\ \overline{\left(\frac{T_t'}{\overline{T_t}}\right)^2} \\ \overline{\frac{(\rho u)'}{\overline{\rho u}}\frac{(\rho v)'}{\overline{\rho u}}} \\ \overline{\frac{(\rho u)'}{\overline{\rho u}}\frac{T_t'}{\overline{T_t}}} \\ \overline{\frac{(\rho v)'}{\overline{\rho u}}\frac{T_t'}{\overline{T_t}}} \end{pmatrix} \tag{4.37}$$

These transformations to Favré averaged N-S equations are given by (2)

$$\begin{aligned} \frac{\overline{u''}}{U} &= -\frac{\overline{\rho' u'}}{\overline{\rho u}} \\ \frac{\overline{v''}}{U} &= -\frac{\overline{\rho' v'}}{\overline{\rho u}} \qquad U \equiv \overline{\rho u}/\overline{\rho} \\ \overline{\rho u'' v''} &= \overline{\rho} \overline{u' v'} \end{aligned} \tag{4.38}$$

*4.3.2 Single Overheat.* If the hot-wire is operated at a higher overheat, then the sensitivity to the total temperature fluctuations is minimized. Thus if $T_t'$ is small, then the SOH technique can be used to obtain accurate mass flux results. The Strong Reynold's analogy was developed to correct for neglecting the total temperature sensitivity of the probe. If the total-temperature fluctuations are assumed negligible ($T_t' = 0$), then

according to reference (12)

$$\frac{T'}{\overline{T}} = -(\gamma - 1)M^2 \left( \frac{u'}{\overline{u}} + R_o \frac{v'}{\overline{u}} \right) \tag{4.39}$$

Bowersox (2) postulated that when $\mathrm{Pr} \neq 1$ and $T_t' \neq 0$ the temperature fluctuations can be represented by

$$\frac{T'}{\overline{T}} = -\kappa(\gamma - 1)M^2 \left( \frac{u'}{\overline{u}} + R_o \frac{v'}{\overline{u}} \right) \tag{4.40}$$

where $\kappa$ is determined empirically as ranging from 0.0 to 1.0. Defining $\theta = -\kappa(\gamma - 1)M^2$, and assuming $R_o^2\theta \ll 1$ and $R_o^2\theta^2 \ll 1 - \theta$ then

$$\frac{u'}{\overline{u}} = \frac{1}{1-\theta} \left[ \frac{(\rho u)'}{\overline{\rho u}} + R_o \theta \frac{(\rho v)'}{\overline{\rho u}} \right] \tag{4.41}$$

$$\frac{v'}{\overline{u}} = \frac{R_o \theta}{1-\theta} \frac{(\rho u)'}{\overline{\rho u}} + \frac{(\rho v)'}{\overline{\rho u}} \tag{4.42}$$

$$\frac{T_t'}{\overline{T}_t} = \frac{\beta + \alpha\theta}{1-\theta} \left[ \frac{(\rho u)'}{\overline{\rho u}} + R_o \theta \frac{(\rho v)'}{\overline{\rho u}} \right] \tag{4.43}$$

with this, the cross-wire equations can be reduced to

$$[S_{ij}] \begin{pmatrix} \overline{\left(\frac{Reo_x'}{Reo_x}\right)^2} \\ \overline{\frac{Reo_x'}{Reo_x}\frac{Reo_y'}{Reo_x}} \\ \overline{\left(\frac{Reo_y'}{Reo_x}\right)^2} \end{pmatrix} = \begin{pmatrix} \overline{\left(\frac{v_w'}{V_w}\right)_1^2} \\ \overline{\left(\frac{v_w'}{V_w}\right)_2^2} \\ \overline{\left(\frac{v_w'}{V_w}\right)_1 \left(\frac{v_w'}{V_w}\right)_2} \end{pmatrix} \tag{4.44}$$

where

$$
\begin{aligned}
S_{11} &= f_1^2 B_{11}^2 + 2 f_1 g_1 R_{mT} R_{uT} B_{11} + g_1^2 R_{mT}^2 \\
S_{12} &= 2[f_1^2 B_{11} B_{21} + f_1 g_1 R_{mT} (R_{uT} R_o B_{11} + \\
&\qquad R_{vT} B_{21}) + g_1^2 R_{mT}^2 R_o] \\
S_{13} &= f_1^2 B_{21}^2 + 2 f_1 g_1 R_{mT} R_{vT} R_o B_{21} \\
S_{21} &= f_2^2 B_{12}^2 + 2 f_2 g_2 R_{mT} R_{uT} B_{12} + g_2^2 R_{mT}^2 \\
S_{22} &= 2[f_2^2 B_{12} B_{22} + f_2 g_2 R_{mT} (R_{uT} R_o B_{12} + \\
&\qquad R_{vT} B_{22}) + g_2^2 R_{mT}^2 R_o] \\
S_{23} &= f_2^2 B_{22}^2 + 2 f_2 g_2 R_{mT} R_{vT} R_o B_{22} \\
S_{31} &= f_1 f_2 B_{11} B_{12} + f_1 g_2 R_{mT} R_{uT} B_{11} + \\
&\qquad f_2 g_1 R_{mT} R_{uT} B_{12} + g_1 g_2 R_{mT}^2 \\
S_{32} &= f_1 f_2 (B_{11} B_{22} + B_{12} B_{21}) + f_1 g_2 R_{mT} (R_{uT} R_o B_{11} + R_{vT} B_{21}) \\
&\qquad + f_2 g_1 R_{mT} (R_{uT} R_o B_{12} + R_{vT} B_{22}) + 2 g_1 g_2 R_{mT}^2 R_o \\
S_{33} &= f_1 f_2 B_{21} B_{22} + f_1 g_2 R_{mT} R_{vT} R_o B_{21} + f_2 g_1 R_{mT} R_{vT} R_o B_{22}
\end{aligned}
\tag{4.45}
$$

The correlations above are given by:

$$
\begin{aligned}
R_{mT} &= \frac{\beta + \alpha\theta}{1-\theta} \\
R_{uT} &= \frac{\overline{(\rho u)' T_t'}}{\sqrt{\overline{(\rho u)'^2}} \sqrt{\overline{T_t'^2}}} \\
R_{vT} &= \frac{\overline{(\rho v)' T_t'}}{\sqrt{\overline{(\rho v)'^2}} \sqrt{\overline{T_t'^2}}}
\end{aligned}
\tag{4.46}
$$

### *4.4 Turbulence Transformation*

Bowersox and Schetz (4) have shown that the Reynolds shear stress can be expressed in terms of the conservative cross-wire variables as

$$
\tau_{ij}^T = -\frac{\overline{(\rho u_i)'(\rho u_j)'}}{\overline{\rho}} + \overline{\rho u_i u_j} \left(\frac{\overline{\rho'}}{\overline{\rho}}\right)^2 \tag{4.47}
$$

where the second term on the right hand side has been shown to be much less than the first term for thin layer type flows. If the effects of the pressure fluctuations on the cross-wire response are assumed small, then the cross-wire results can be decomposed into "nonconservative" variables (Bowersox (3)), i.e,

$$\overline{(\rho')^2}, \qquad \overline{(u_i')^2}, \quad \overline{u_i' u_j'}, \qquad \overline{\rho' u_j'}$$

Hot wire anemometry was used in the mode of constant temperature. Constant temperature (resistance) was chosen because with constant current anemometers wires can self destruct in flows which have sharp decreases in velocity (16). The AFIT wind tunnel has strong un-starting shock waves which could possibly burn the probes out under these conditions. In this study a constant temperature anemometer with fixed resistance was connected to a 1:1 bridge. The current resistance level was set to 10.4 ohms. The signal of the hot wire probes were broken down into three components, the mean value, the cross-correlation, and the root mean square of the deviation.

Mean:

$$\overline{V_i} = \frac{1}{N} \sum V_i \tag{4.48}$$

$$V_i' = (V_i - \overline{V_i})/[\overline{V_i}'(N-1)] \tag{4.49}$$

$$\overline{V_1' V_2'} = (V_1' * V_2')/[(N-1) * \overline{V_1} * \overline{V_2}] \tag{4.50}$$

Where N is the number of sampled points, and i is the wire number.

## *V. Results and Discussion*

A characterization of the boundary layer and its turbulent structure was obtained using the Pitot probe, cone static probe, and the cross wires at a location 44 cm from the nozzle throat to document the flow before the expansion region. In this way, when taken in concert with the same measurements (Pitot, cone static, and cross wires) made in the favorable pressure gradient region (71.5 cm downstream from the nozzle throat), the effects of the changes in the pressure on the turbulent flow structure can be ascertained.

### *5.1 Shadowgraph and Schlieren Photography*

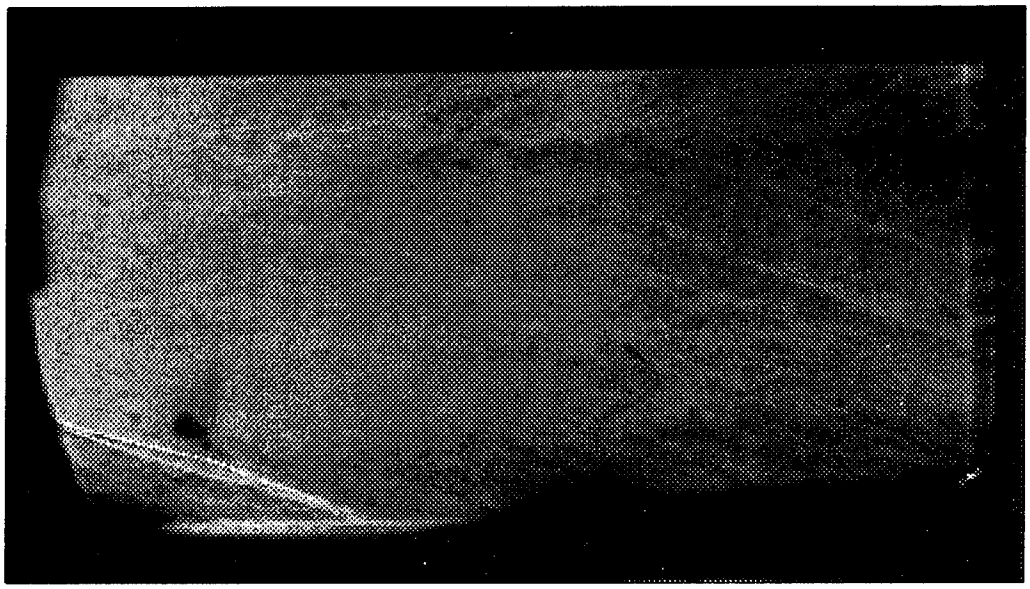

Figure 5.1 Test Section Shlieren Image

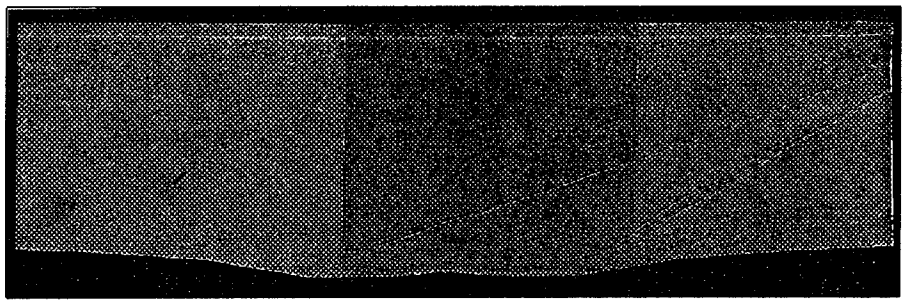

Figure 5.2 Test Section Shadowgraph Image

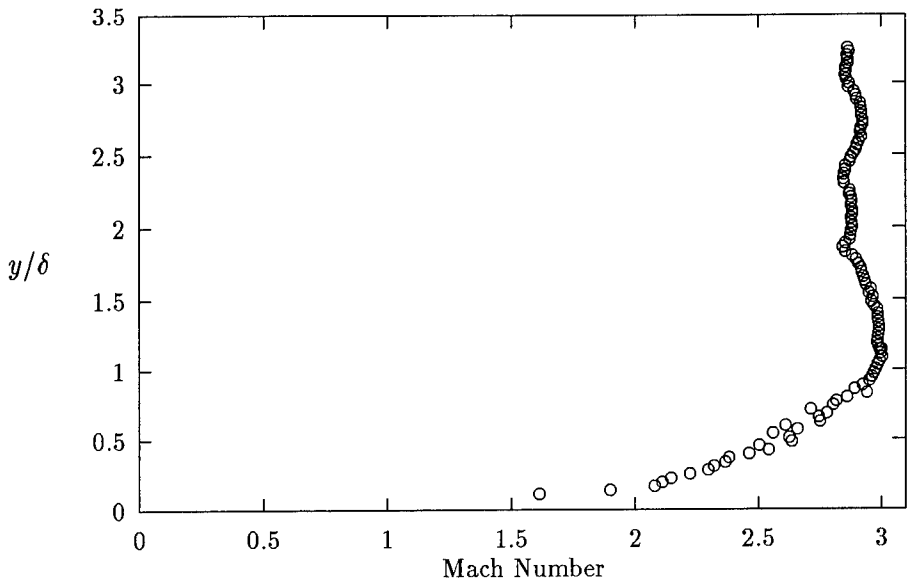


Figure 5.3 Test Section Mach Profile x = 71.5 cm

In Figure 5.1 is presented a schlieren image in the vicinity of the expansion fan. Note that the boundary layer has not separated, the thickness of the boundary layer is increasing in the streamwise direction, and the presence of turbulent eddies. The shadowgraph image in Figure 5.2 is presented, but is of little value in an expansion region since the mean density gradients are rather small. In Figure 5.3 is presented the profile of the Mach number across the wind tunnel as determined using Pitot and cone-static probes. Figure 5.4 is a plot of the $P_{t2}/P_{t\infty}$ profile at x = 71.5 cm. The jumps in pressure are located in the vicinity of the expansion fans.

### *5.2 Conventional Data*

Detailed Pitot and cone-static measurements are obtained along the tunnel centerline at x = 44 cm and 71.5 cm, Figure 5.5 shows a rough outline of the measurement locations, where 1 is the x = 44 cm location and 2 is the x = 71.5 cm location. The latter station is located in the vicinity of the expansion. Variation of the mean-flow profiles in the streamwise direction highlights the effect of the pressure gradient; the mean flow accelerates under the influence of a favorable pressure gradient (Figure 5.3). The boundary layer edge, at the 44 cm location, is defined as the point at which the mean velocity reached 99% of

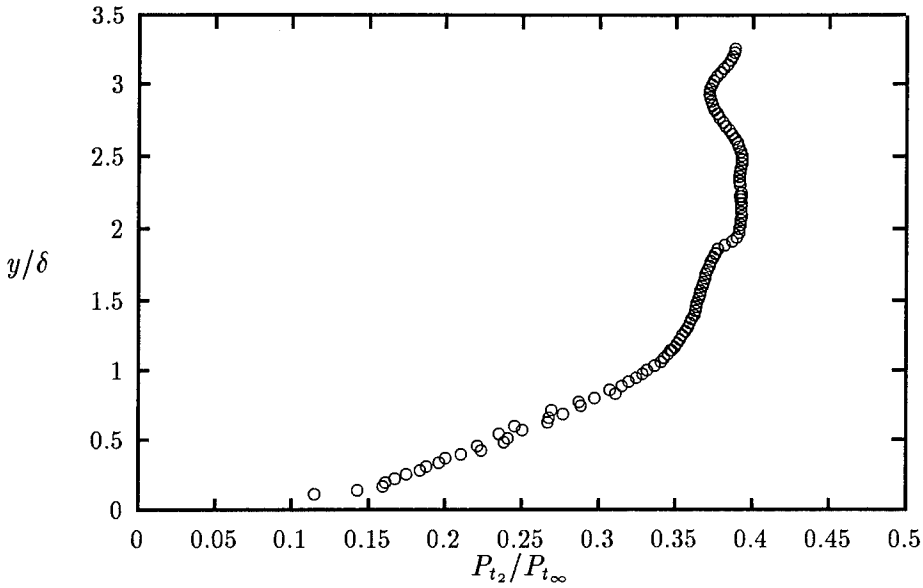


Figure 5.4 Test Section Pressure Profile $P_{t2}/P_{t\infty}$ x = 71.5 cm

the mean value at the tunnel centerline. Because the flow in the expansion section is not fully developed, the 99% criteria is based on the highest Mach number peak near the wall. This peak Mach number is 3.0. The boundary layer thickness at x = 44 cm is estimated at 0.83 cm and 1.17 cm downstream (x = 71.5 cm). The freestream Mach number is 2.9 upstream. Measurements acquired as part of the current study extend to within $y/\delta \approx 0.06$ of the wall upstream and $y/\delta \approx 0.09$ downstream.

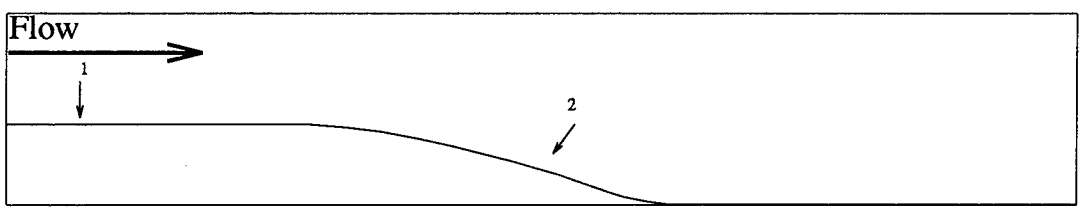


Figure 5.5 Test Section

### *5.3 Repeatability of Data*

One difficulty with experimental work is that the data must be measured in a stable environment where the variable of the conditions do not change. The precautions mentioned earlier in Chapter III highlight some of the steps taken to insure the equipment is stable. As a means of investigating the repeatability of the data, several duplicate runs

were conducted. In particular, the profiles of the flow in Figure 5.6 were taken on two different days with the same hot-wire probe. The profiles of the flow in Figure 5.7 are from the second channel of the UW x-wire probe. Through comparison of flow profiles obtained using alternative means (i.e. conventional and hot wire methods) a comparison was made of Mach profile shape and voltage cross-correlation from the cross-wires. Figure 5.8 shows the Mach profile through the boundary layer and Figure 5.9 shows the downstream shear profile from the SOH data. Again, the close correlation of the profile shapes demonstrates the repeatability of the data. To confirm the consistency of the hot wire data, the mean

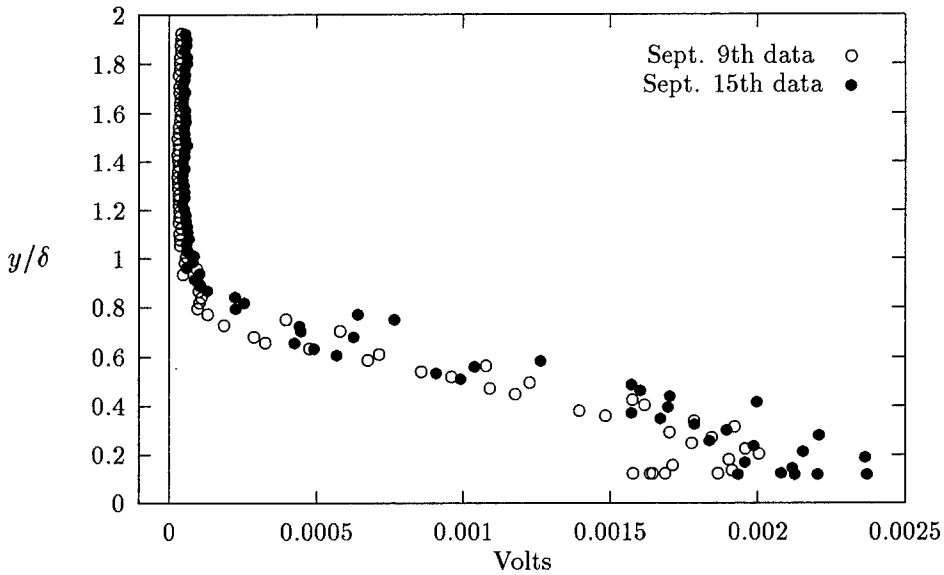


Figure 5.6 UW RMS Voltage Wire 1(x = 44 cm)

flow data profile shapes are compared. The mean flow voltages are plotted in Figure 5.10. The close agreement in shape of the five plots confirms the repeatability of the runs.

### *5.4 Hot Wire Constants*

The constants in the equations for reduction of the SOH data are derived from the MOH data. The terms $R_{uT}$, $R_{vT}$ and $R_{wT}$ were determined by averaging the values calculated from different MOH runs. They were determined to be 0.6, -0.5, and 0.15. The variable $\kappa$ was determined by matching the SOH and MOH data by adjusting $\kappa$ until the data aligned. This value was highly dependent on the SOH ratio and can be shown that

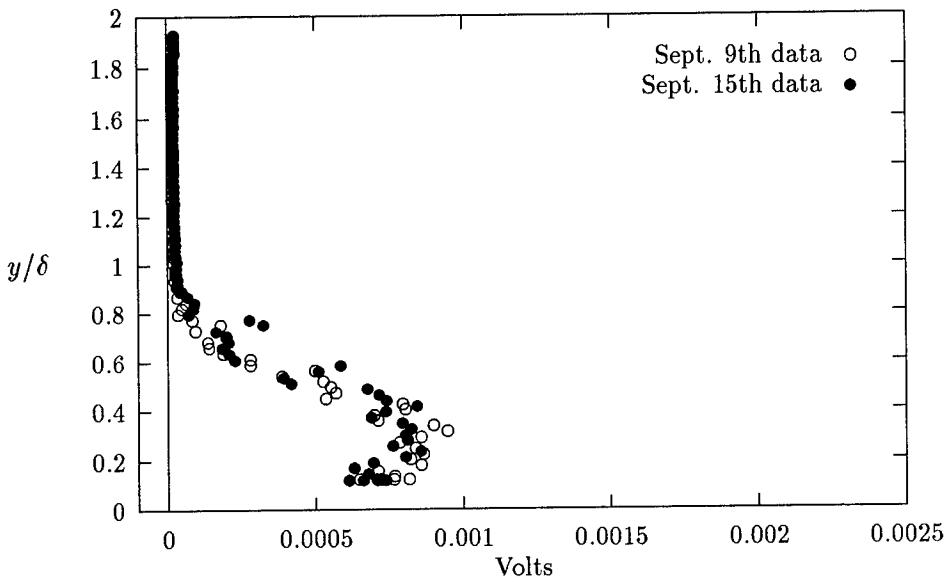


Figure 5.7 UW RMS Voltage Wire 2(x = 44 cm)

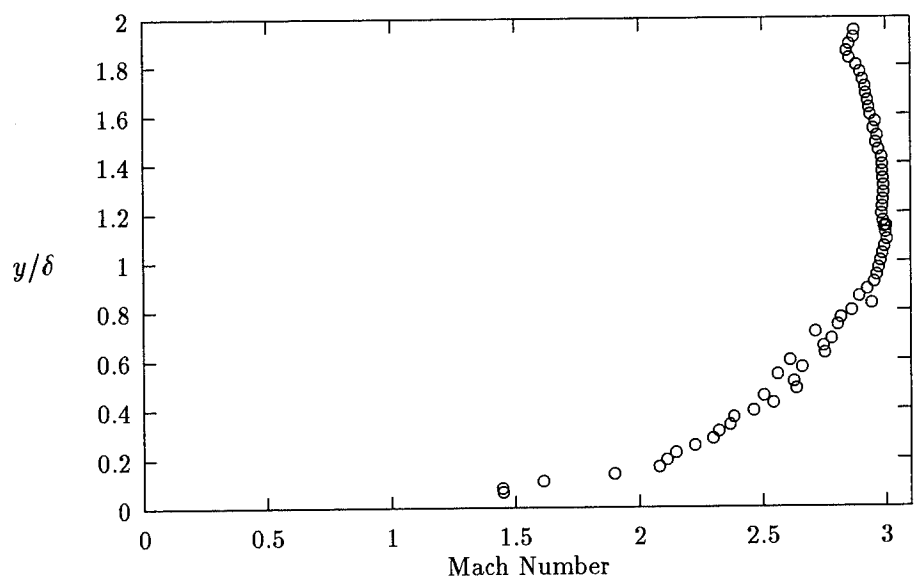


Figure 5.8 Mach Profile (x = 44 cm)

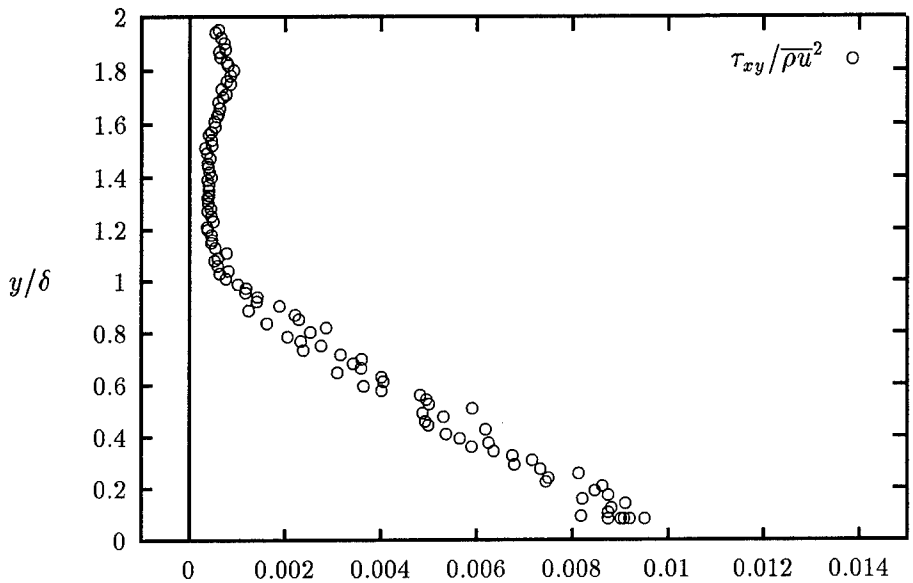


Figure 5.9 Shear Stress (x = 44 cm)

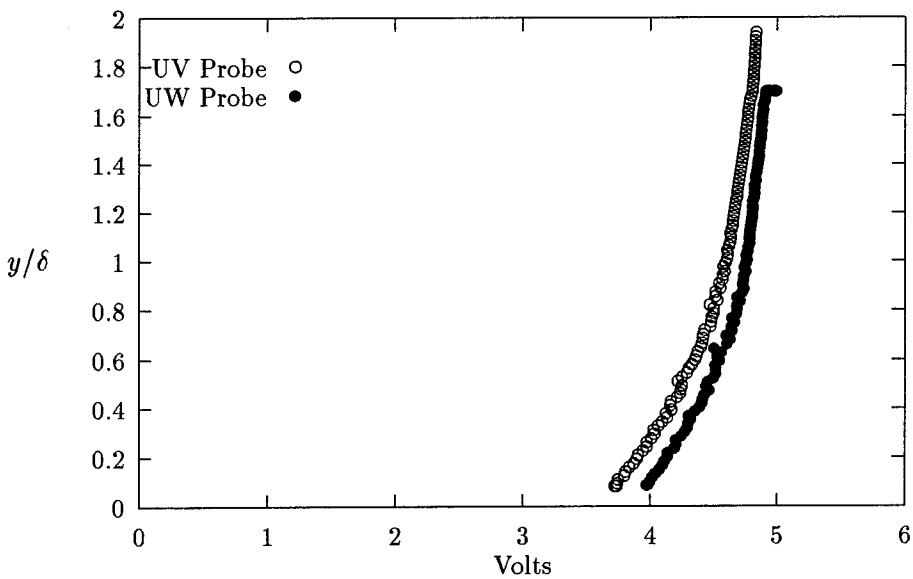


Figure 5.10 Hot Wire Mean Voltage(x = 44 cm)

$\kappa = f(OHR)$. The overheat ratios (OHR) force a sensitivity to flow properties that respond to factors in the Strong Reynolds analogy equation. The Strong Reynolds analogy assumes $\kappa \approx 1(11)$. This applies to flows where the sensitivities, f and g, are not coincidental and are widely separated, i.e., overheat levels below approximately 1.8. The sensitivities are mentioned in Chapter 4 and are related to the system fluctuations by

$$\frac{V'}{V} = f\frac{(\rho u)'}{\overline{\rho u}} + g\frac{T_t'}{\overline{T_t}} \tag{5.1}$$

An approximate graph of the behavior of f and g looks like Figure 5.11 and $\frac{T_t'}{\overline{T_t}}$ is usually

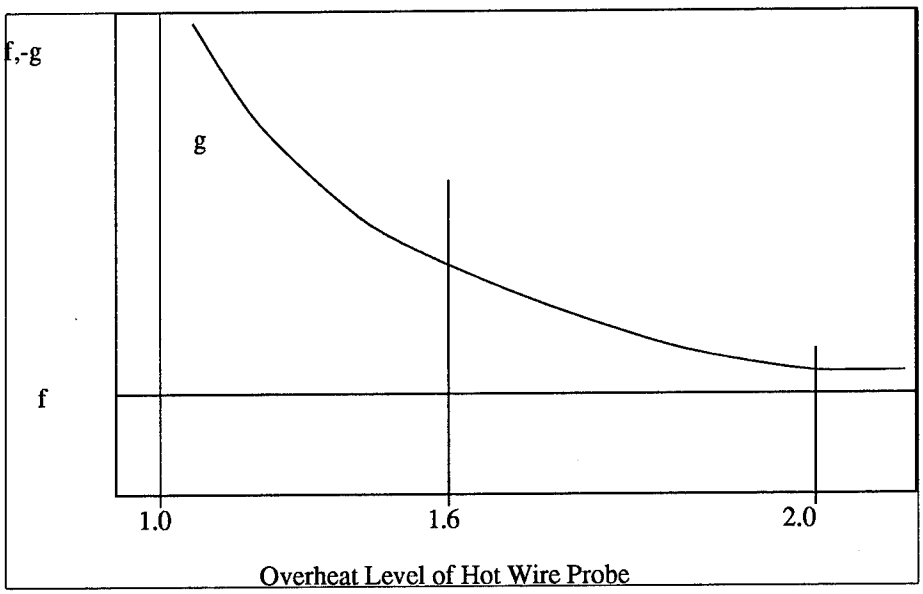


Figure 5.11 Hot Wire Probe Sensitivities

assumed small. To solve for $\kappa$ experimentally multiple overheat values are used and flow properties are derived as in chapter 4. In this way the data is made independent of overheat level. For overheat values larger than 1.9, $\kappa$ has a more gradual influence.

For the SOH UV data the overheat level was approximately 1.6, and a value of $\kappa \approx 1.0$ is appropriate, as postulated in Morkovin's work. This aligned the UV data with the MOH data. Figure 5.12 represents $\kappa = 0$, Figure 5.13 represents $\kappa = 0.4$, and Figure 5.14 represents $\kappa = 1.0$.

The UW SOH data on the other hand was found to align best at $\kappa = 0$. The UW data overheat ratio was approximately 2.2, causing the data to be less sensitive to $\kappa$ changes.

Figure 5.15 shows UW data with $\kappa = 1.0$ and Figure 5.16 shows when $\kappa = 0.0$. The $\kappa = 0.0$ data aligns best with the multiple overheat data and removes the disparity from the U component in the UV and UW data. When $\kappa$ was set to either 1.0 or 0.4 for

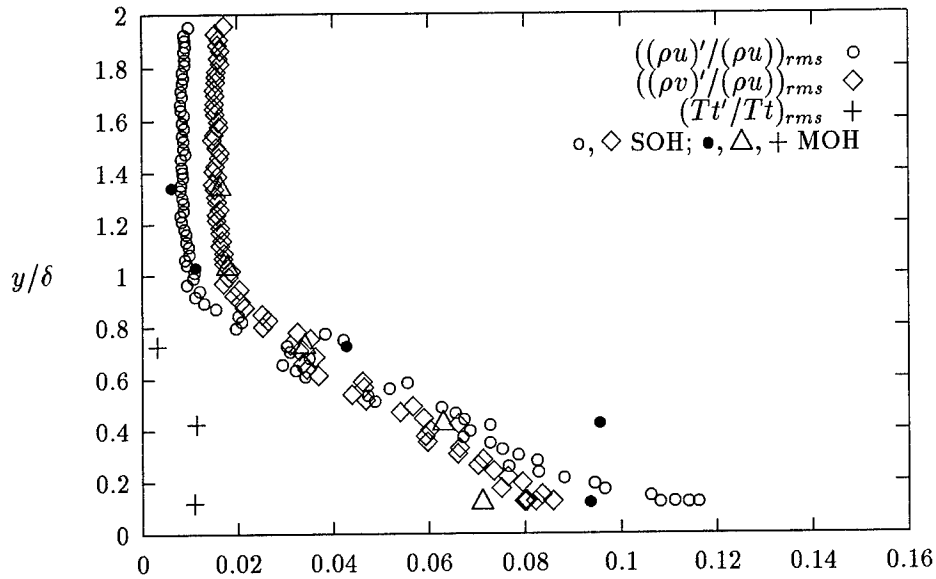


Figure 5.12 UV Probe Turbulence Intensities ($\kappa = 0$ x = 44 cm)

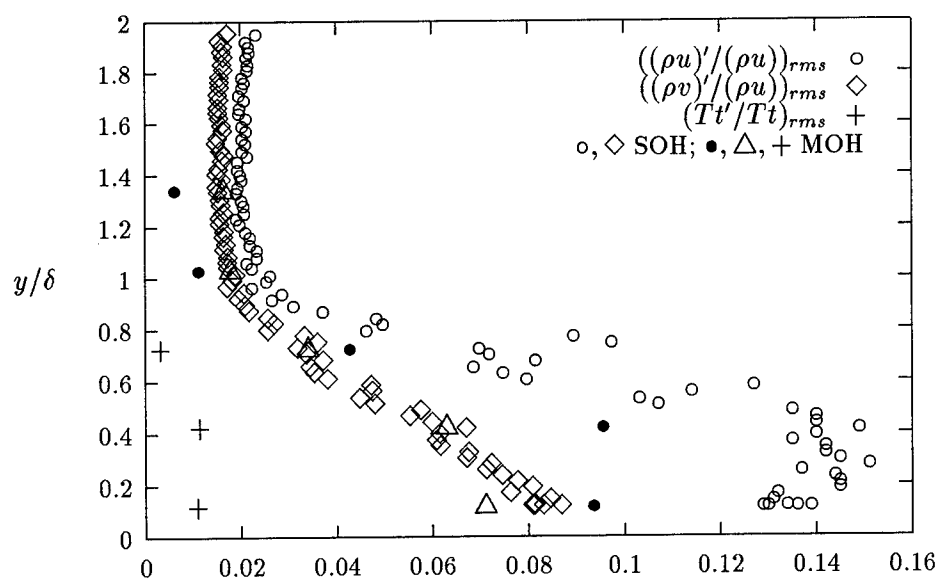


Figure 5.13 UV Probe Turbulence Intensities ($\kappa = .4$ x = 44 cm)

both channels the U-component differed by 0.02. The sensitivity disparity between f and g are accounted for by $\kappa = 1$. By increasing the overheat ratios to be near 2.0 the disparity

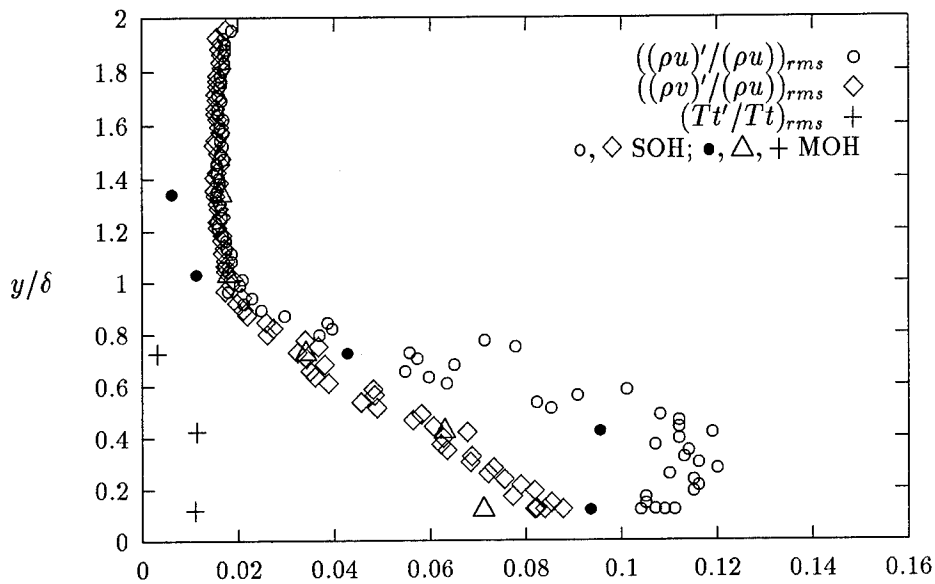


Figure 5.14 UV Probe Turbulence Intensities ($\kappa = 1$ x = 44 cm)

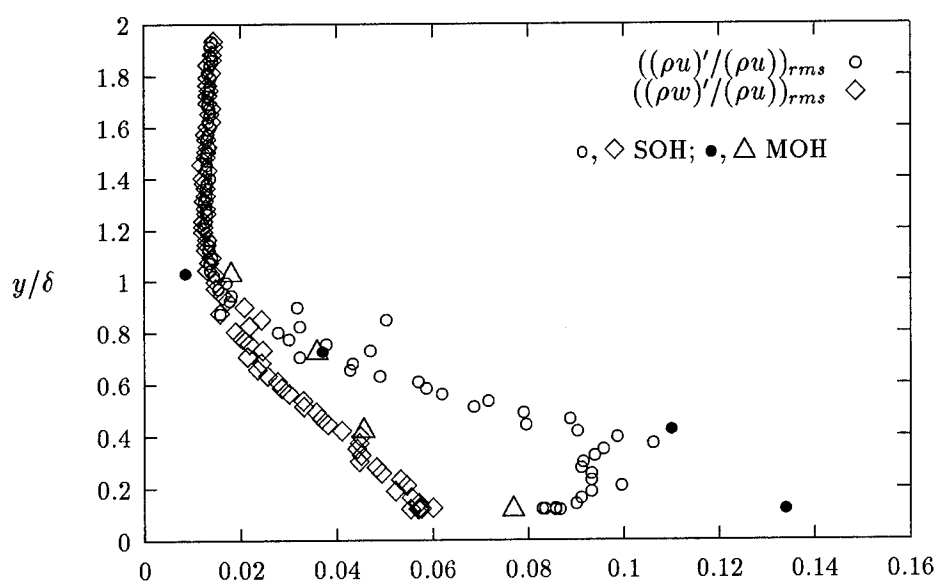


Figure 5.15 UW Probe Turbulence Intensities ($\kappa = 1$ x = 44 cm)

between f and g sensitivities can be removed when $\kappa$ is set to zero, i.e. less temperature sensitivity in equation 4.40 ($T'/\overline{T_t} = 0$).

### *5.5 Zero Pressure Gradient Region*

The turbulence intensities represented in Figure 5.14 and Figure 5.16 of the UV and UW wires, respectively are the quantities measured directly by the hot-wires. The relative magnitude of this term is the largest of the intensity terms in the boundary layer. This term also appears to be asymptotically approaching a much lower value as it nears the wall. The terms $((\rho v)'/(\rho u))_{rms}$ and $((\rho w)'/(\rho u))_{rms}$ both appear to be approaching the wall at a linear rate. The multiple overheat data shows good agreement with the single overheat data.

The separated turbulence intensities follow a similar pattern. The Figures 5.17 and 5.18 illustrate the separated turbulence intensities. The components of $u'$, $v'$, $w'$ all follow a nearly linear slope through the boundary layer. Near the wall all three terms collapse within the same region of both graphs. Additionally, when the terms reach the edge of the boundary layer $(v'/u)_{rms}$, $(w'/u)_{rms}$ and $(\rho'/\rho)_{rms}$ collapse into the same region, whereas the term $(u'/u)_{rms}$ is near zero in the freestream. The fluctuating term $(\rho'/\rho)_{rms}$ is the largest fluctuating component through most of the boundary layer.

The component of shear in the x-y plane is predominantly composed of the $\overline{u\rho' v'}/\overline{\rho u}^2$ term, Figure 5.19. Within the majority of the boundary layer, neglecting the boundary layer region below $y/\delta \approx 0.2$ and the top 10% of the boundary layer edge, $\overline{u\rho' v'}/\overline{\rho u}^2$ is approximately 67% of the total shear. Neglecting this term would be neglecting the majority of the shear. The terms $v'$ and $\rho'$ are the larger fluctuating components in the boundary layer and contribute to create the larger term $\overline{u\rho' v'}/\overline{\rho u}^2$. Similarly, the terms $w'$ and $\rho'$ contribute to the $\overline{u\rho' w'}/\overline{\rho u}^2$ term being the largest contribution to the $\tau_{xz}$ term, Figure 5.20. Note that the maximum value of $\tau_{xy}$ is twice as large the maximum of $\tau_{xz}$. Furthermore, the term $\tau_{xz}$ is only significant in the lower half of the boundary layer.

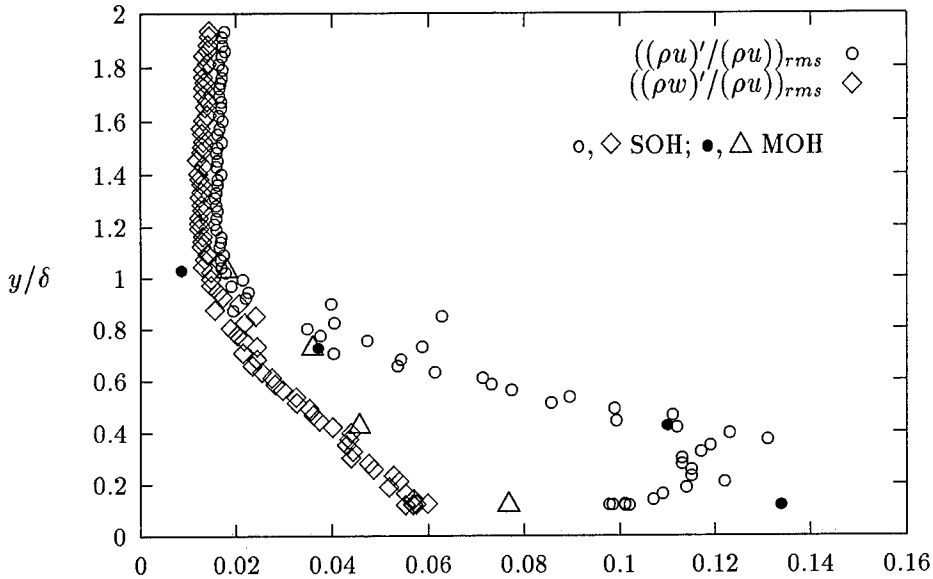


Figure 5.16 UW Probe Turbulence Intensities ($\kappa = 0$ x = 44 cm)

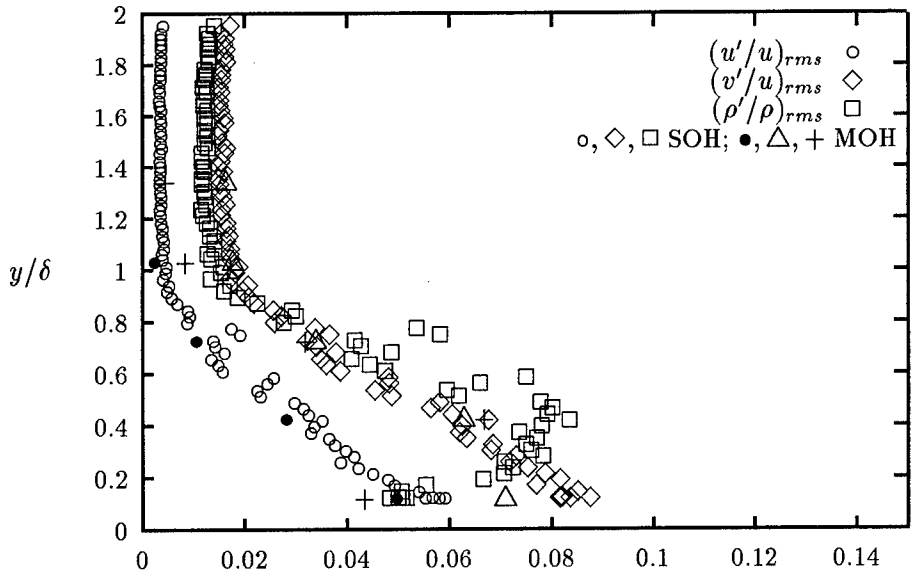


Figure 5.17 UV Probe Separated Turbulence Intensities (x = 44 cm)

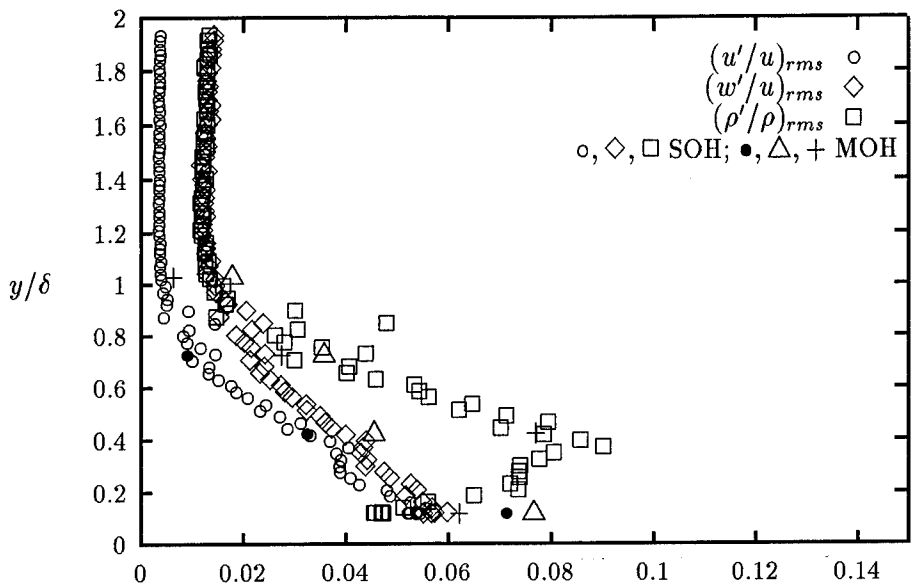


Figure 5.18 UW Probe Separated Turbulence Intensities (x = 44 cm)

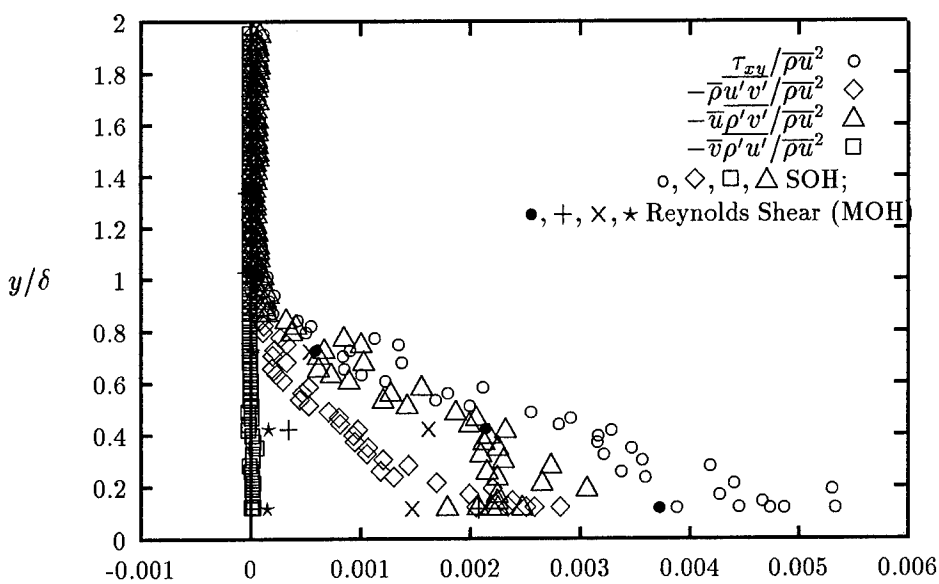


Figure 5.19 UV Probe Shear (x = 44 cm)

The UV Reynolds shear derived from the MOH data is in close agreement with the measured shear stress. The MOH derived values of the Favré shear

$$\tau_{xy}^{T} \mid_{Favré} = \bar{\rho}\overline{u''v''} \approx \rho\overline{u'v'} \tag{5.2}$$

estimates the first term of the Reynolds shear well also showing the close agreement between the SOH and MOH data. Morkovin postulated that the velocity density correlation,

$$\frac{\overline{u}\overline{\rho'v'}}{\bar{\rho}\overline{u'v'}} \approx 1$$

where we have found this quantity to be approximately 2 though 60 to 70% of the boundary layer.

### *5.6 Favorable Pressure Gradient Region*

The raw turbulence intensities $((\rho u)'/(\rho u))_{rms}$, etc. in the expansion region are still dominated by the term $((\rho u)'/(\rho u))_{rms}$, Figure 5.21 and Figure 5.22. The freestream value of the UW probe is 0.02 whereas the UV probe has a value of approximately 0.03 in the freestream. The components $((\rho w)'/(\rho u))_{rms}$ and $((\rho v)'/(\rho u))_{rms}$ both follow a nearly linear progression from the freestream value down to maximum values of 0.06 and 0.1 respectively. The component $((\rho u)'/(\rho u))_{rms}$ follows a "fuller" curved path which curves back towards the value of the other two terms as it approaches the lowest measured station.

The separated turbulence intensities provide an insight as to which terms are causing this characteristic, Figure 5.23 and Figure 5.24. Again the predominant fluctuation quantity is the density, $(\rho'/\rho)_{rms}$. As the flow approaches the wall, below $y/\delta \approx 0.2$, the components of $u'$ and $w'$ become the predominant terms. $u'$, $v'$, and $w'$ vary linearly across the boundary layer, while the term $(\rho'/\rho)_{rms}$ has the characteristic shape of the turbulence intensity term $((\rho u)'/(\rho u))_{rms}$.

From these observations and experience with the upstream (44 cm) data one could conclude that the shear stress would predominantly be driven by the density fluctuation component. The component of the shear, Figure 5.25 and Figure 5.26, $\overline{u}\overline{\rho'v'}/\overline{\rho u}^2$ is

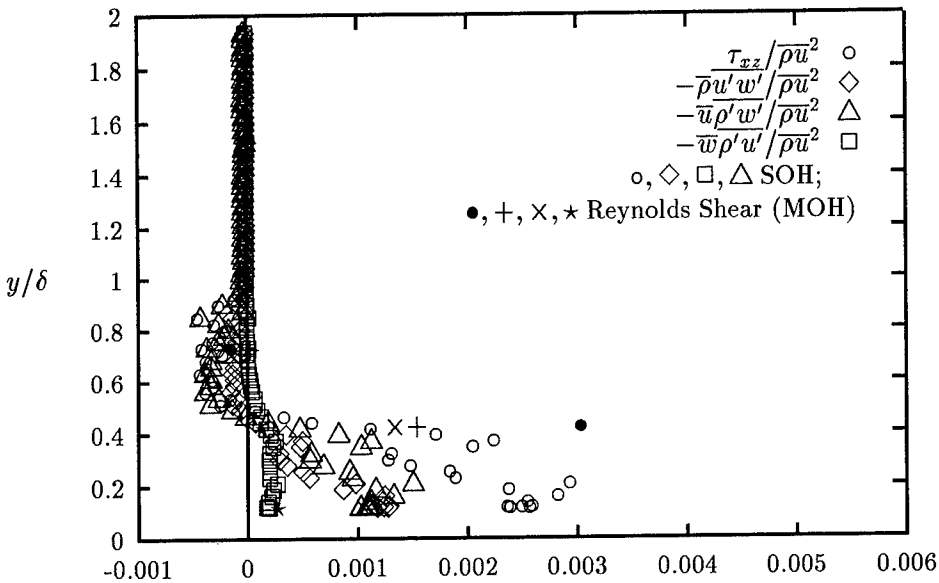


Figure 5.20 UW Probe Shear (x = 44 cm)

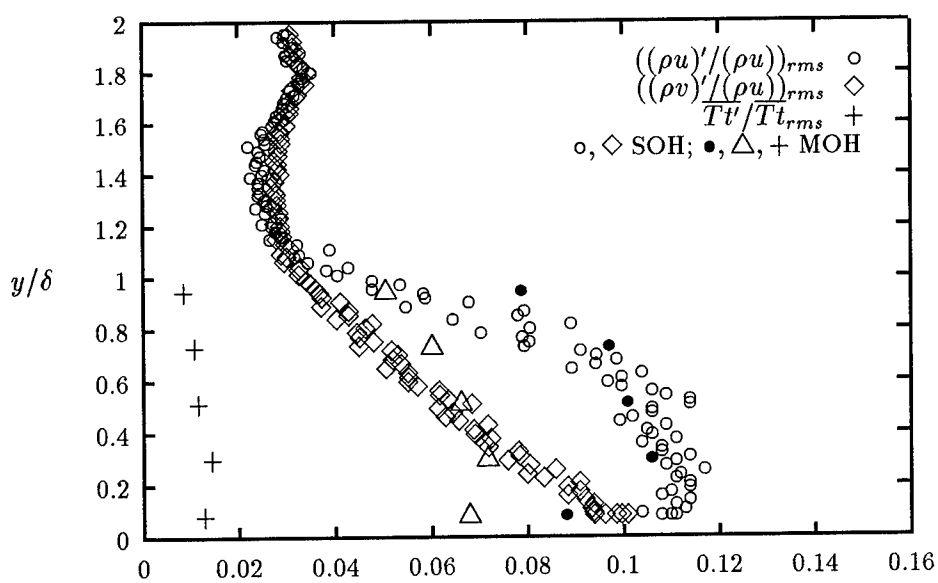


Figure 5.21 UV Probe Turbulence Intensities (x = 71.5 cm)

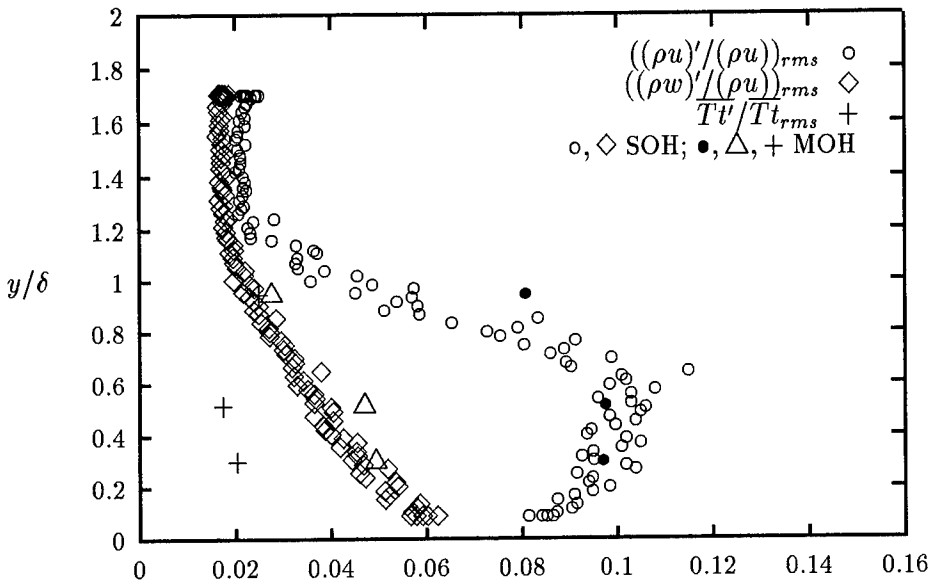


Figure 5.22 UW Probe Turbulence Intensities (x = 71.5 cm)

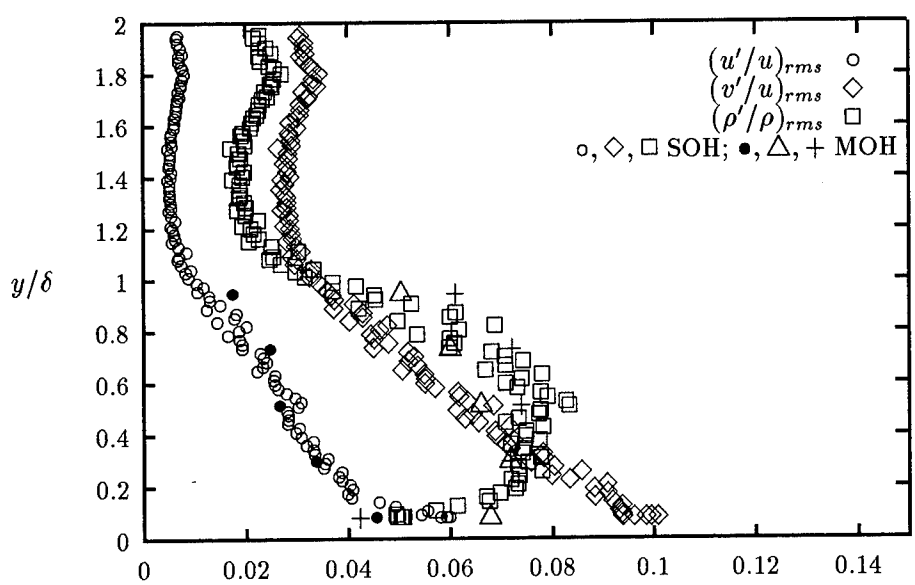


Figure 5.23 UV Probe Separated Turbulence Intensities (x = 71.5 cm)

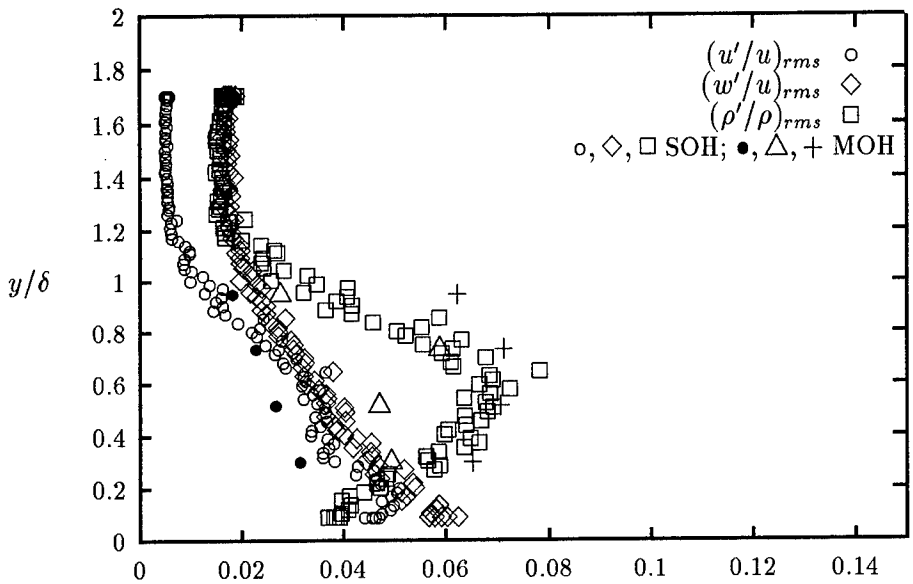


Figure 5.24 UW Probe Separated Turbulence Intensities (x = 71.5 cm)

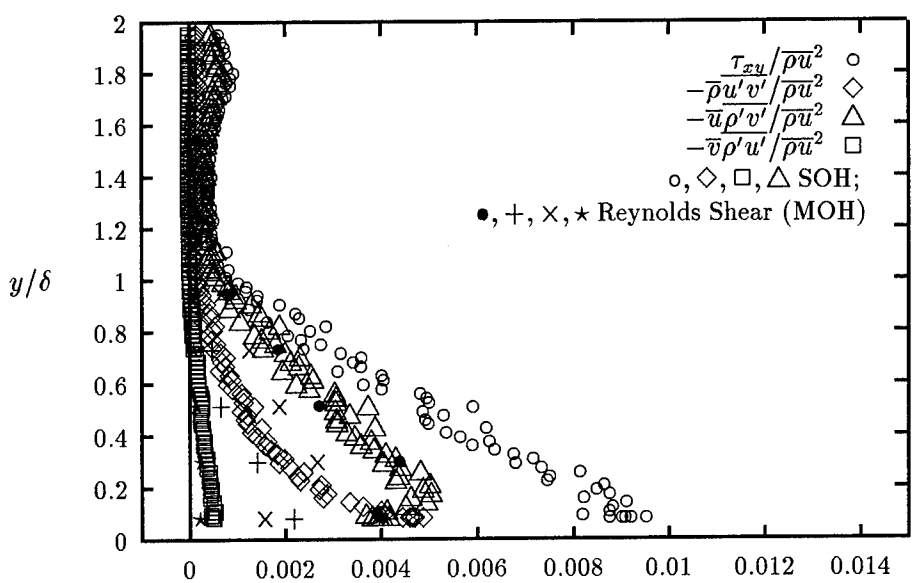


Figure 5.25 UV Probe Shear (x = 71.5 cm)

the dominant term, exhibiting the same behavior, with 67% of the shear residing in this term throughout most of the boundary layer. The shear $\tau_{xz}$ is less pronounced, but the density term $\overline{u}\overline{\rho' w'}/\overline{\rho u}^2$ accounts for at least 50% of the shear in this plane. The MOH Reynolds shear estimation for the x-y plane tracked the SOH term $\overline{u}\overline{\rho' v'}/\overline{\rho u}^2$ throughout the boundary layer. This term accounts for 67% of the total shear. The Favré on the other hand continued to track the $\overline{\rho}\overline{u'' v''}/\bar{\rho}\bar{u}^2$ term. Given the predominance of the mean flow in the streamwise direction, shear stress terms such as $-\overline{v}\overline{\rho' u'}/\overline{\rho u}^2$ and $-\overline{w}\overline{\rho' u'}/\overline{\rho u}^2$, are insignificant. Similar to the upstream flow the velocity-density correlation relation of Morkovin is also found to be $\approx 2.0$.

Comparison of the turbulence intensities from the 44 cm upstream test station to the 71.5 cm test station shows subtle changes in the character of the flow ( Figures 5.14, 5.21, 5.16 and 5.22). The component $((\rho v)'/(\rho u))_{rms}$ increased slightly in the downstream location. The freestream value of both of the u and v components increased from approximately 0.02 upstream to 0.03 downstream. This change accounts for the increase of the $((\rho v)'/(\rho u))_{rms}$ data. The UW wire shows a similar trend. A slight increase in the $((\rho w)'/(\rho u))_{rms}$ component can be seen in the freestream. Additionally, the peak value of $((\rho u)'/(\rho u))_{rms}$ has decreased downstream, but it also has a "fuller" profile. The separated turbulent intensities show similar characteristics. The maximum value of $v'$ increases from a peak value upstream of $\approx 0.085$ to $\approx 0.1$ downstream. The components of turbulence for $u'$ remains relatively constant, with a very slight decrease in the peak value downstream. The slope of the $u'$ and $v'$ component through the boundary layer does not change. The peak of the density fluctuation decreases.

At the top and bottom 10% of the boundary layer (Figures 5.19, 5.25, 5.20 and 5.26), the proportionality of the shear components is approximately 50/50. Throughout the remainder of the boundary layer the proportionality is split with 33% in the first term and 67% in the second term. It is curious to see that the first contribution to the Reynolds stress appears to be increasing asymptotically as it approaches the lowest measured station. The second term seems to die off rapidly after passing the point of $y/\delta \approx 0.2$. This last observation is not as apparent in the upstream graph.

The reduction of the shear into the separate Reynolds stress components assumes that the second term in the conservative cross-wire shear equation is small.

$$\tau_{ij}^{T} = -\frac{\overline{(\rho u_i)'(\rho u_j)'}}{\overline{\rho}} + \overline{\rho u_i u_j}(\frac{\overline{\rho'}}{\overline{\rho}})^2 \tag{5.3}$$

This can be verified by looking at the graph of the shear contributions, Figure 5.27 and Figure 5.28. The second term is essentially a third order term because $\overline{v}$ is on the order of $v'$, causing this term to be small. So although the pressure fluctuations must be assumed small to separate out the terms in the Reynolds stresses equation, i.e.

$$\tau_{ij}^{T} = -\overline{\rho}\overline{u_i' u_j'} - \overline{u_i}\overline{\rho' u_j'} - \overline{u_j}\overline{\rho' u_i'} - \overline{\rho' u_i' u_j'} \tag{5.4}$$

the value of the Reynolds stress can be assumed to be accurate regardless of the pressure fluctuation assumption.

### *5.7 Heat Flux*

Few studies have documented the turbulent heat flux behavior. The use of MOH allows the separation of the heat flux terms necessary for solution of the energy equation. Figure 5.29 shows the heat flux terms from the UV cross wire and Figure 5.30 shows the values obtained from the UW cross wire.

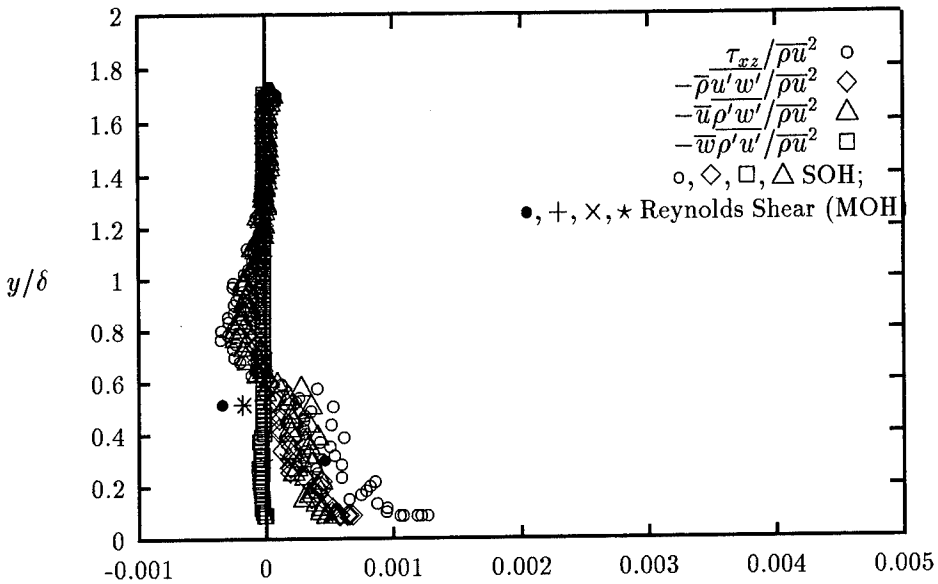


Figure 5.26 UW Probe Shear (x = 71.5 cm)

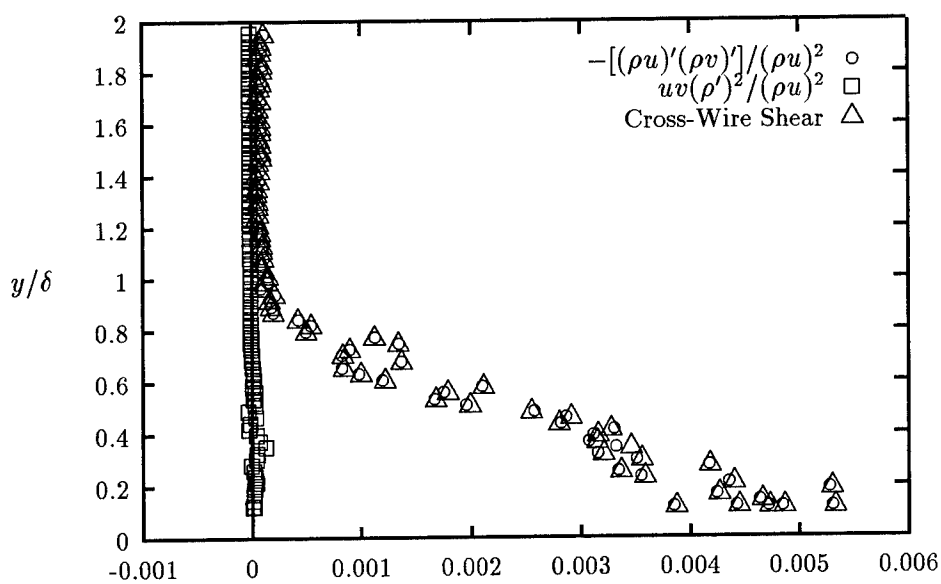


Figure 5.27 UV Probe Shear (x = 44 cm)

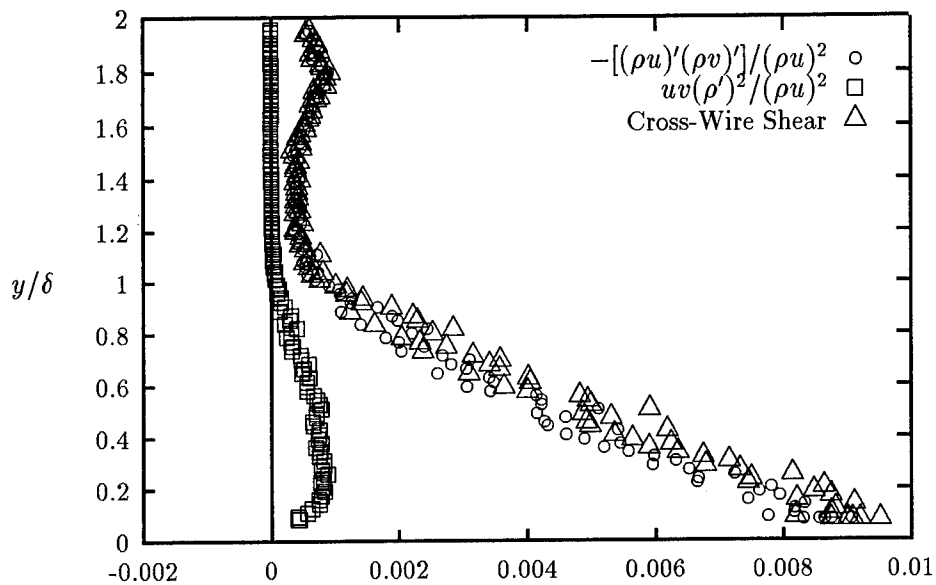


Figure 5.28 UV Probe Shear (x = 71.5 cm)

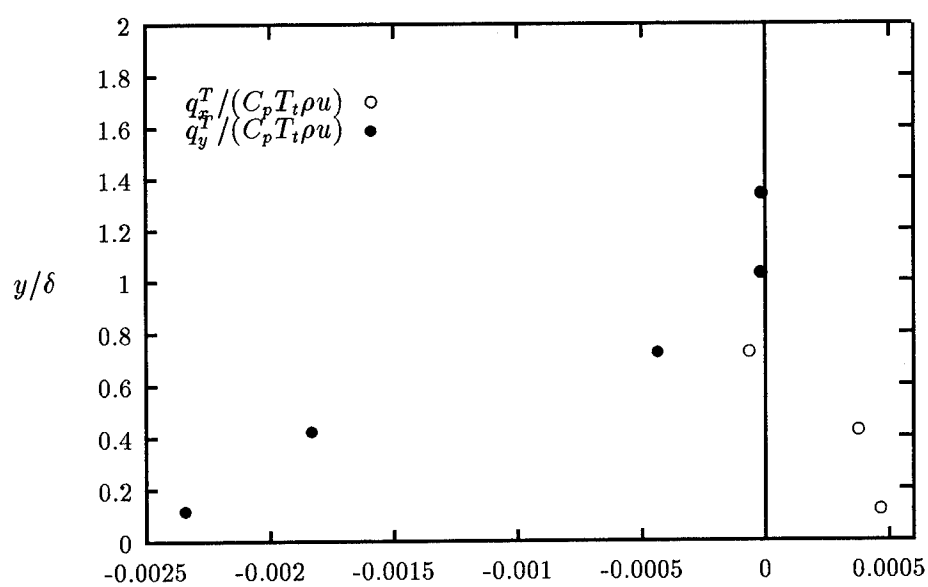


Figure 5.29 UV Probe Shear (x = 44 cm)

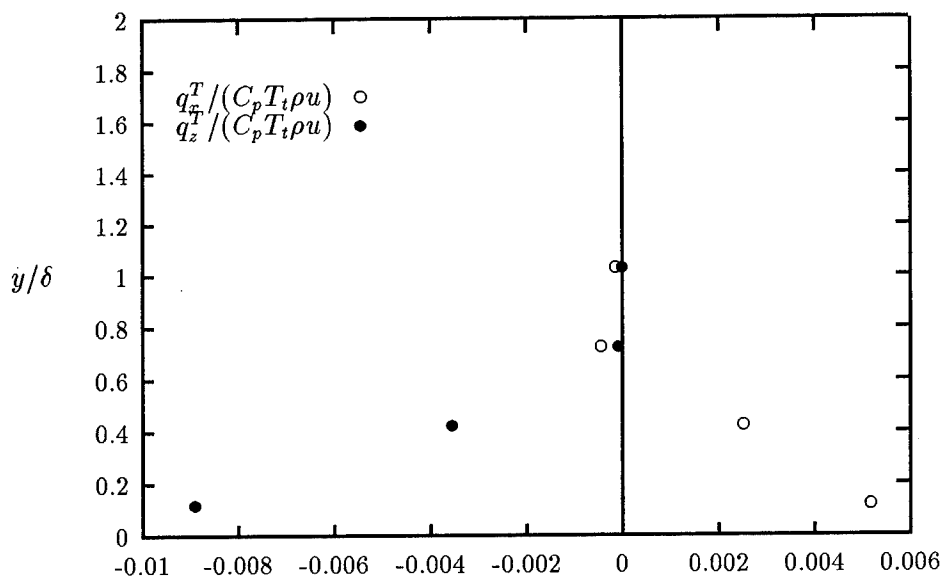


Figure 5.30 UW Probe Shear (x = 44 cm)

# VI. Conclusions and Recommendations

## 6.1 Conclusions

The importance of compressibility and the effect of pressure gradient on the turbulent flow structure in a Mach 2.9 boundary layer were investigated experimentally. Consistently, terms involving density fluctuations are shown to be important in both the zero and favorable pressure gradient regions.

This effect manifests itself in the $\overline{u}_i\overline{\rho' u'_j}$ term appearing in the RANS, accounting for as much as 67% of the total shear stress (irrespective of pressure gradient). The first two terms in $\tau_{xy}$ do not behave in a linear manner but combine to create an overall linear total through the boundary layer. The shear, $\tau_{xy}$, is remarkably linear through most of the boundary layer with a slope upstream of approximately $-182$ and downstream of $-109$. The upstream value is approximately zero in the freestream and estimated as .0008 downstream.

In addition, the fluctuating components in the energy equation may be of similar importance. The terms in the energy equation $\bar{h}_o\overline{\rho' u'_i}$ and $\bar{u}_i\overline{\rho' h'_o}$ may be significant because they contain the density fluctuation. The FANS equations again do not contain terms involving explicit mention of the density fluctuation component in the energy equation.

The density fluctuation terms in the stress calculations are a significant component of the shear stress. The lack of an explicit term in the FANS equations to account for this fluctuation demonstrates the difficulty of modeling density fluctuations in the FANS based CFD solutions. CFD methods should account for compressibility effects explicitly in order to more accurately model the high speed turbulent flow regime. Through the FANS form of the N-S equation is more straightforward to model numerically, most experimental techniques measure RANS-type terms. Thus, in flow situations where the importance of compressibility and pressure gradient can be identified, the incorporation of this information into turbulent models is more suited for RANS applications. Thus if the interest is to develop more accurate closure models based on this data, a RANS approach may be most useful.

The assumption that $\kappa = 1.0$ suggested by in the Strong Reynolds analogy is not universally applicable. Overheat ratios of about 1.6 are likely candidates for the use of $\kappa = 1.0$. On the other hand this investigation has found if the overheat ratio is near 2.0 a $\kappa \approx 0.0$ is more appropriate. The study overheat ratios of 1.6 for the UV data matched the MOH data best when the value of 1.0 was used. However, when the overheat ratios were 2.2 the value of $\kappa$ of 0.0 matched the MOH best. The Strong Reynolds analogy is correct that if a moderate overheat ratio is used that 1.0 is an ideal number for matching SOH and MOH data, but as the overheat level becomes higher the sensitivity of the data to $\kappa$ decreases, therefore use of the Strong Reynolds analogy was only necessary at the lower overheat ratios.

### *6.2 Recommendations*

To further quantify the effect of a favorable pressure gradient, measurements should be obtained of a zero pressure gradient boundary layer at the same location as where the favorable pressure gradient measurements were conducted (71.5 cm). In this way, changes in turbulence intensities and shear stress due only to the evolution of the boundary layer in the absence of pressure gradients could be extracted, and a truer measure of the role of the pressure gradient obtained.

LDV (Laser Doppler Velocimetry) measurements of same flow should be conducted in order to assess the effect of the hot-wire probes on the flow field.

The use of higher overheat ratios in the SOH data portion of this experiment would remove the need for a $\kappa$ other than zero. The data of the SOH would match the MOH data more closely without data matching between the MOH and the SOH data. Because the lower overheat ratios provided a better picture of the temperature fluctuations. overheat values and the range of the MOH should have spanned the overheat levels more fully, i.e. from 1.1 up to 2.2 if possible.

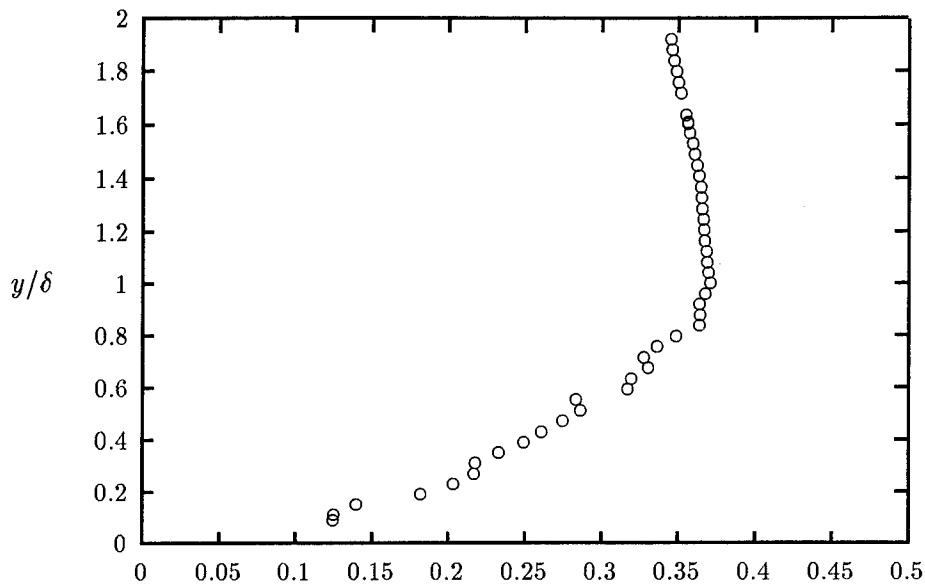


Figure A.1 Upstream Pressure Profile $P_{t2}/P_{t1}$ x = 44 cm

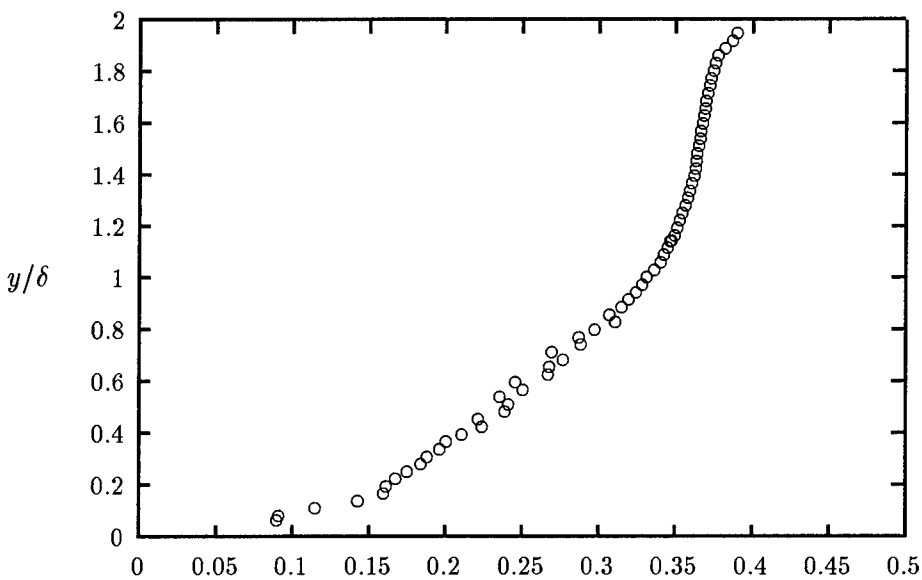


Figure A.2 Test Section Pressure Profile $P_{t2}/P_{t1}$ x = 71.5 cm

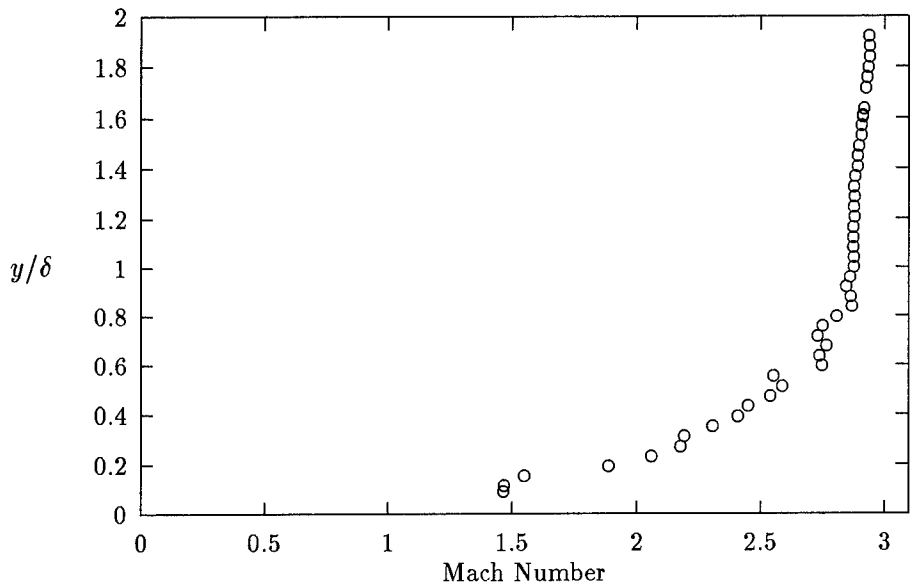


Figure A.3 Mach Profile (x = 44 cm)

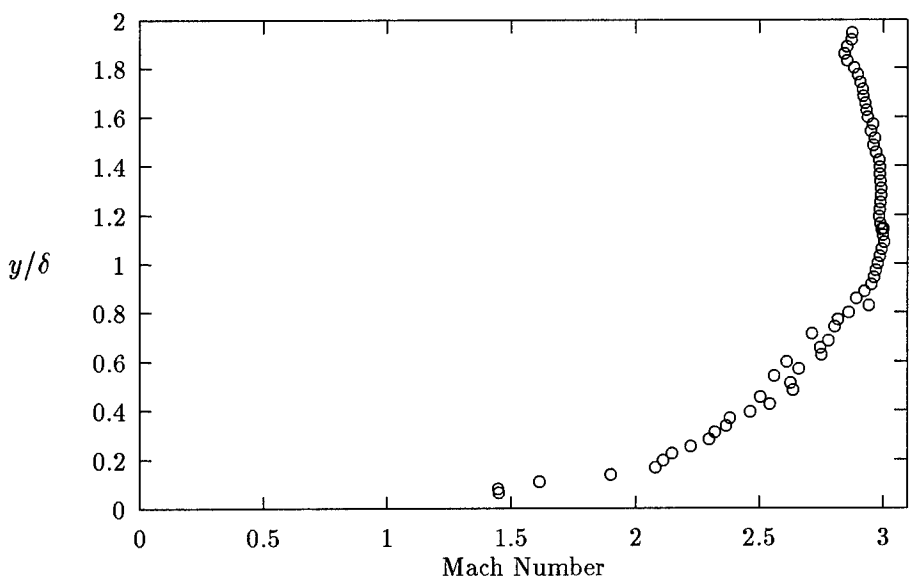


Figure A.4 Mach Profile (x = 71.5 cm)

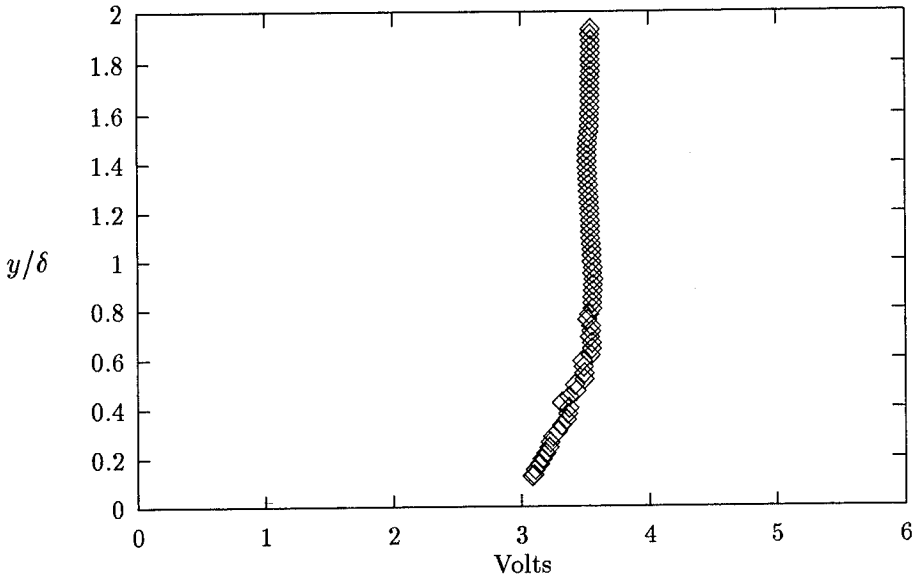


Figure B.1 UV Mean Voltage Wire 1(x = 44 cm)

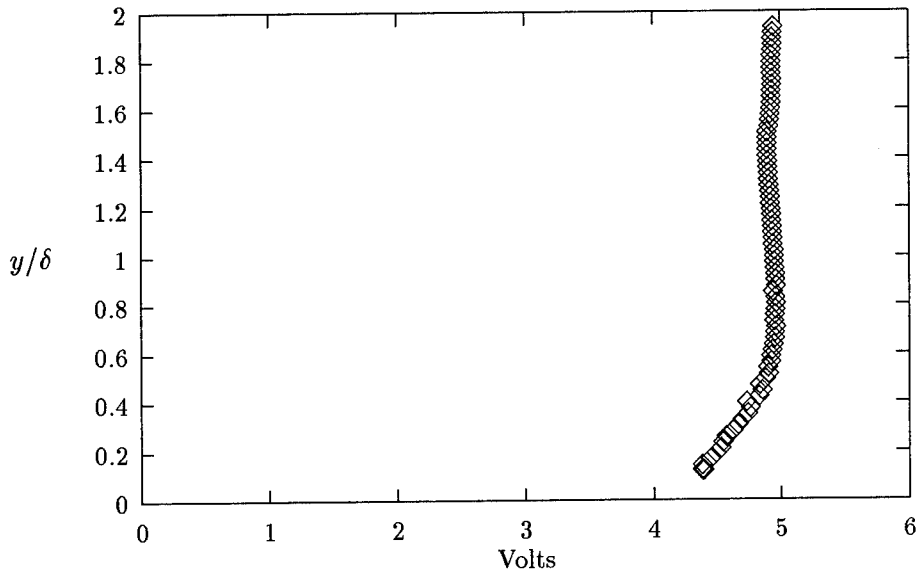


Figure B.2 UW Mean Voltage Wire 1(x = 44 cm)

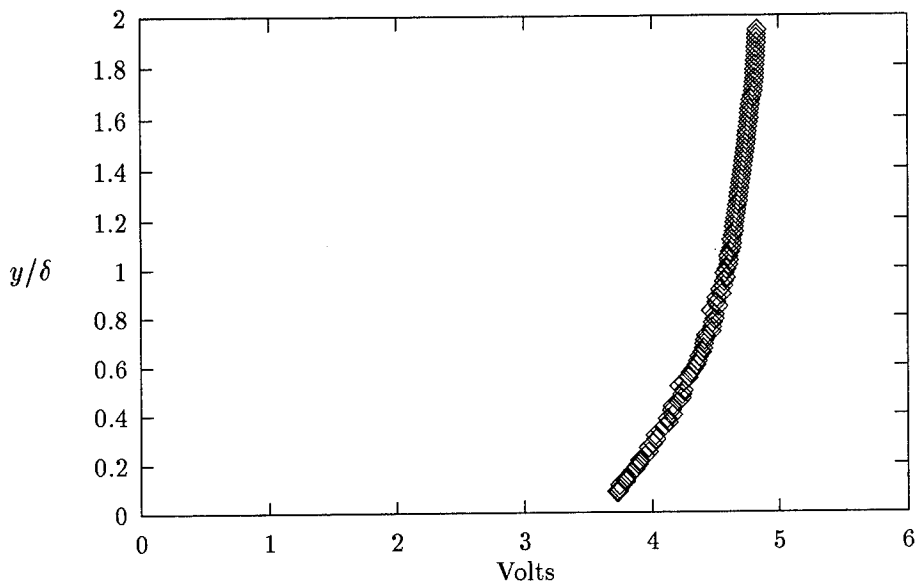


Figure B.3 UV Mean Voltage Wire 1(x = 71.5 cm)

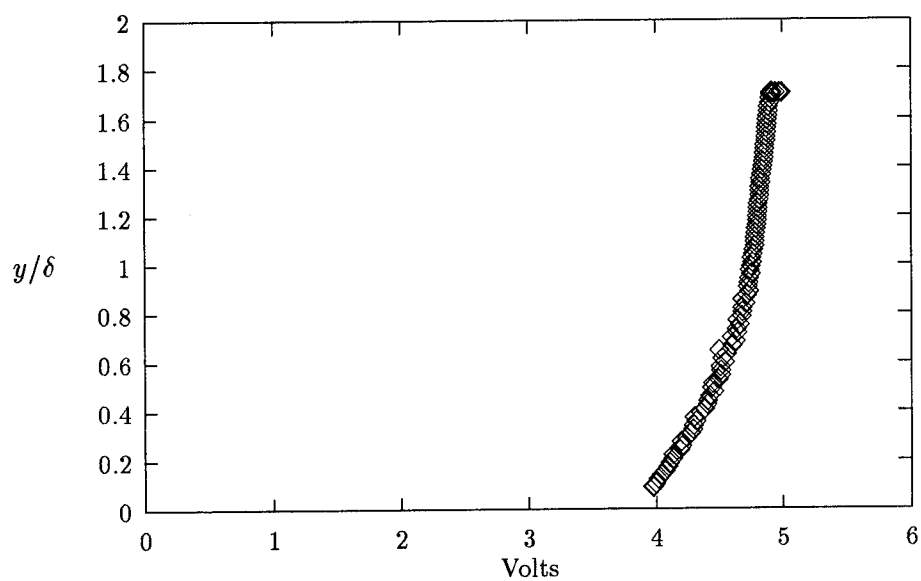


Figure B.4 UW Mean Voltage Wire 1(x = 71.5 cm)

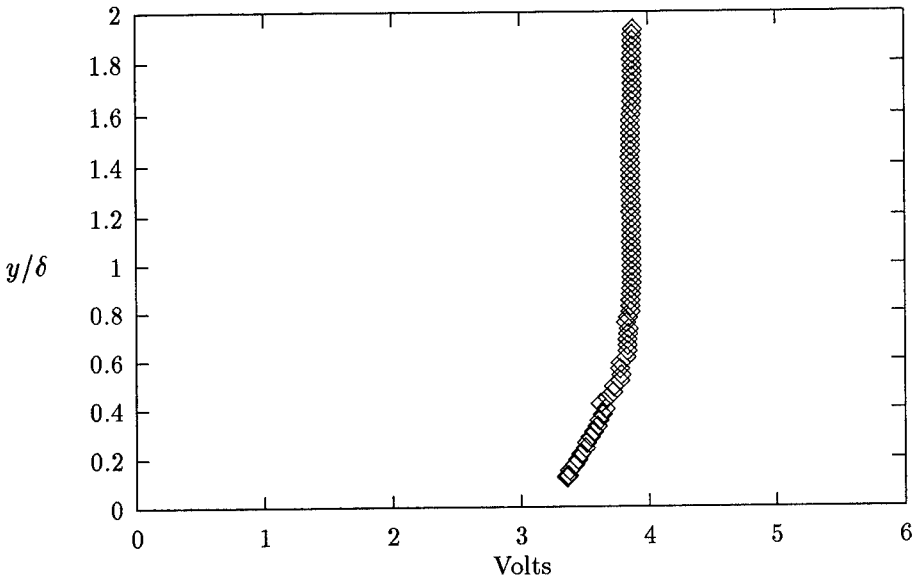


Figure B.5 UV Mean Voltage Wire 2(x = 44 cm)

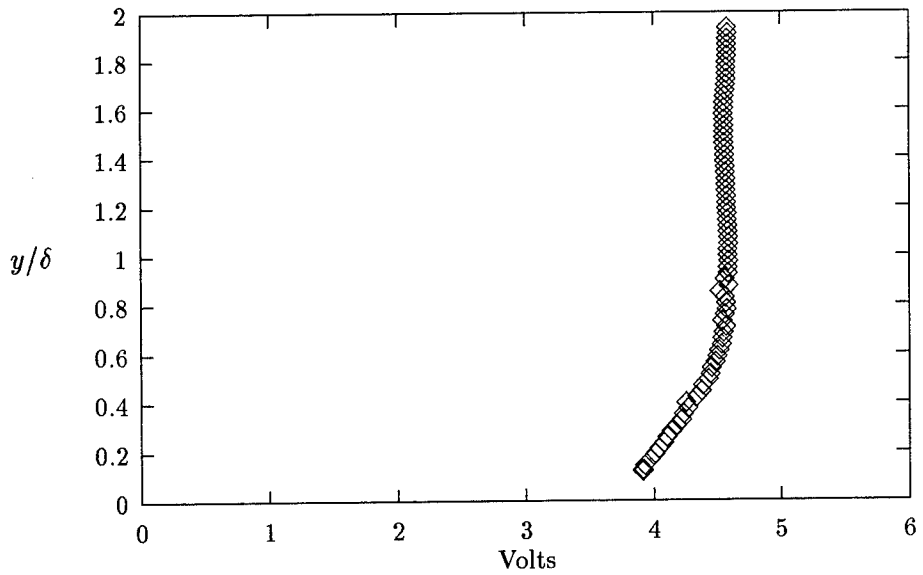


Figure B.6 UW Mean Voltage Wire 2(x = 44 cm)

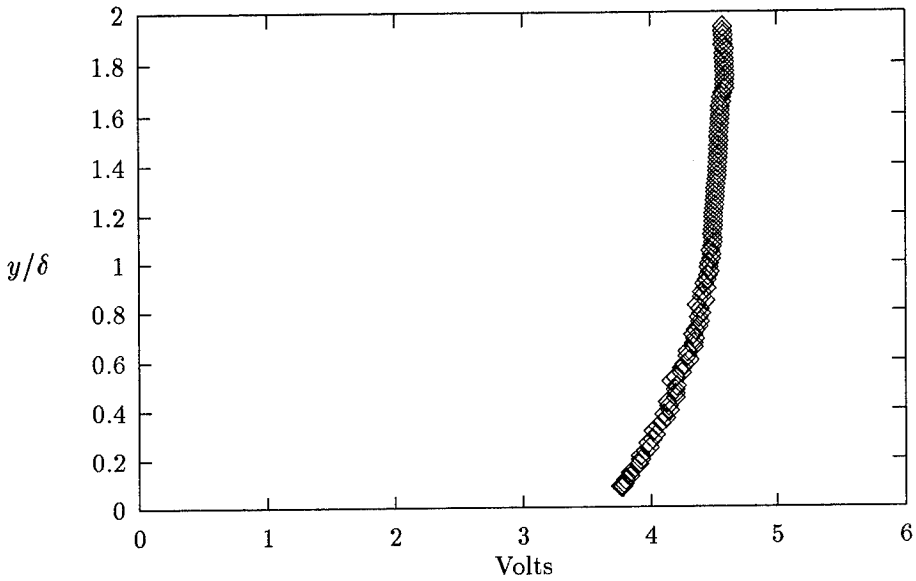


Figure B.7 UV Mean Voltage Wire 2(x = 71.5 cm)

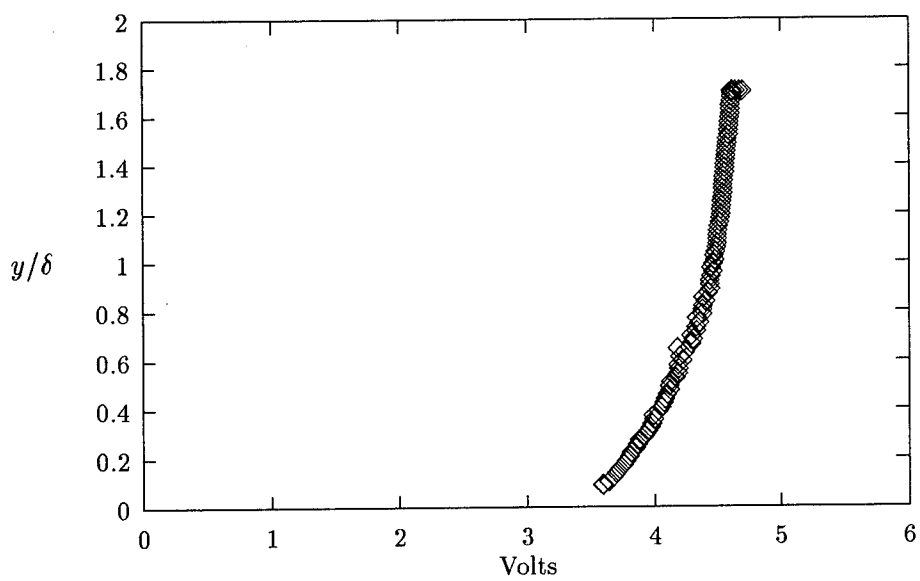


Figure B.8 UW Mean Voltage Wire 2(x = 71.5 cm)

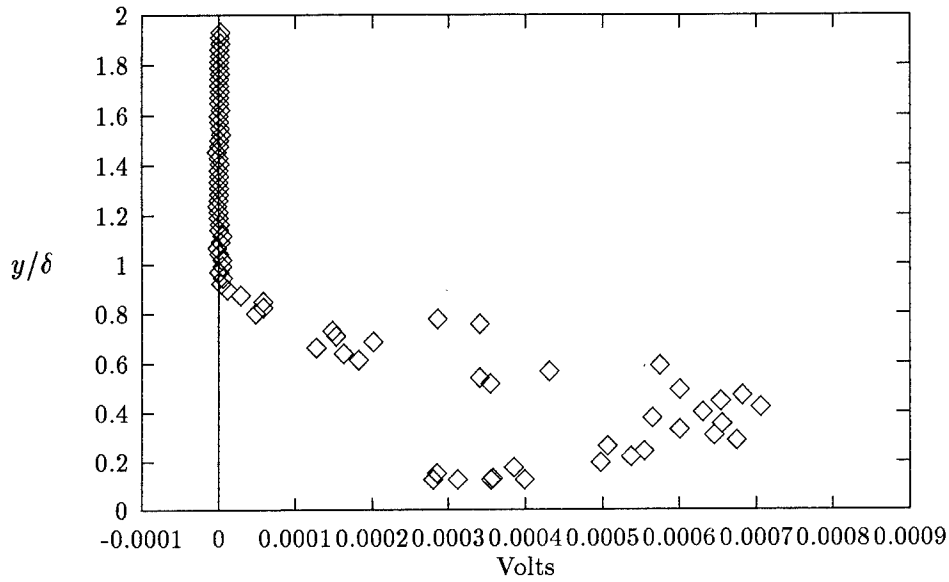


Figure C.1 UV Cross Correlation Voltage(x = 44cm)

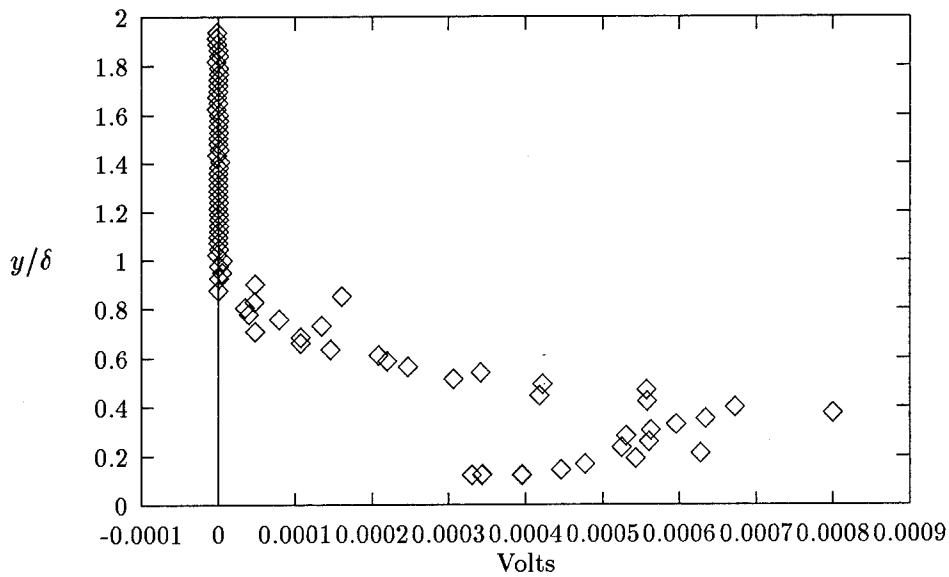


Figure C.2 UW Cross Correlation Voltage(x = 44cm)

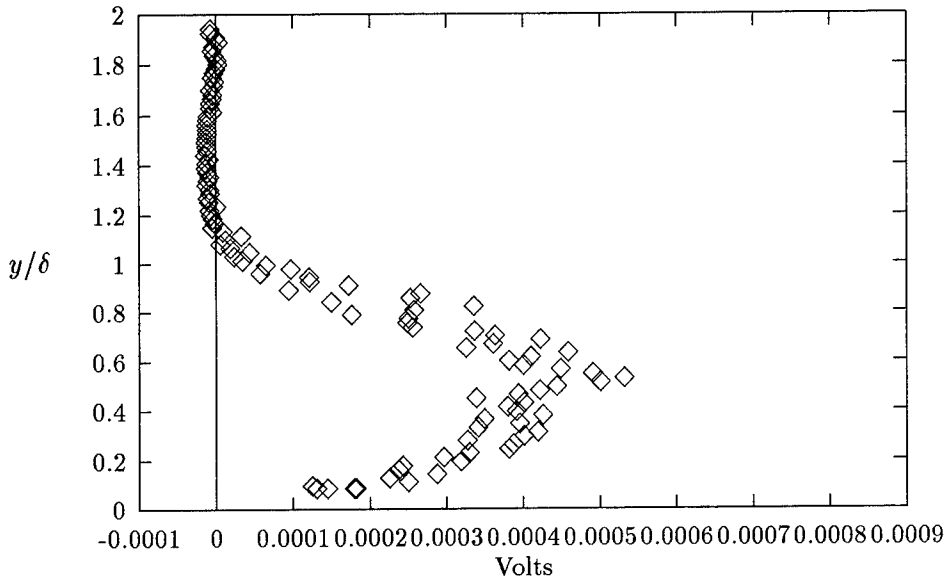


Figure C.3 UV Cross Correlation Voltage(x = 71.5cm)

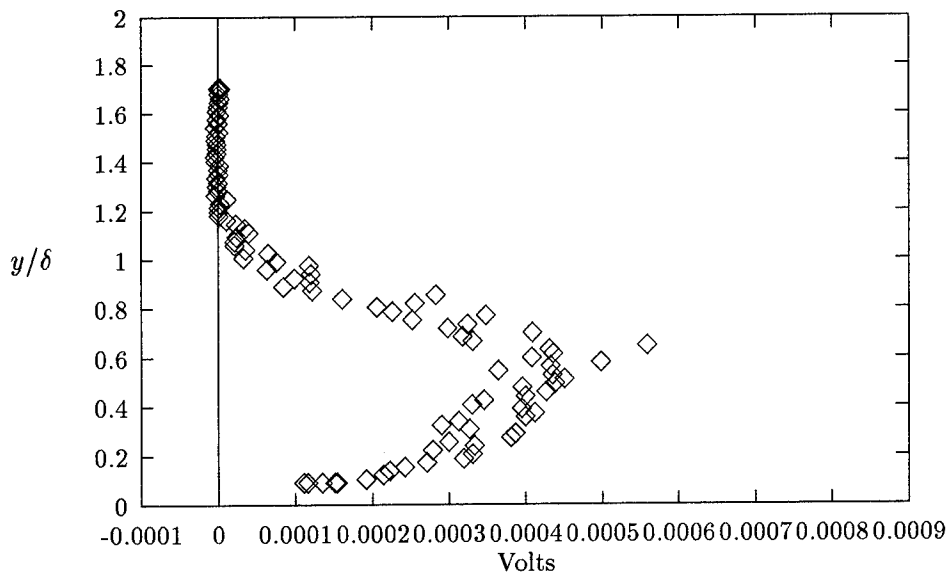


Figure C.4 UW Cross Correlation Voltage(x = 71.5cm)

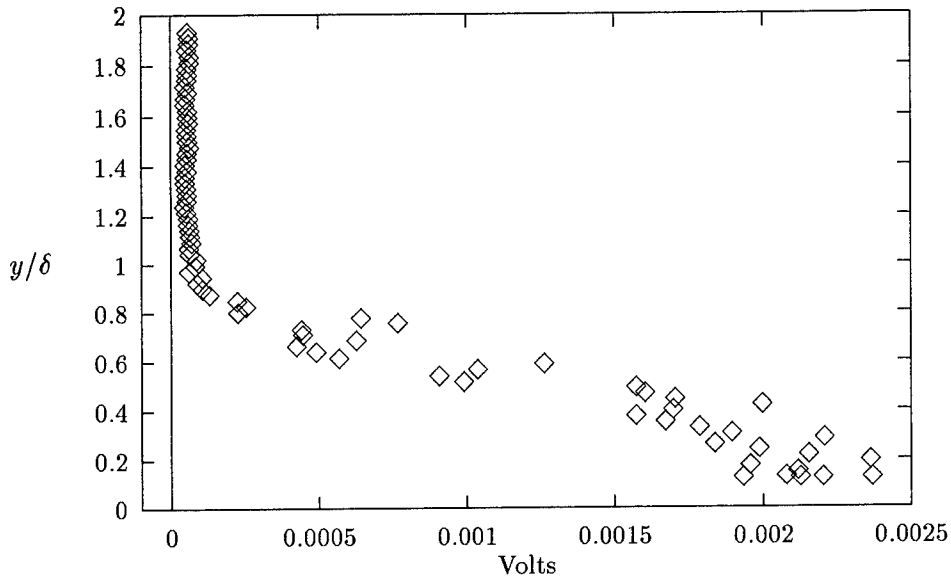


Figure D.1 UV RMS Voltage Wire 1(x = 44 cm)

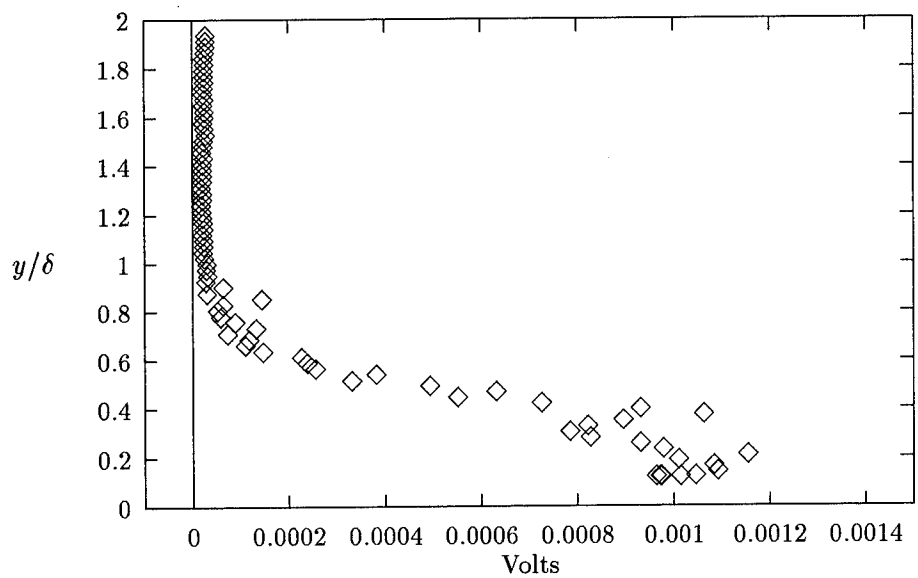


Figure D.2 UW RMS Voltage Wire 1(x = 44 cm)

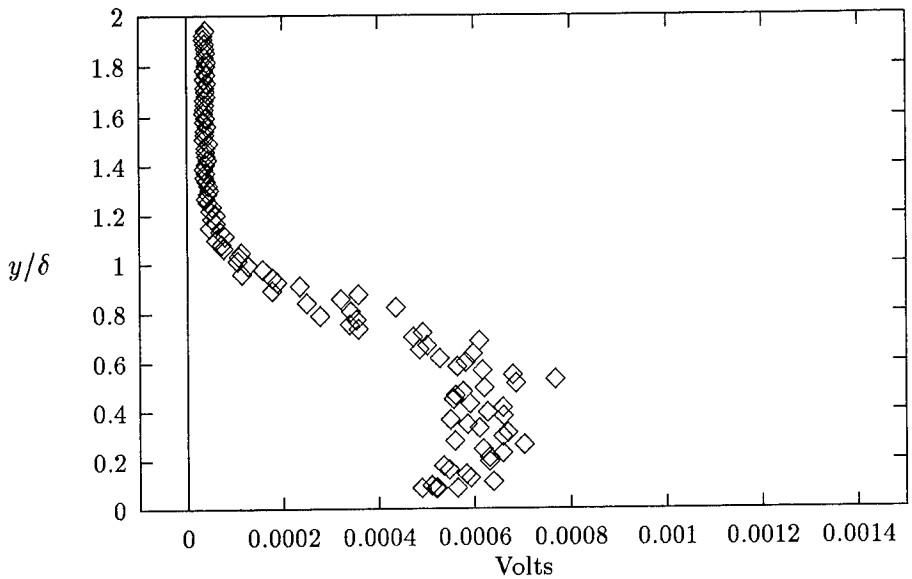


Figure D.3 UV RMS Voltage Wire 1(x = 71.5 cm)

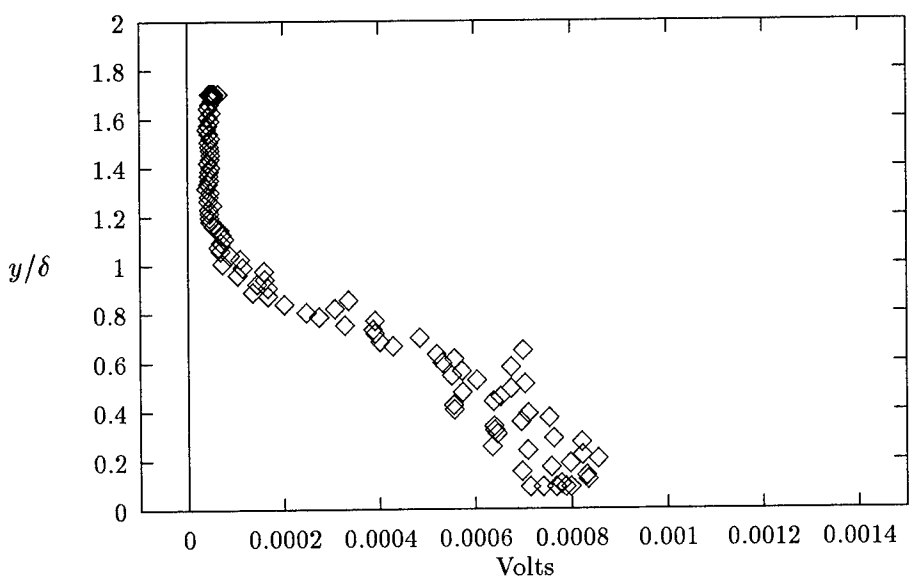


Figure D.4 UW RMS Voltage Wire 1(x = 71.5 cm)

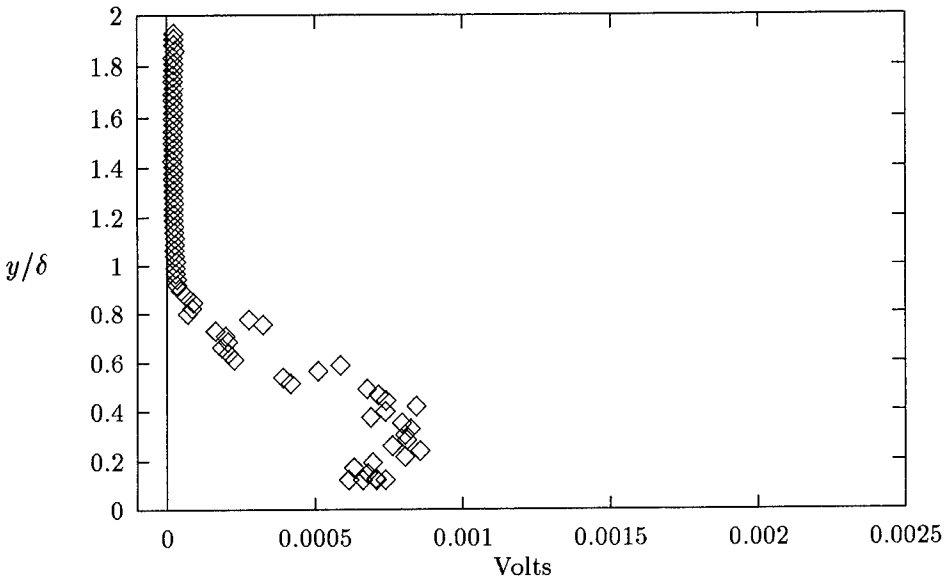


Figure D.5 UV RMS Voltage Wire 2(x = 44 cm)

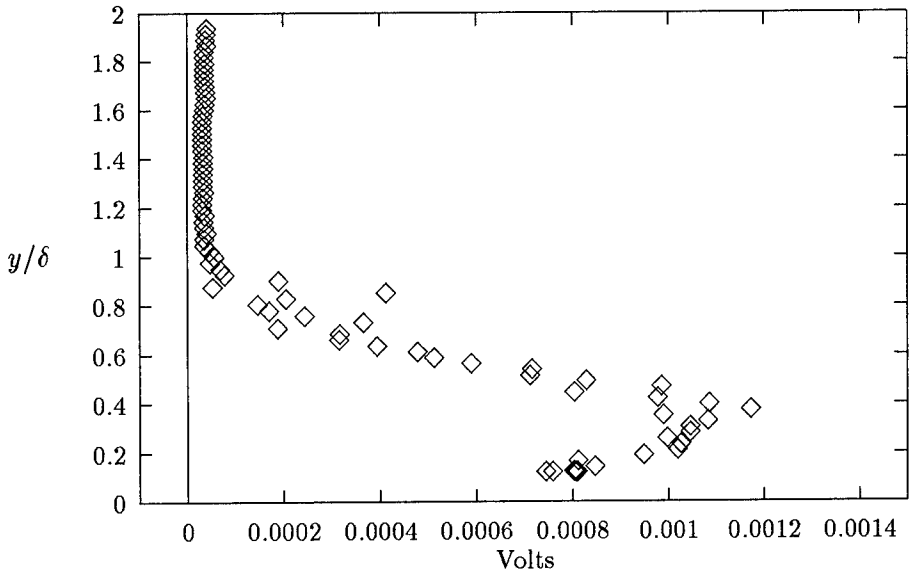


Figure D.6 UW RMS Voltage Wire 2(x = 44 cm)

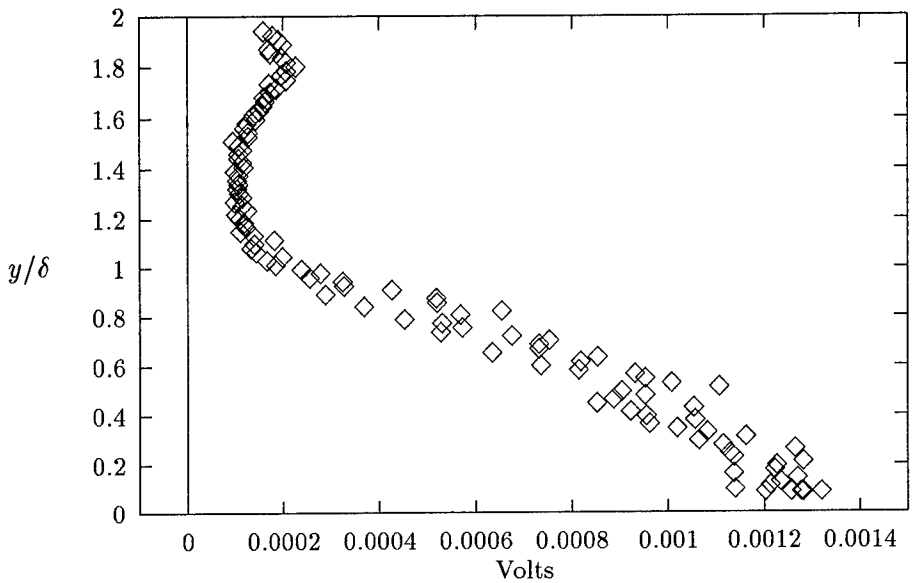


Figure D.7 UV RMS Voltage Wire 2(x = 71.5 cm)

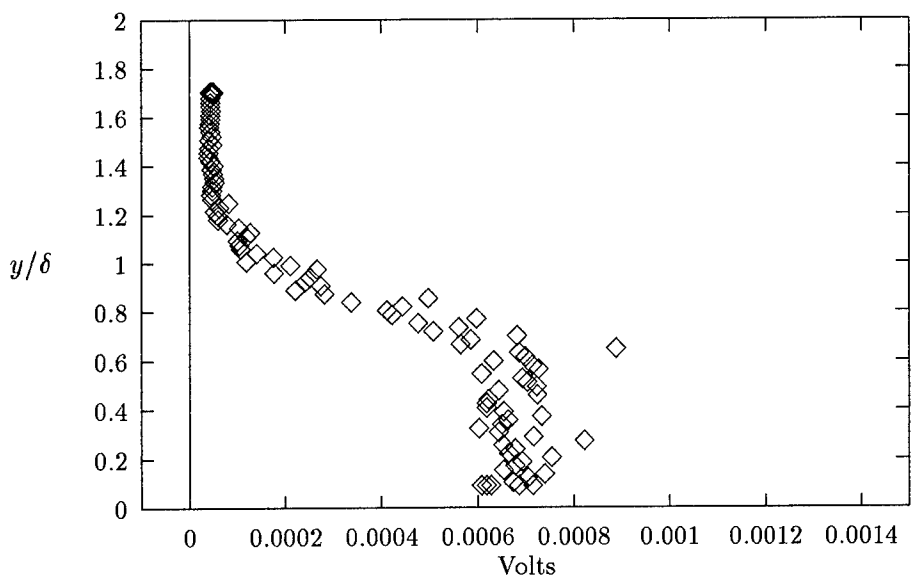


Figure D.8 UW RMS Voltage Wire 2(x = 71.5 cm)

*Appendix E. Turbulence Intensities and Separated Turbulence Intensities*

## *E.1 Turbulence Intensities*

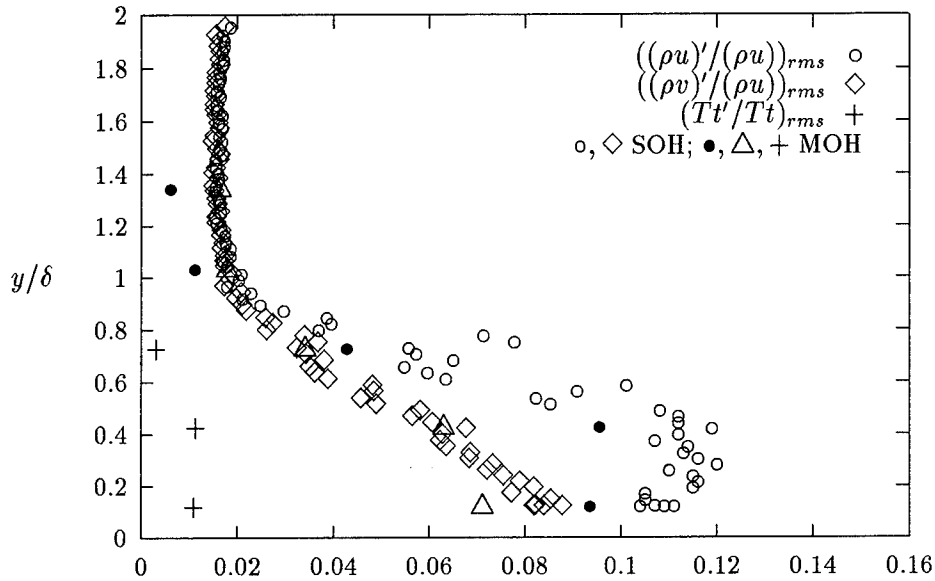


Figure E.1 UV Probe Turbulence Intensities (x = 44 cm)

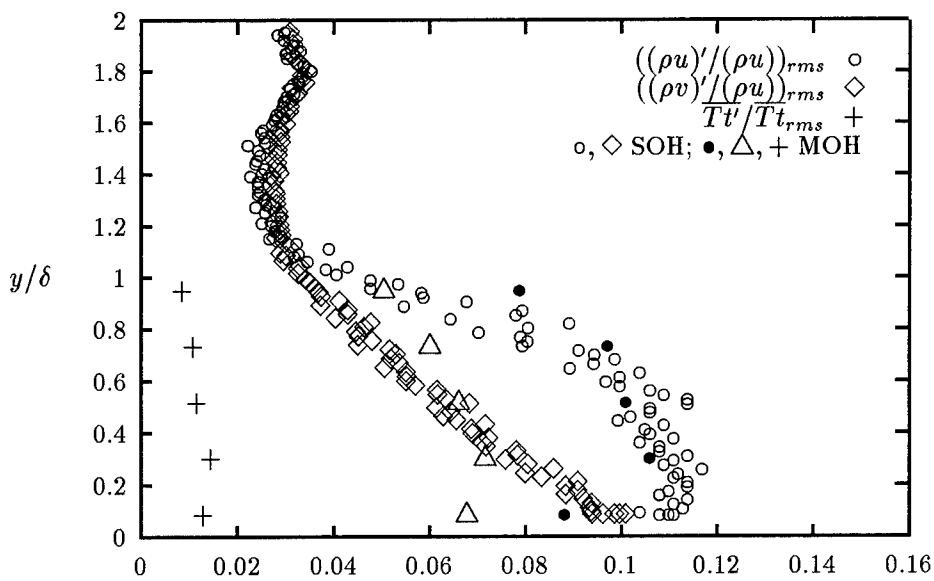


Figure E.2 UV Probe Turbulence Intensities (x = 71.5 cm)

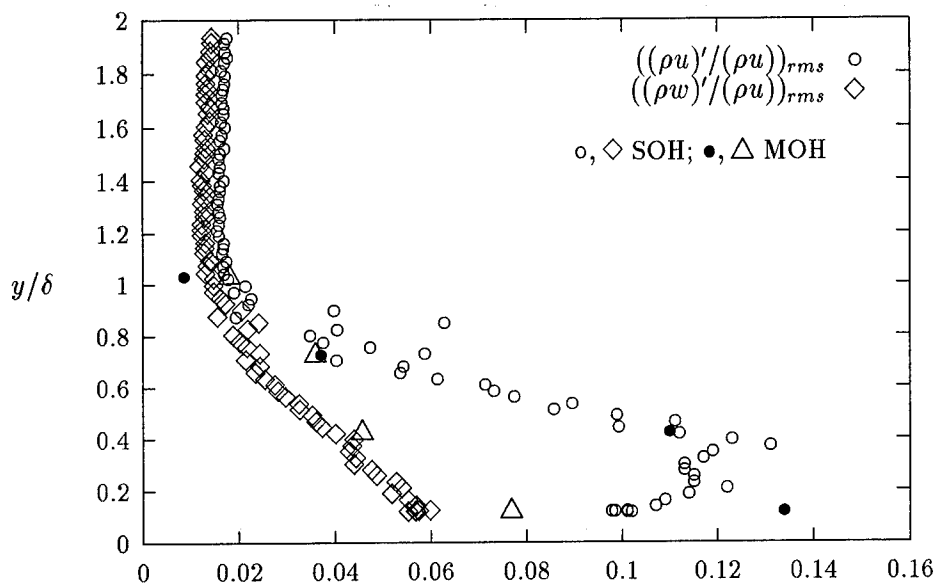


Figure E.3 UW Probe Turbulence Intensities (x = 44 cm)

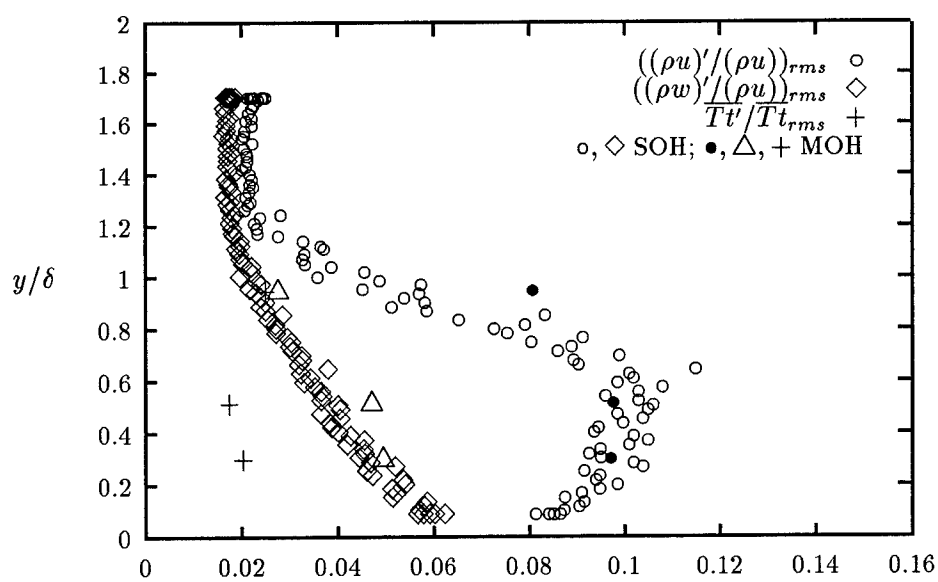


Figure E.4 UW Probe Turbulence Intensities (x = 71.5 cm)

*E.2 Separated Turbulence Intensities*

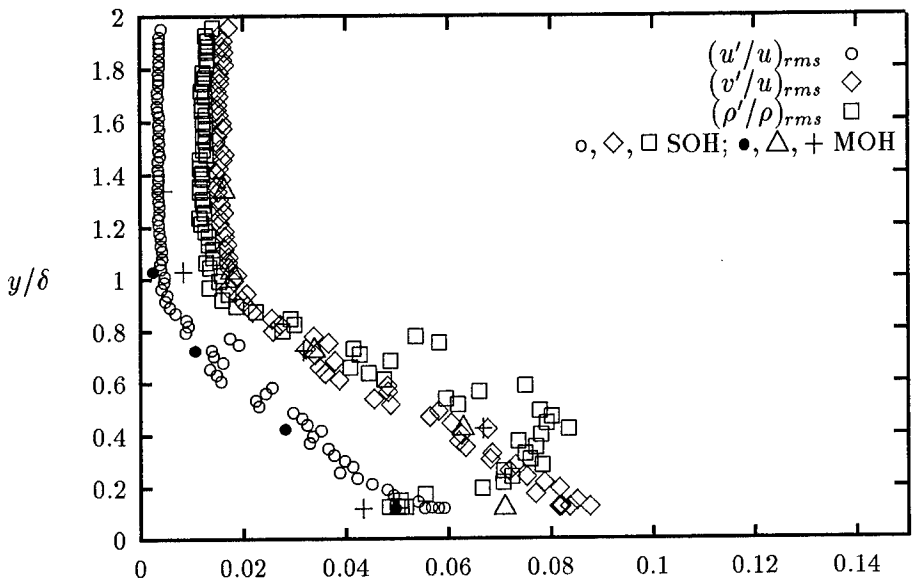


Figure E.5 UV Probe Separated Turbulence Intensities (x = 44 cm)

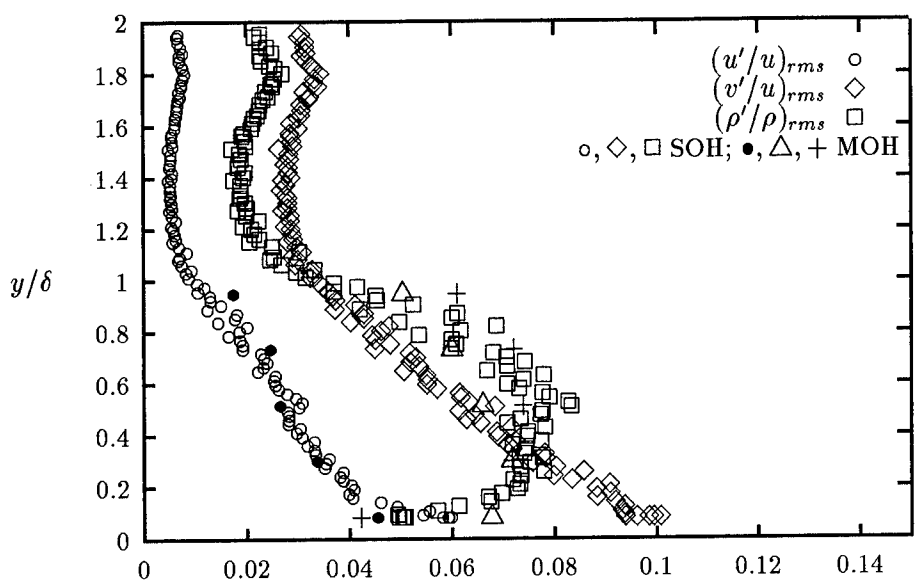


Figure E.6 UV Probe Separated Turbulence Intensities (x = 71.5 cm)

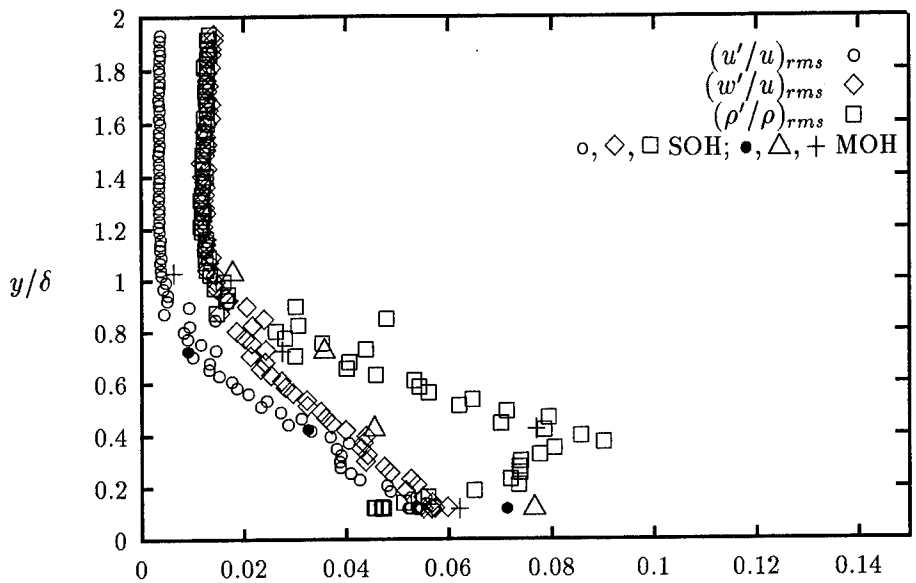


Figure E.7 UW Probe Separated Turbulence Intensities (x = 44 cm)

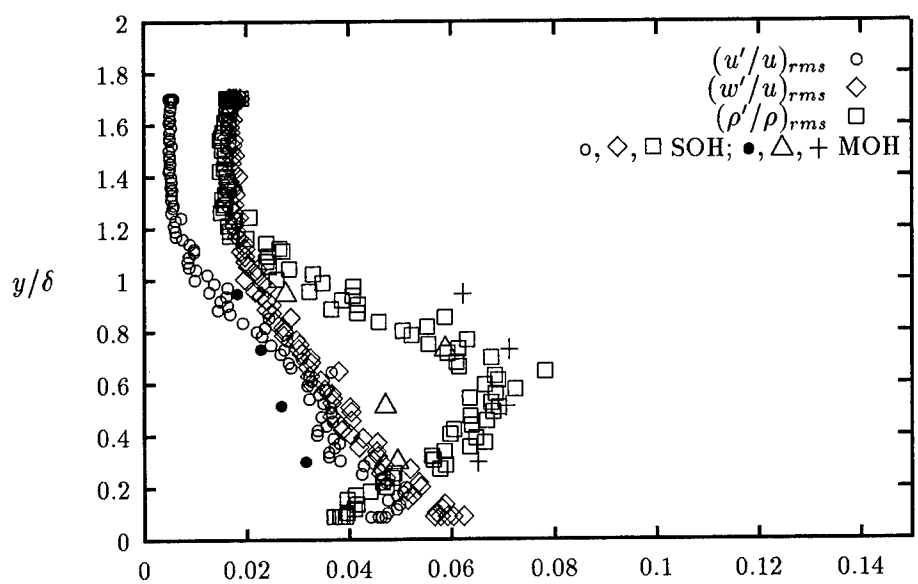


Figure E.8 UW Probe Separated Turbulence Intensities (x = 71.5 cm)

## *F.1 RANS*

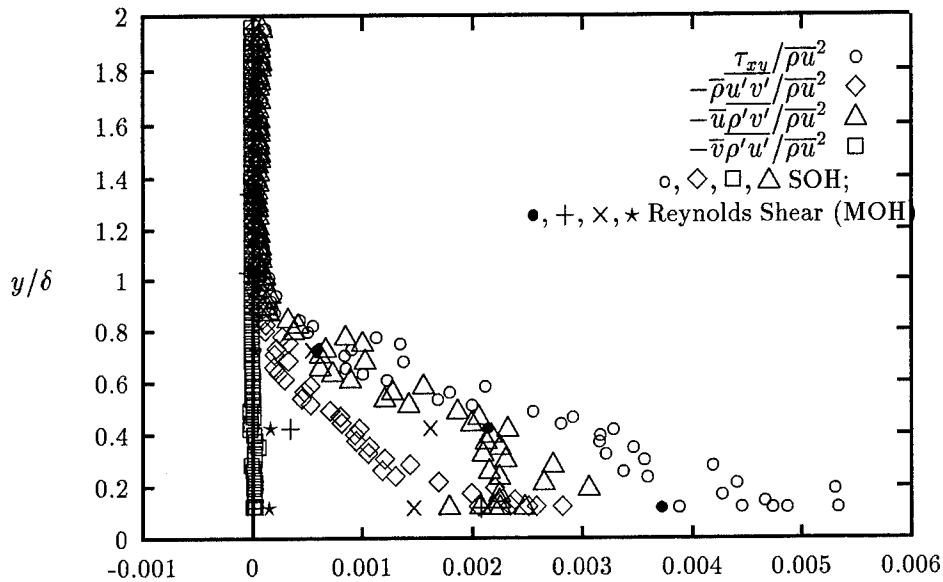


Figure F.1 UV Probe Shear (x = 44 cm)

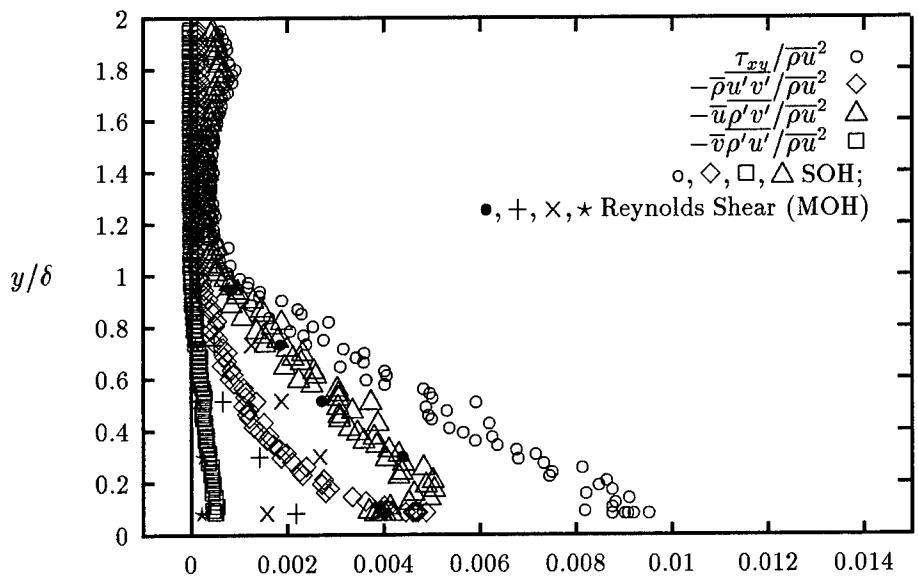


Figure F.2 UV Probe Shear (x = 71.5 cm)

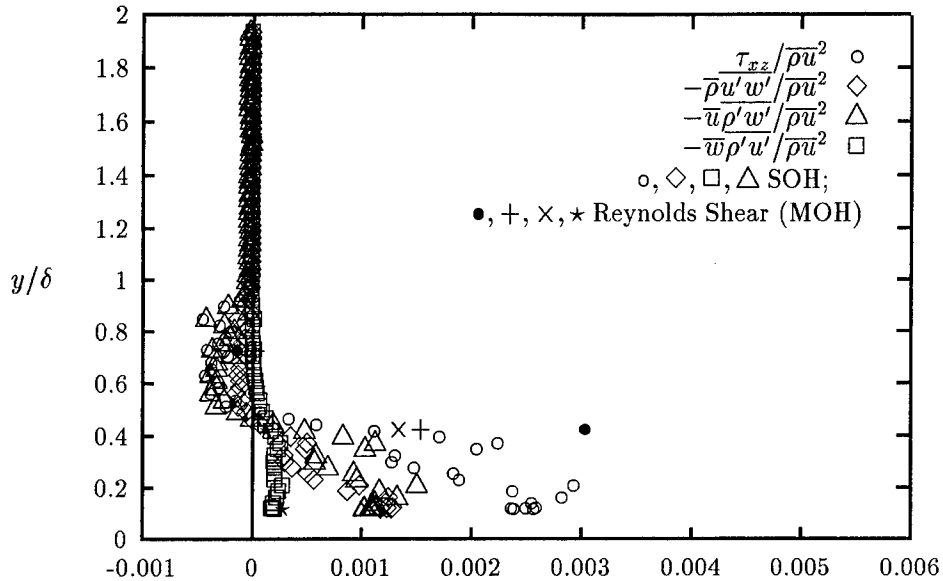


Figure F.3 UW Probe Shear (x = 44 cm)

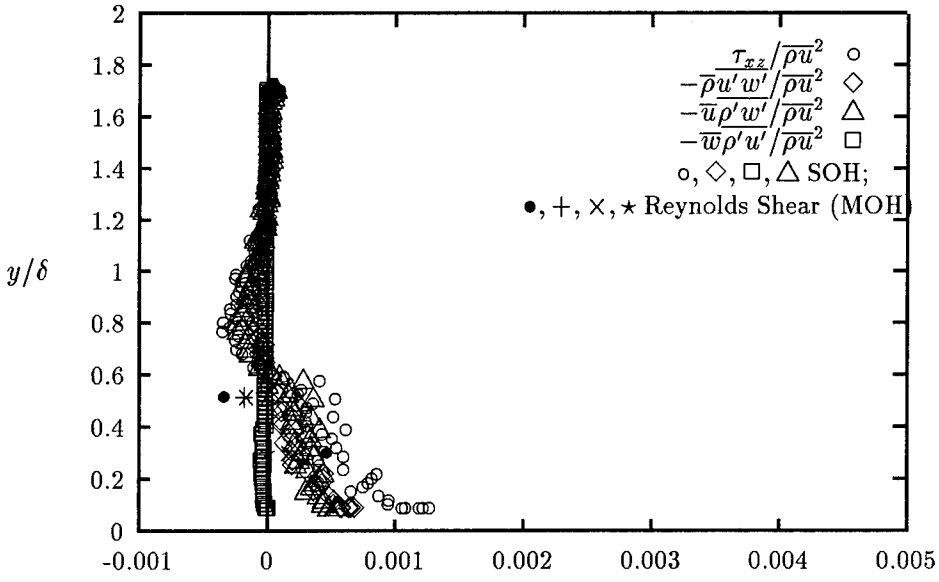


Figure F.4 UW Probe Shear (x = 71.5 cm)

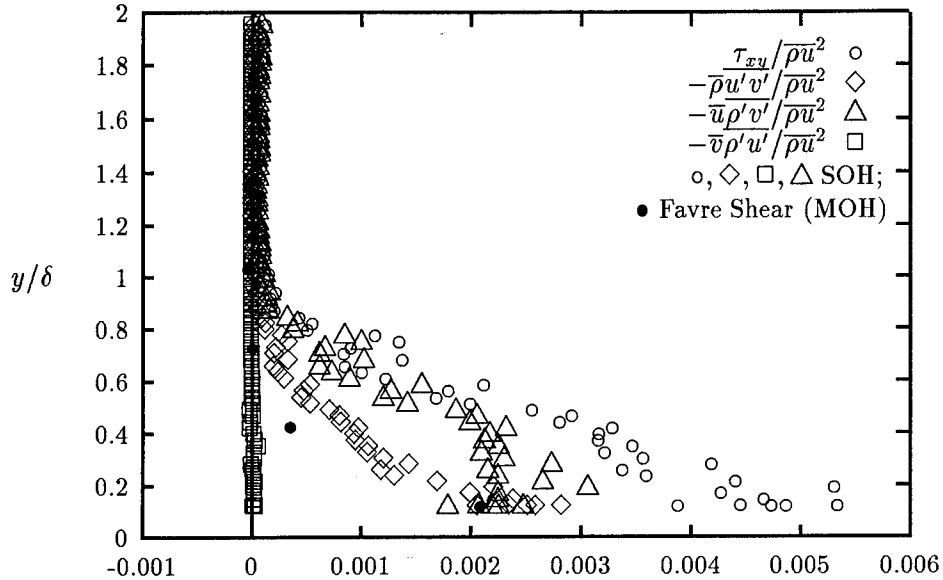


Figure F.5 UV Probe Shear (x = 44 cm)

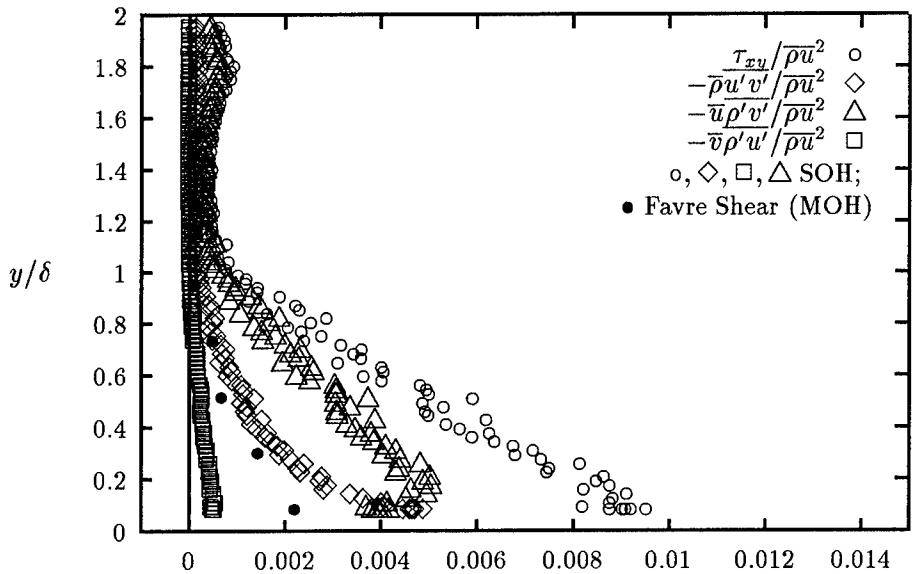


Figure F.6 UV Probe Shear (x = 71.5 cm)

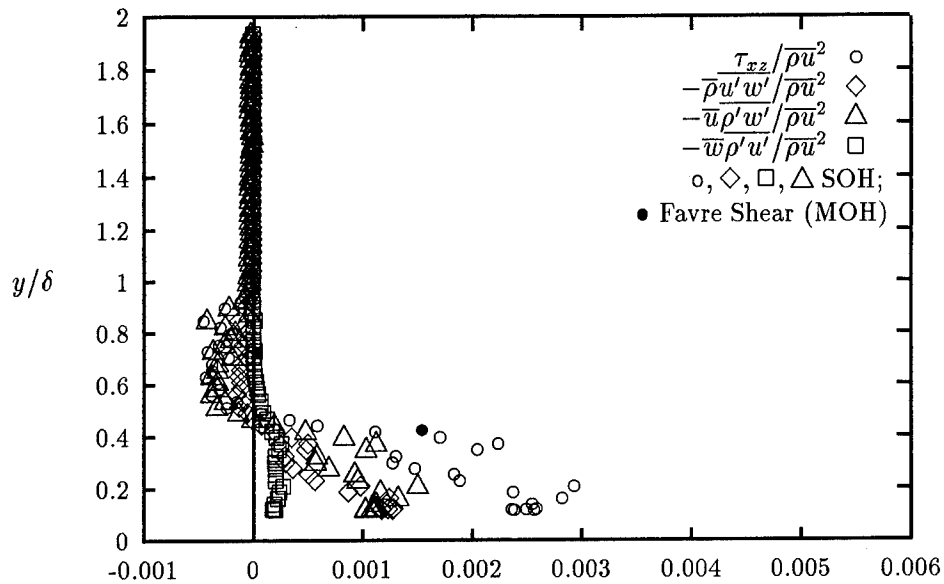


Figure F.7 UW Probe Shear (x = 44 cm)

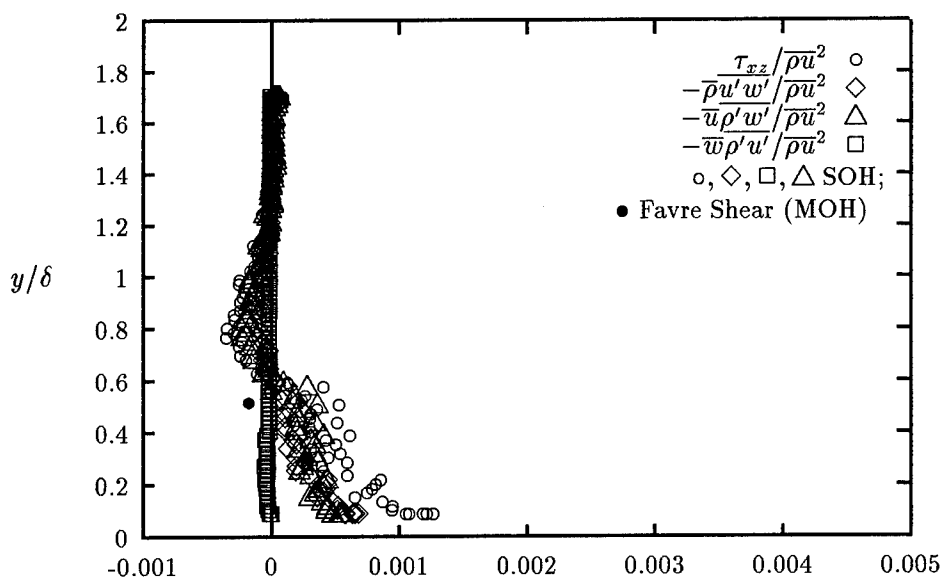


Figure F.8 UW Probe Shear (x = 71.5 cm)

*F.3 Plots of Cxy*

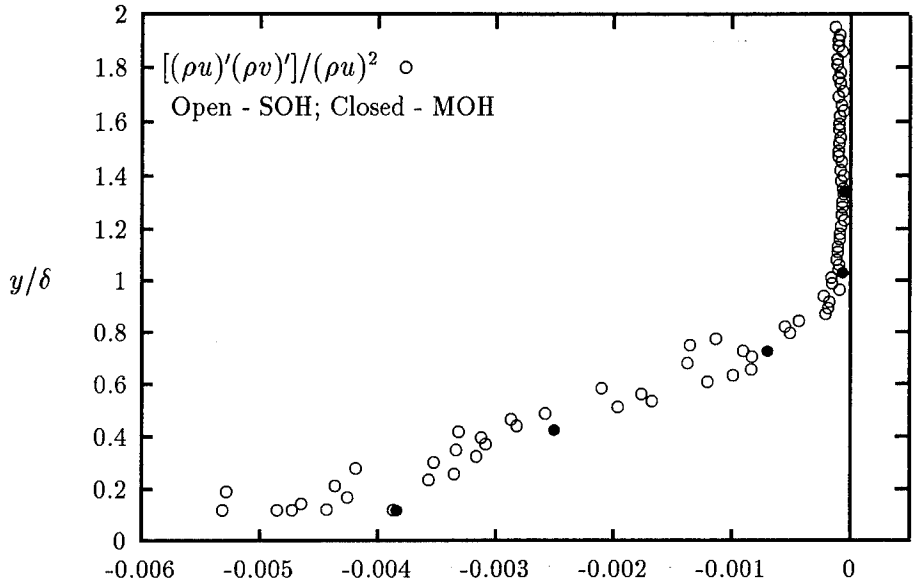


Figure F.9 UV Probe Shear (x = 44 cm)

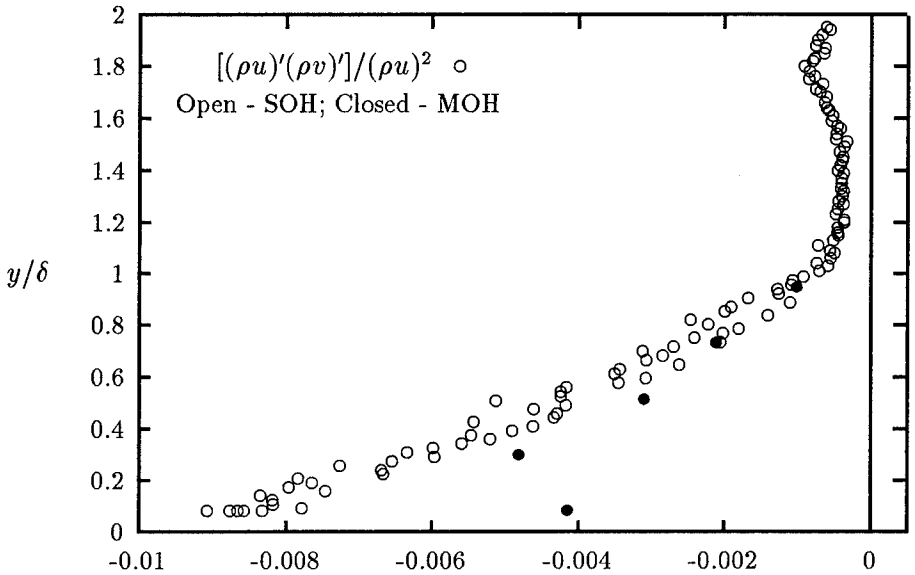


Figure F.10 UV Probe Shear (x = 71.5 cm)

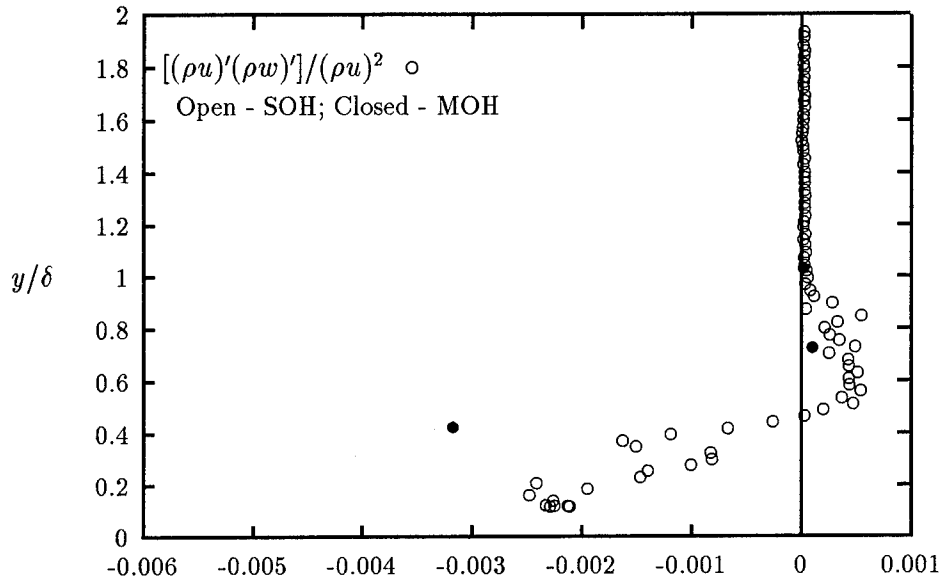


Figure F.11 UW Probe Shear (x = 44 cm)

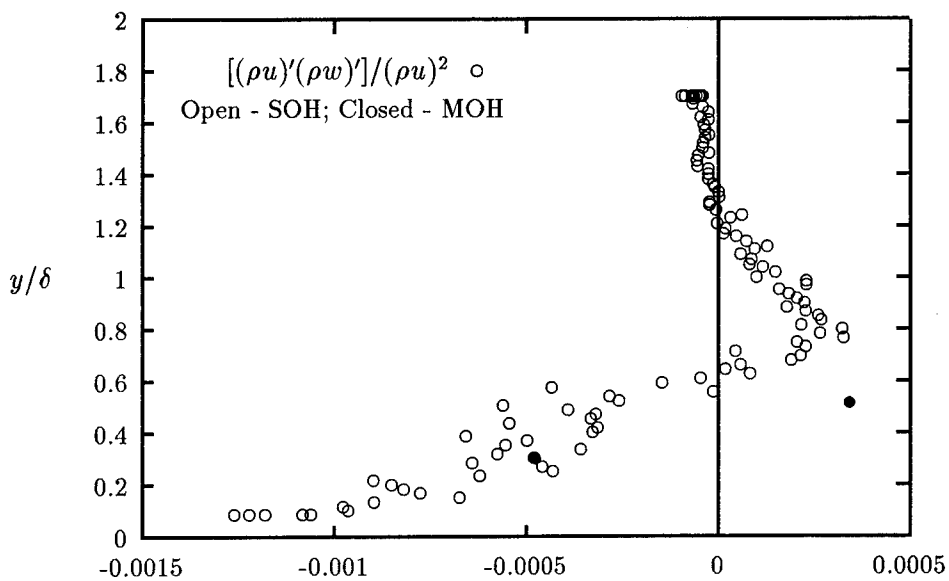


Figure F.12 UW Probe Shear (x = 71.5 cm)

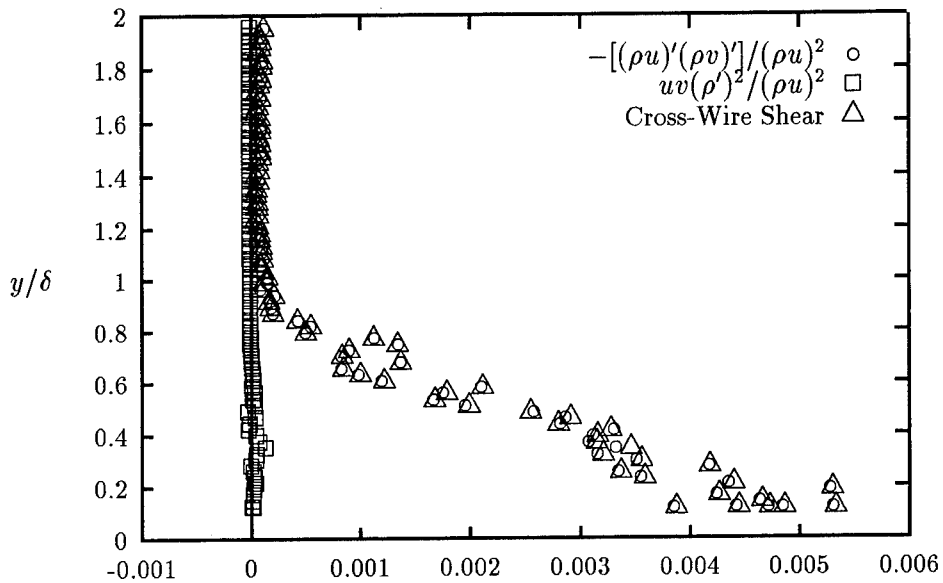


Figure G.1 UV Probe Shear (x = 44 cm)

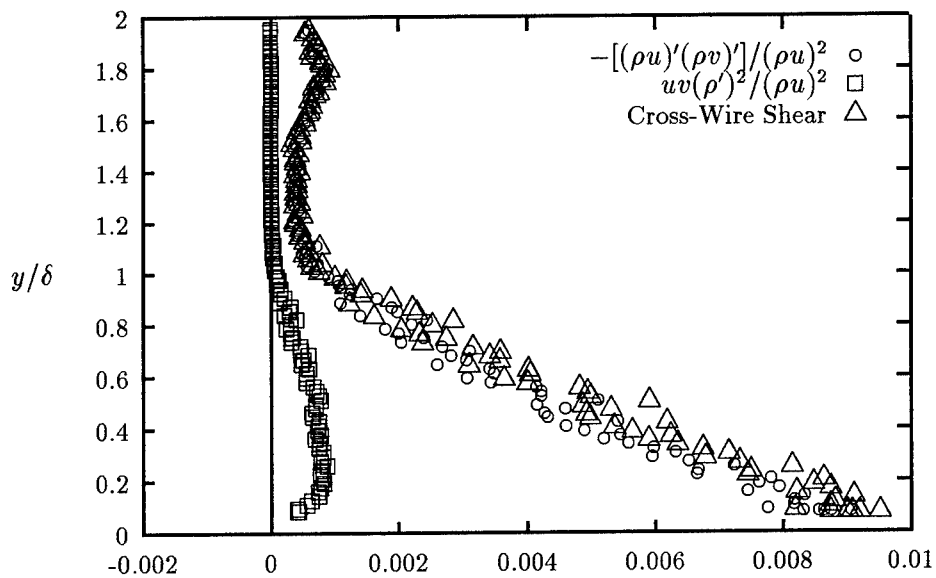


Figure G.2 UV Probe Shear (x = 71.5 cm)

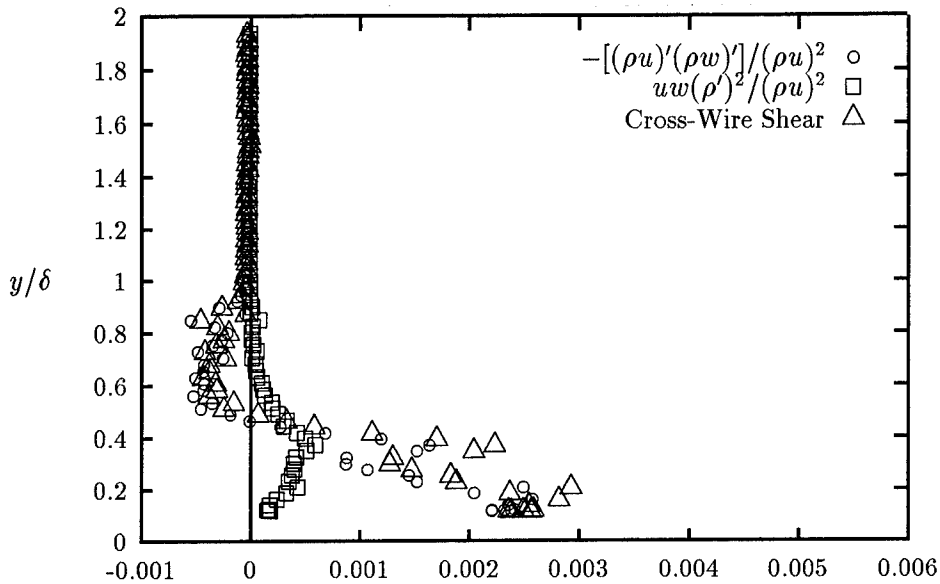


Figure G.3 UW Probe Shear (x = 44 cm)

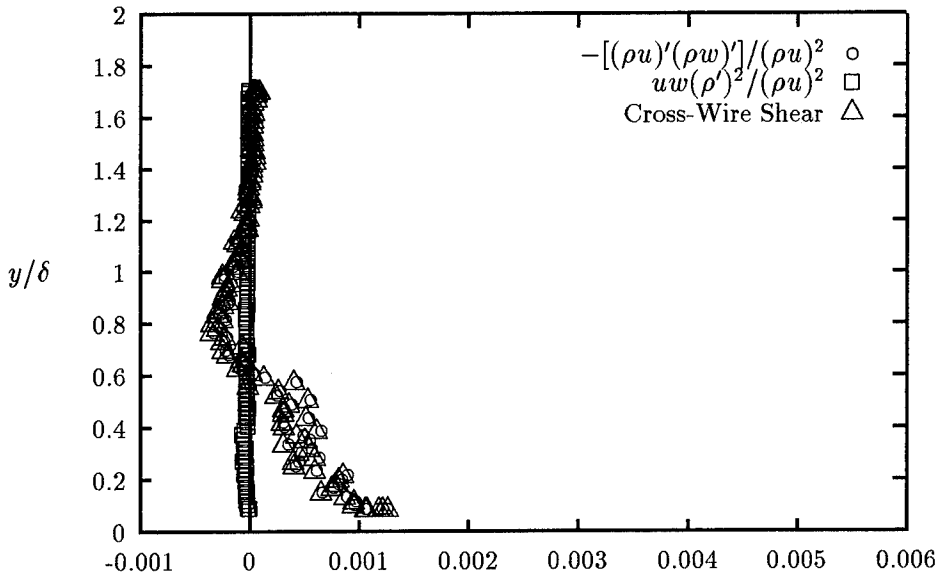


Figure G.4 UW Probe Shear (x = 71.5 cm)

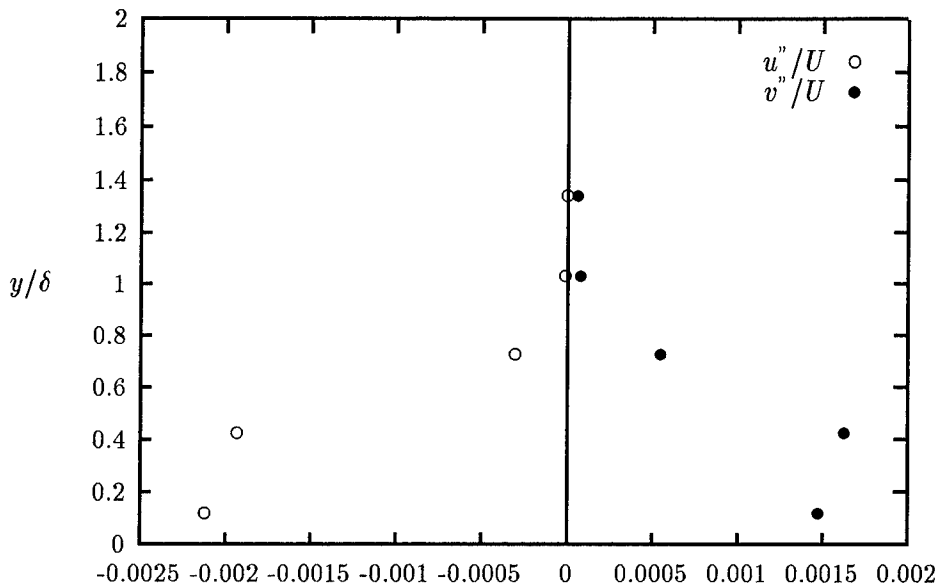


Figure H.1 UV Separated Turbulence Intensities (x = 44 cm)

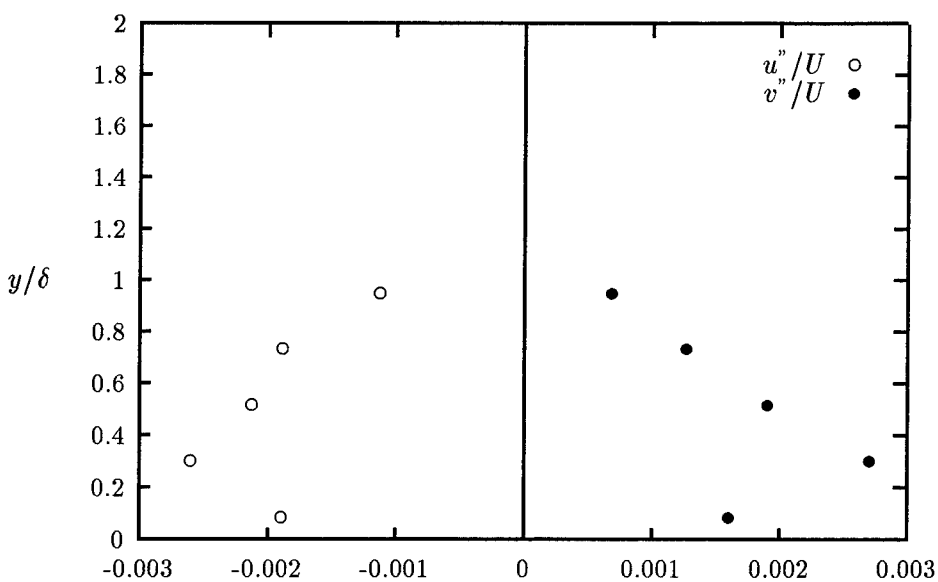


Figure H.2 UV Separated Turbulence Intensities (x = 71.5 cm)

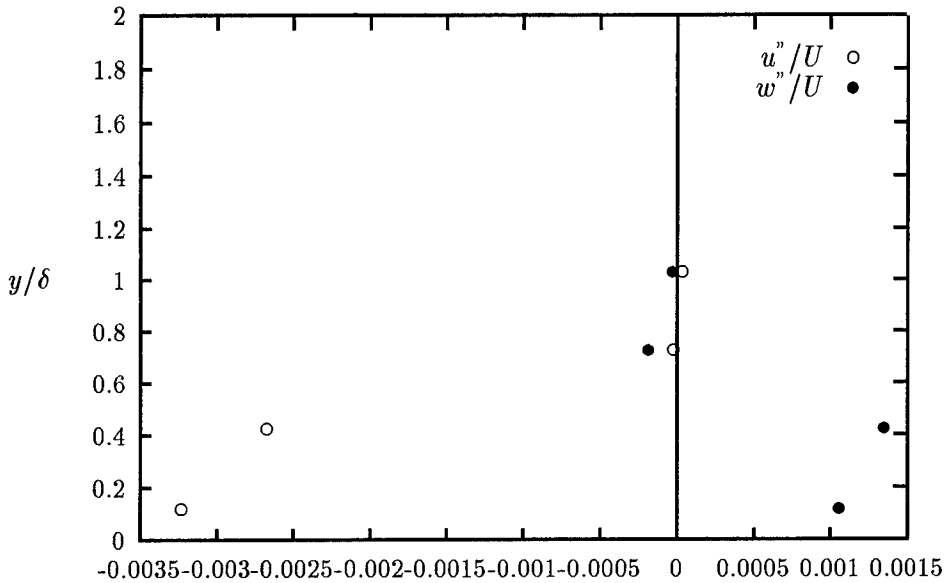


Figure H.3 UW Separated Turbulence Intensities (x = 44 cm)

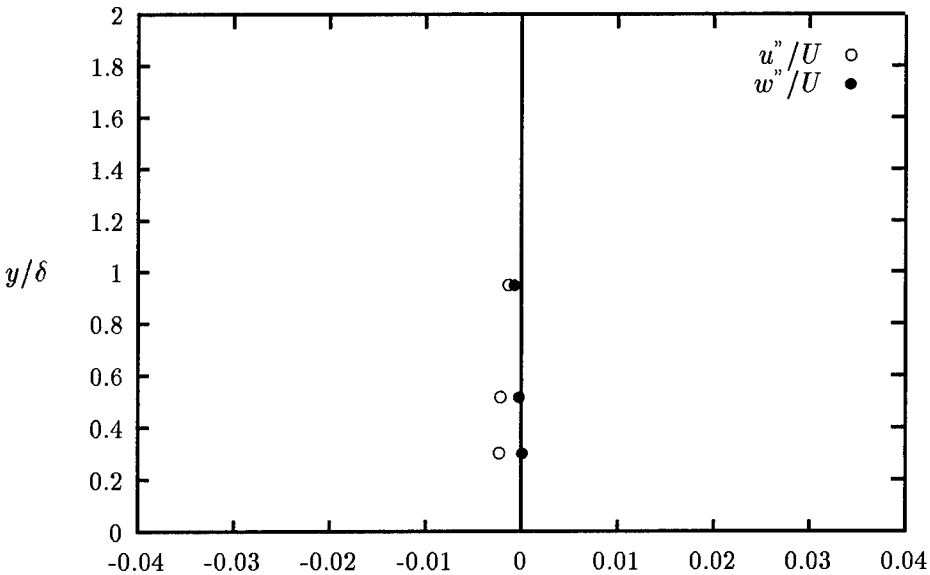


Figure H.4 UW Separated Turbulence Intensities (x = 71.5 cm)

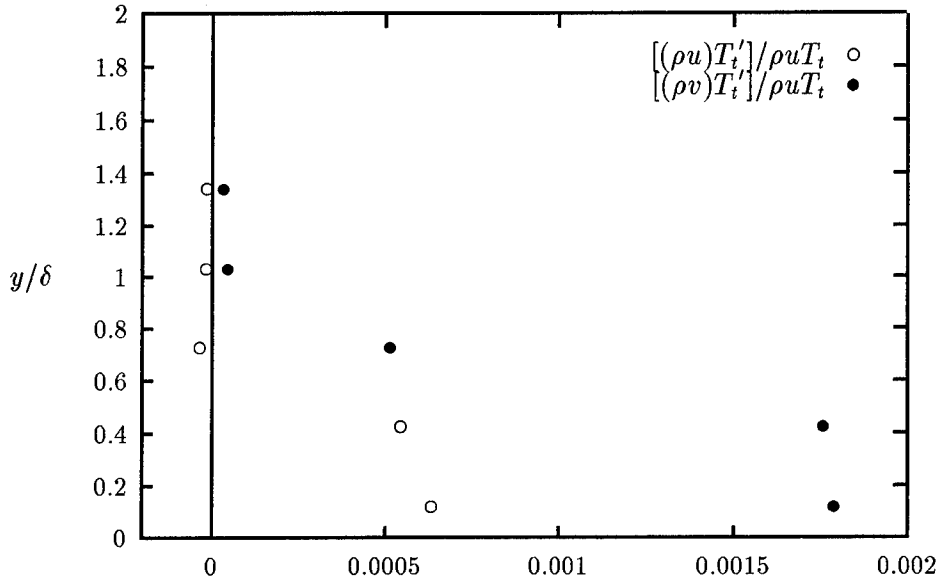


Figure I.1 UV Mass Flux-Total Temperature Correlations (x = 44 cm)

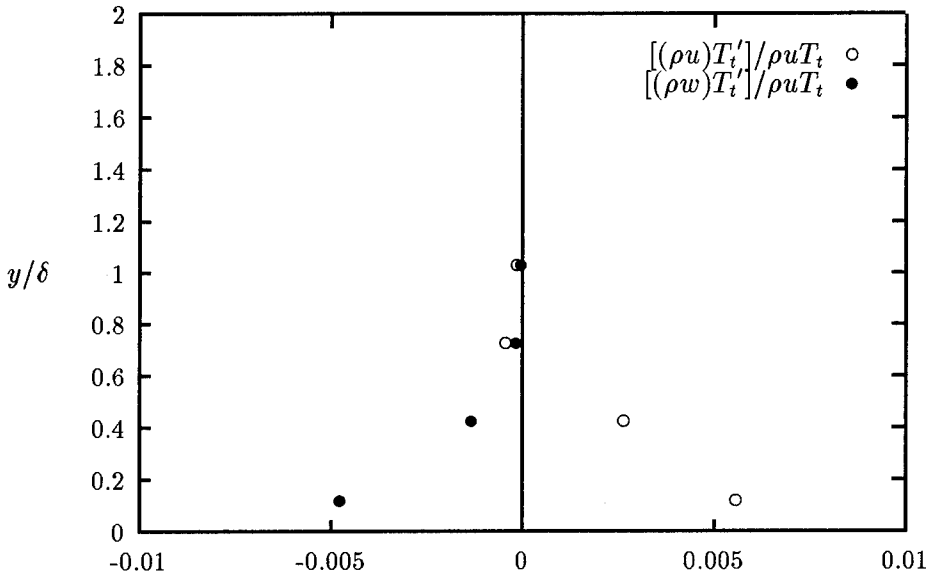


Figure I.2 UW Mass Flux-Total Temperature Correlations (x = 44 cm)

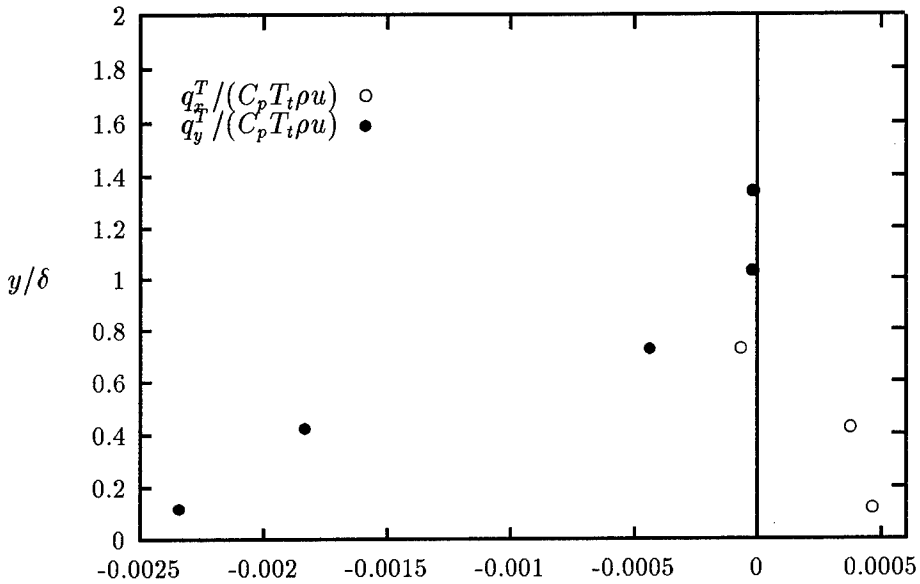


Figure I.3 UV Specific Turbulent Heat Flux (x = 44 cm)

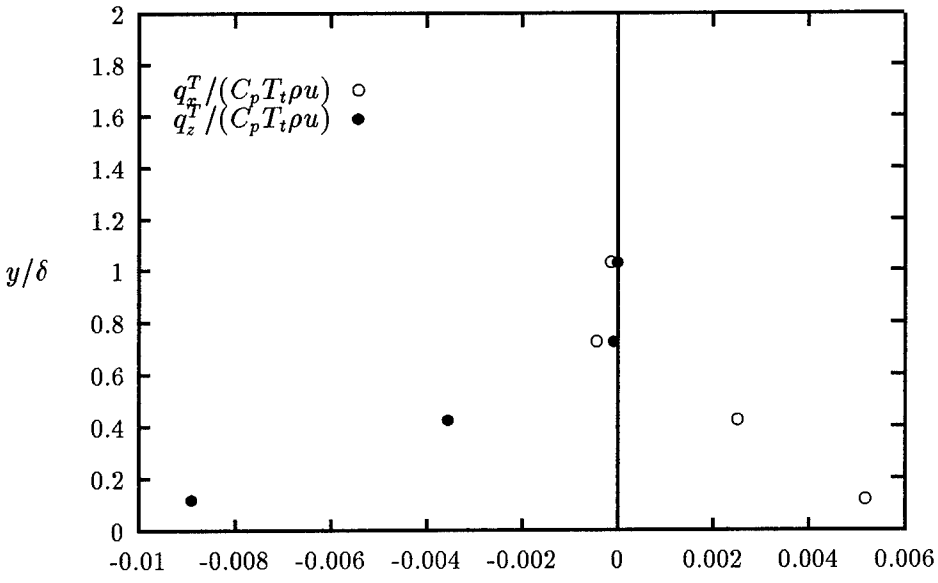


Figure I.4 UW Specific Turbulent Heat Flux (x = 44 cm)

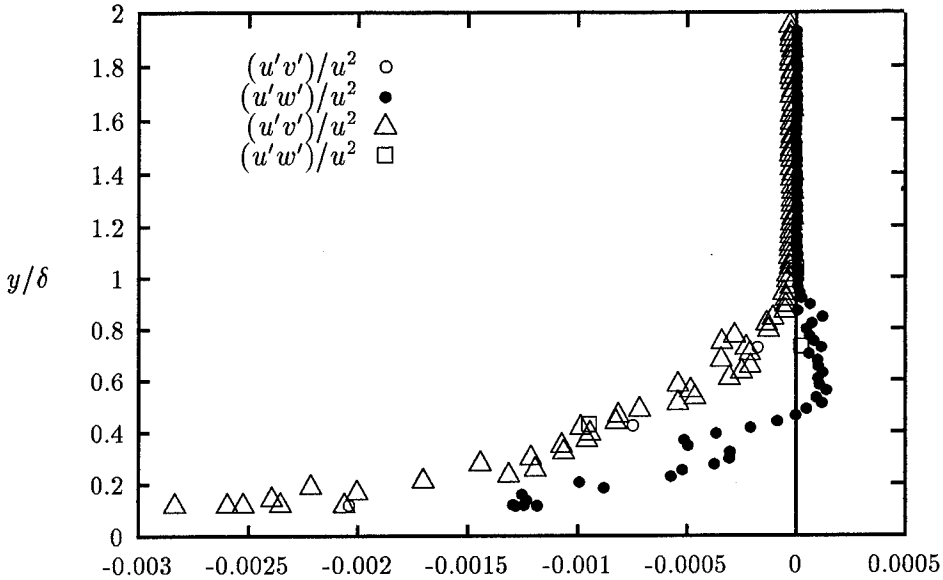


Figure J.1 Turbulence Correlations (x = 44 cm) Velocity-Velocity Correlations

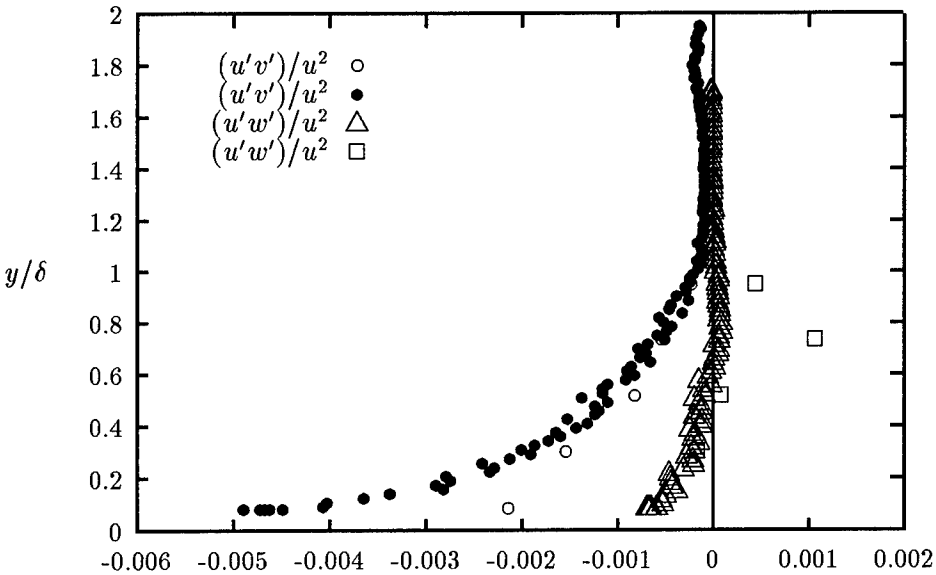


Figure J.2 Turbulence Correlations (x = 71.5 cm) Velocity-Velocity Correlations

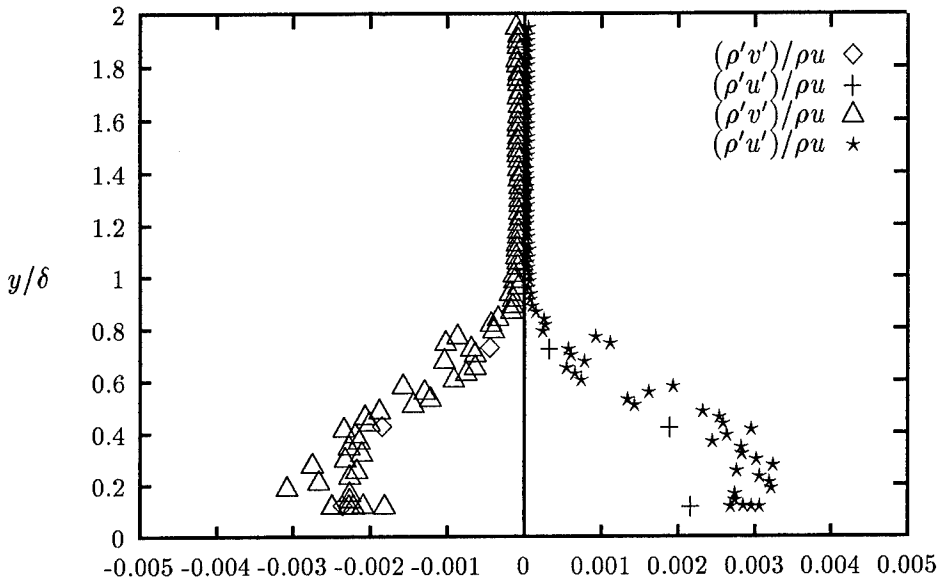


Figure J.3 UV Probe Turbulence Correlations (x = 44 cm) Velocity-Density Correlations

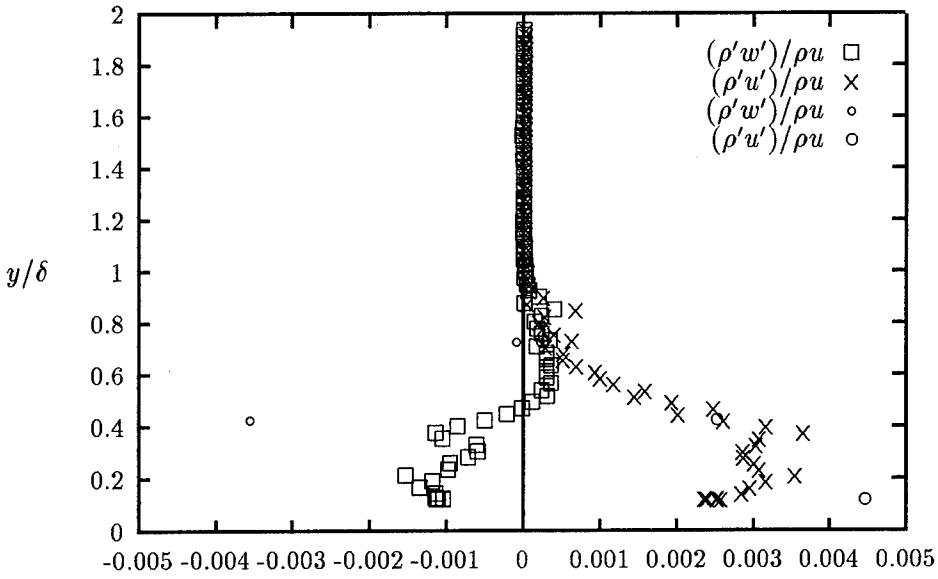


Figure J.4 UW Probe Turbulence Correlations (x = 44 cm) Velocity-Density Correlations

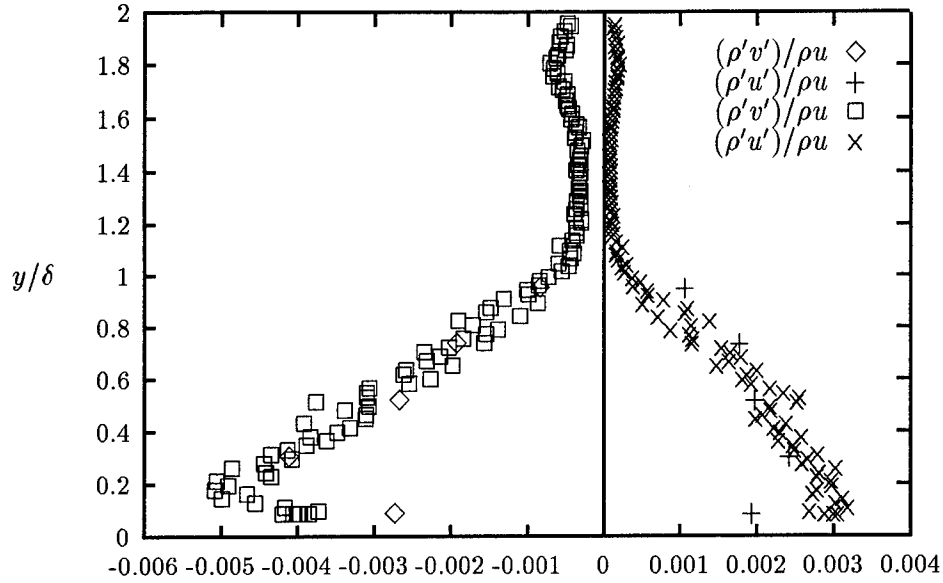


Figure J.5 UV Probe Turbulence Correlations (x = 71.5 cm) Velocity-Density Correlations

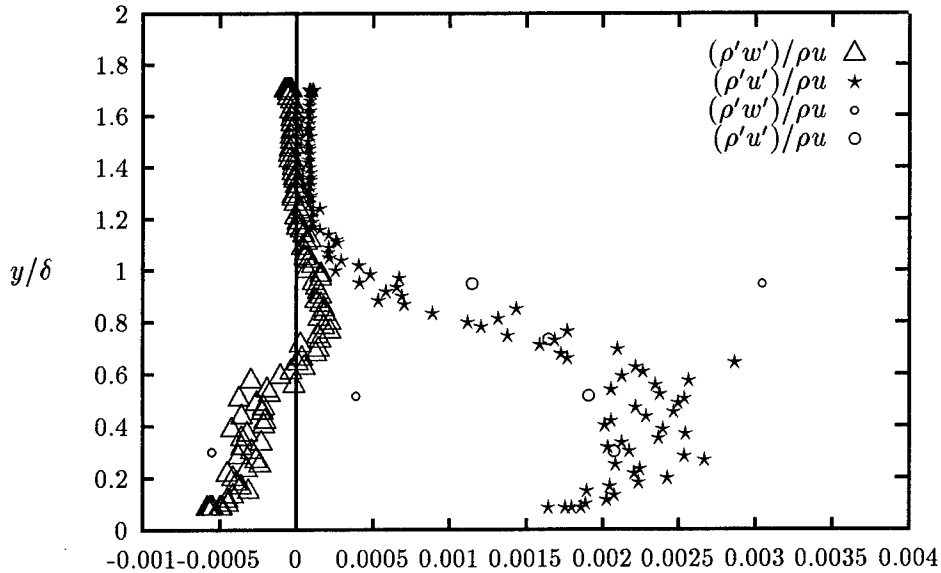


Figure J.6 UW Probe Turbulence Correlations (x = 71.5 cm) Velocity-Density Correlations

## *Appendix K. Procedure*

### *K.1 Mean Flow Data*

The initial reduction of the data was taking the raw Multipro file, which was binary and processing it into an ASCII file using a supplied program by the manufacturer. Although more usable it was in a convoluted form. The essential data contained in these files is the number of data points, the Multipro internal offset value, the Multipro internal slope value, the user entered offset and the user entered slope. The internal file vlaues for the user offset and slope was not used and the calibration values were used in the data reduction. Once these values had been stripped from the file, the data is all that remained. A code was written that took the original ASCII file and constructed a more compact and usable one only containing the data and the above mentioned values. Next, the data upstream was taken at 1.27 cm increments to allow high resolution of the flow. This required five passes through the flow to measure the complete cross section. The data had to be spliced together at the junctures of commonality. Within the aforementioned code was a filter to detect when the LVDT had started and had stopped traversing the flow, at these points the data was spliced together.

### *K.2 SOH Data*

The single overheat data began essentially the same as the mean flow data reduction. The conversion of the Multipro files to a usable ASCII file was done by using the code AsctoAscii.c. The data for the SOH was taken in one traverse step to a distance of approximately two boundary layer thicknesses. This distance was estimated from the shadowgraphs and schlieren photographs. Due to traverse equipment restrictions and the time limit of 21 seconds for the run time of the tunnel the travel distance was usually restricted to below 2.54 cm. The calibration data was obtained, generally on the same run as the data by varying the pressure in the wind tunnel after the probe had stopped traversing. In this manner data acquired on a run was guaranteed to have calibration data available. A script file was written on the Sparc 20's to execute the various data reduction codes. First was the ASCII conversion, second the LVDT data was converted into inches

using the Convert.c code. After the LVDT data was in inches the code LVDTcountandcut.c was used to capture the intervals where the LVDT was moving and count there position in the file and also cut this data out of the overall LVDT data. The count, positions, obtained in this manner were used to cut the other files containing the pressure, and two channel of hot wire data. The code used for this was the Cutfile.c code. The Cutfile.c code had an additional function of cutting the calibration data off of the end of the data files. After the files were cut they were converted to voltages or pressures using the Convert.c program. By cutting the three files, pressure , channel1 hot wire, channel2 hot wire, first, before Convert.c, the reduction time of the data was cut in half. The calibration files were then converted to the appropriate units. Once the calibration files were converted they were converted into files intended for MSHeaR (2).

The format for the MSHeaR calibration file is:

Voltage Pressure($P_{t1}$) Temperature($T_t$) Mach $P_{t2}/P_{t1}$

After this point the calibration files were edited to remove the tunnel unstart data from the files, this is characterized by large fluctuations in data values. The calibration data was very near linear, as it should be in this Mach range. Next the construction of a mean flow data file that matched the data point locations of the SOH data. The program Interpolate.c was used to linearly interpolate the original mean flow data so that the y coordinates matched the SOH data. This was another file required by MSHeaR. The data from the two channels of hot wire data were cross correlated and there mean values and root mean square values were found using the code Xwk.c written by Mike Senseney and Raymond Miller. The original routine was written for Matlab by Mike Senseney and was subsequently rewritten in C by Raymond Miller. This resulted in a conservative estimate of a three time speed increase in the code execution. Next the code MSHeaR was run to obtain the initial turbulence results. Last the code written by Jon Dotter and modified by Raymond Miller was used to separate turbulent variable terms. The code was called separt.f

### *K.3 MOH Data*

Data for the multiple overheat was much harder to reduce than either of the two other data types. A script file was also written to execute most of these steps automatically. First you have a separate calibration data set that may or may not have the resistance levels in the same order as your data file and second, filtering the data is very time consuming. The data is initially broken down the same as the other data, conversion to a usable ASCII form using AsctoAscii.c. The data is then converted to its native form, voltage, etc. because the data had to be viewed to set various data cuting criteria. The method in which the data was triggered made it no longer crucial to base data reduction on the LVDT, but on one of the cross wire channels. The two channels of data from the hot wires were viewed and the more stable, least wildly oscillatory, was used for the cut indexing. This channel was cut on two criteria, first if there was a false jump then a skip first jump switch was set, second the smallest jump between overheat steps was set as teh second criteria. These jumps ranged in value from 0.6 volts up to 4.0 volts typically. Usually the larger was used and then cut down until a satisfactory cut was made. Another adjustment that could be made within Channelcut.c was the number of data points to not use at the end of the step of data. For example if the jump size was set to 4.0 and the data had large jumps in it at the end of the step then the cut at the end of the data would often ignore 350 points and grab the 2056 points that preceed this area. In this way adjustments could be made as to where on the data step, overheat ratio, the data was taken from. Typically the lower the criteria the earlier the initial cut location. By trial and error the calibration files and the data file that was used as a key had to be cut "cleanly". Cleanly meaning no wild oscillations of transition inherent in the data. Once the two channels used as keys were satisfactory the other channels had to be cut using Cutfile.c, same name different algorithm, to match the key channel. These files had to also be viewed to see if further adjustments needed to be made to the cut criteria. The LVDT data was sampled at a lower rate than the pressure or hot wires and therefore had to be expanded to meet there number of data points, this was accomplished using the code Expand.c which takes the frequencies of each channel and expands the file to match. After the LVDT data is expanded it is cut just like the other files.

Once all files have been cut then the calibration files must be sorted. Calibration files were captured on separate runs from the data runs. Sometimes the sequence of resistors was in a different order from the data sequence. The code to separate the calibration data allowed such reordering. The code Calibrate.c constructed the calibration files needed by MSHeaR.

The calibration files are now ready and the interpolated mean flow data is needed. This code is the same as above and does the same linear interpolation of data to match the y locations. The code MSHeaR is run at this point and the function, either option 7 or 8 is used to evaluated the MOH data, 8 was used for all data in this thesis.

A bug when running MSHeaR on Unix systems is that the MOH separation routine needs a space between the title of the output file of option 8 inorder to run option 11 on all data points. Option 11 provided MOH separtion of variables.

### *K.4 Midway*

The results in this section are not valid because the mean flow data was not available. If an adjustment to the mean data or measurements are taken later this data may be highly useful in tracking the flow properties in the wind tunnel. It has been suggested that a delta shift of the 44 cm location mean flow data may render this data useful. Intermediate turbulence measurements are taken 53.5 cm from the nozzle, between the two original upstream station, 44 cm, and the downstream station, 71.5 cm. The measurements are obtained in a zero pressure gradient flat plate section. The only terms measured are the UW single overheat readings. They provide some insight into the nature and progression of the flow. In order to provide direct comparison with the 44 cm location, data is non-dimensionalized using the the conventional probe values from the 44 cm location, i.e. Mach number, etc. The turbulence intensities, separated turbulence intensities and the shear all increase dramatically, Figures K.1 K.2 and K.3. The component of the shear in the xz plane increased dramatically. The shear, $\tau_{xz}$ has increased from a maximum of 0.003 to a maximum of 0.009, a 3 times increase in magnitude! The UW data at the 53.5 cm cite resembles the UV data at the 44 cm location in magnitude and character. Still it is quit clear that the density fluctuation term is the largest term present according to the

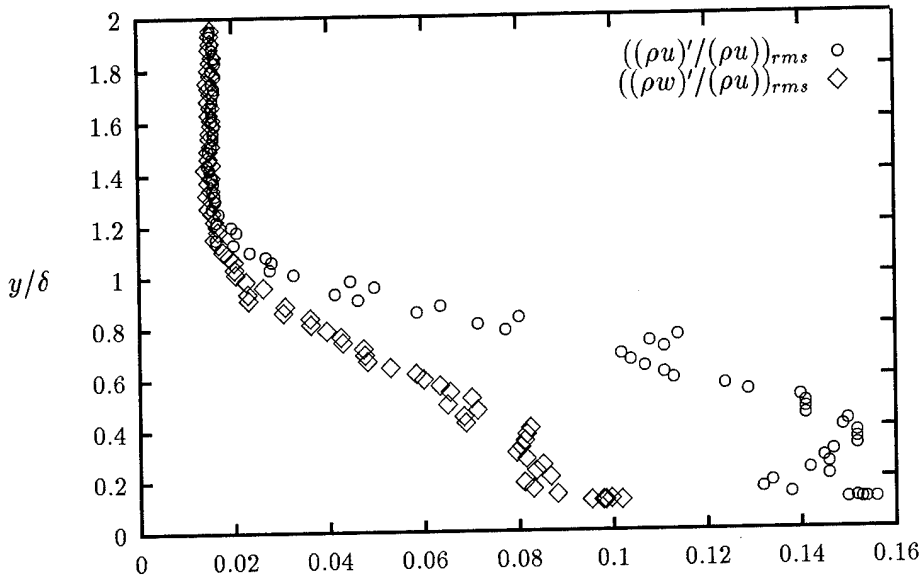


Figure K.1 UW Probe Turbulence Intensities (x = 53.5 cm)

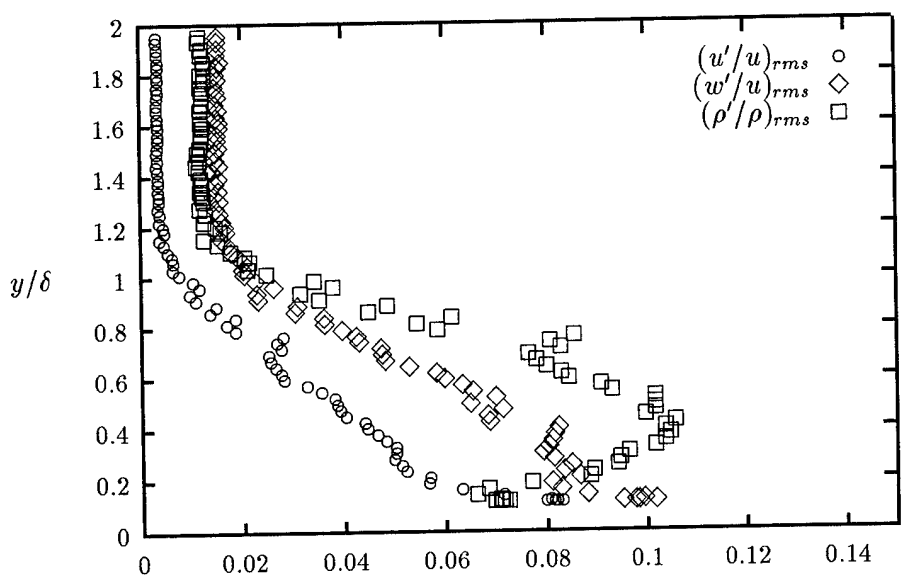


Figure K.2 UW Probe Separated Turbulence Intensities (x = 53.5 cm)

Table K.1 Favré terms from multiple overheat data

| y | Run 009 | Run 010 |
|---|---|---|
| 0.840E-01 | 0.221E-02 | -0.102E+00 |
| 0.301E+00 | 0.145E-02 | 0.289E-03 |
| 0.517E+00 | 0.678E-03 | -0.173E-03 |
| 0.734E+00 | 0.499E-03 | -0.361E-02 |
| 0.950E+00 | 0.129E-03 | -0.137E-02 |

Table K.2 Favré terms from multiple overheat data

| y | 011 | 012 |
|---|---|---|
| 0.119E+00 | 0.209E-02 | – |
| 0.424E+00 | 0.360E-03 | 0.155E-02 |
| 0.728E+00 | 0.155E-04 | 0.439E-04 |
| 0.103E+01 | -0.297E-04 | -0.836E-06 |
| 0.134E+01 | -0.200E-04 | – |

previous description, approximately 67% of the magnitude of the total shear is accounted for in this term. Comparison of the turbulence intensities from the 53.5 cm location to the 71.5 cm location shows more dramatic changes. The 53.5 cm data suggest that the boundary layer is still expanding and the turbulence is getting stronger. The expansion section appears to damp out the turbulence and smooth the flow. The turbulence intensity $((\rho u)'/(\rho u))_{rms}$ has decreased from a peak value of 0.14 to 0.10 when traveling through the expansion ramp. Recall that the 53.5 cm location is non-dimensionlized with the 44 cm data freestream values. The separated values show a similar trend. An increase in magnitude from the 44 cm section, but then a sharp decrease in the 71.5 cm section when exposed to the expansion ramp. Once again, this demonstrates a favorable pressure gradient damps the turbulence in a flow.

The comparison of the shear for the 53.5 cm section to the 71.5 cm section shows a more drastic decrease in the shear value from a maximum of almost 0.009 to approximately 0.0013, almost a 7 fold decrease in spanwise turbulence.

### *K.5 Tables of Favré and Reynolds Shear Terms*

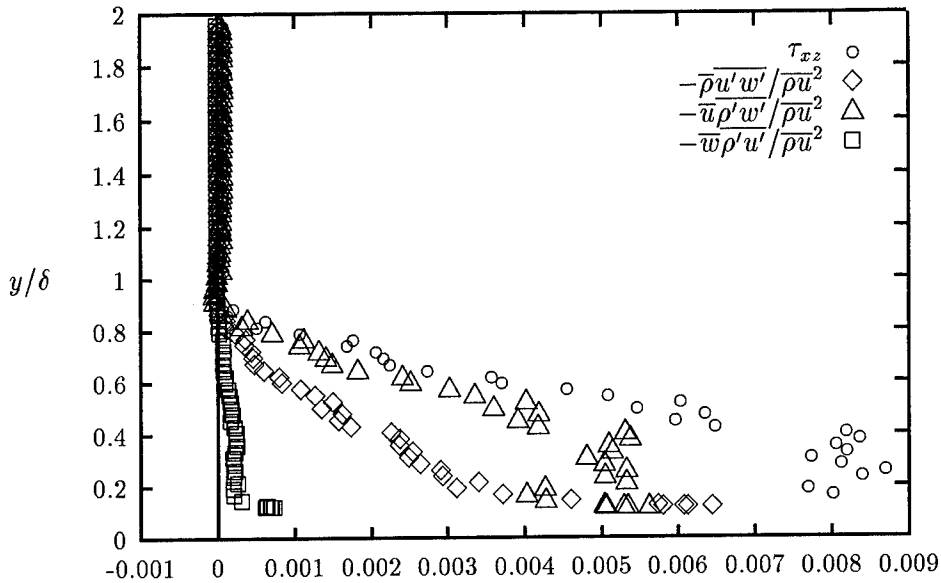


Figure K.3 UW Probe Shear (x = 53.5 cm)

Table K.3 Reynolds terms from multiple overheat data

| y | 011 | 012 |
|---|---|---|
| 0.119E+00 | 0.373E-02 | 0.914E-02 |
| 0.424E+00 | 0.215E-02 | 0.304E-02 |
| 0.728E+00 | 0.595E-03 | -0.137E-03 |
| 0.103E+01 | 0.557E-04 | -0.265E-04 |
| 0.134E+01 | 0.448E-04 | – |

Table K.4 Reynolds terms from multiple overheat data

| y | Run 009 | Run 010 |
|---|---|---|
| 0.840E-01 | 0.404E-02 | -0.704E-01 |
| 0.301E+00 | 0.441E-02 | 0.468E-03 |
| 0.517E+00 | 0.274E-02 | -0.333E-03 |
| 0.734E+00 | 0.187E-02 | -0.438E-02 |
| 0.950E+00 | 0.864E-03 | -0.198E-02 |

*Bibliography*


1. Anderson, J. D. *Modern Compressible Flow with Historical Perspective* ($1^{st}$ ed. Edition). New York: McGraw Hill Inc., 1984.
2. Bowersox, R. *Compressible Turbulence in a High-Speed High Reynolds Number Mixing Layer*. PhD dissertation, Virginia Polytechnic Institute and State University, 1992.
3. Bowersox, R. "Thermal Anemometry." *Handbook of Fluid Dynamics*, edited by J. Schetz and W. Fuhs. John Wiley, 1995.
4. Bowersox, R. and J.A. Schetz. "Compressible Turbulence Measurements in a High-Speed High-Reynolds-Number Mixing Layer," *AIAA Journal*, *32*(4):758 – 764 (April 1994).
5. Clauser, F. "Turbulent Boundary Layers in Adverse Pressure Gradients," *Journal of the Aeronautical Sciences*, 91 – 108 (February 1954).
6. G., Settles and L. Dodson. "Supersonic and Hypersonic Shock/Boundary-Layer Interaction Database," *AIAA Journal*, *32*(7):1377 – 1383 (July 1994).
7. Kistler, A. "Fluctuation Measurements in a Supersonic Turbulent Boundary-Layer," *Physics of Fluids*, *2*(3):290–296 (1959).
8. Kolmogoroff, A. N. "Kolmogoroff's Theory of Locally Isotropic Turbulence," *C.R. Acad. Sci. U.R.S.S.*, *30*:301 – 305 (1941).
9. Liou, W. W. and T. H. Shih. *On the Basic Equations for the Second-Order Modeling of Compressible Turbulence*. Technical Memorandum 105277, NASA, October 1991.
10. Marvin, Joseph G. "Turbulence Modeling for Computational Aerodynamics," *AIAA Journal*, *21*(7):941 – 955 (July 1983).
11. Morkovin, M. "Effects of High Acceleration on a Turbulent Supersonic Shear Layer," *Proceedings of the Heat Transfer and Fluid Mechanics Institute*, *4*:1–17 (1955).
12. Morkovin, M. "Effects of Compressibility on Turbulent Flows," *AGARD*, *4*:368–380 (1961).
13. Press, W., et al. *Numerical Recipes in C* (1st ed. Edition). New York: Cambridge University Press, 1988.
14. Smits, A and K. C. Muck. "Three Shock Wave Turbulent Boundary Layer Interactions," *Journal of Fluid Mechanics*, *182*(10):291 – 314 (June 1987).
15. Staff. *The Temperature Handbook*. Stamford, CT: Omega Engineering, Inc, 1990.
16. Tapley, B. D. *Eshbach's Handbook of Engineering Fundamentals* (4th ed. Edition). New York: John Wiley and Sons Inc, 1990.
17. Volluz, R. *Handbook of Supersonic Aerodynamics*. Technical Report, NAVORD Report 1988, 1961.
18. White, F. M. *Viscous Fluid Flow* (2nd ed. Edition). New York: McGraw-Hill, Inc., 1991.

*Vita*

Captain Raymond S. Miller [redacted]. He graduated from Prescott High School in May of 1980 and entered active Air Force on September 23, 1981. He spent his first five and a half years in the Air Force in the nuclear munitions maintenance field, working up to the position of crew chief and later, became head of munitions control. During that time he was awarded first termer of the quarter in 1983, maintenance person of the quarter in 1984 and 1985, and maintenance person of the year for the year of 1985. He was awarded Senior Airman below the zone and attained the rank of SSgt in three years and two months. He was selected for the Airman Education and Commissioning Program in 1987, and attended Arizona State University in Tempe, Arizona graduating with a BS in Aerospace Engineering. Captain Miller was commissioned on April 24, 1990 and he was subsequently assigned to the 544 Strategic Intelligence Wing at Offutt AFB, NE. He worked on Scud flight analysis during Desert Storm as well as many other projects to decrease the turn around time for analysis of foreign missile system capabilities. During this period he served as the point of contact for implementation of the new inter-continental ballistic missile Early Warning System Algorithm. He received special mention for his work during the IG inspection for his work in these areas. He entered the School of Engineering, Air Force Institute of Technology in May 1993. He completed three sequences of study which were: Finite Element Analysis, Materials, and Computational Fluid Mechanics. His follow-on assignment will be at Robins AFB, where he will be working on the modernization program for the F-15.

Permanent address: [redacted]

# REPORT DOCUMENTATION PAGE

Form Approved
OMB No. 0704-0188

Public reporting burden for this collection of information is estimated to average 1 hour per response, including the time for reviewing instructions, searching existing data sources, gathering and maintaining the data needed, and completing and reviewing the collection of information. Send comments regarding this burden estimate or any other aspect of this collection of information, including suggestions for reducing this burden, to Washington Headquarters Services, Directorate for Information Operations and Reports, 1215 Jefferson Davis Highway, Suite 1204, Arlington, VA 22202-4302, and to the Office of Management and Budget, Paperwork Reduction Project (0704-0188), Washington, DC 20503.

| 1. AGENCY USE ONLY (Leave blank) | 2. REPORT DATE | 3. REPORT TYPE AND DATES COVERED |
|---|---|---|
| | December 13, 1994 | Master's Thesis |

**4. TITLE AND SUBTITLE**
COMPRESSIBLE TURBULENCE MEASUREMENTS IN A SUPERSONIC BOUNDARY LAYER INCLUDING FAVORABLE PRESSURE GRADIENT EFFECTS

**5. FUNDING NUMBERS**

**6. AUTHOR(S)**
Raymond S. Miller

**7. PERFORMING ORGANIZATION NAME(S) AND ADDRESS(ES)**
Air Force Institute of Technology, WPAFB OH 45433-6583

**8. PERFORMING ORGANIZATION REPORT NUMBER**
AFIT/GAE/ENY/94D-19

**9. SPONSORING/MONITORING AGENCY NAME(S) AND ADDRESS(ES)**
Dr James McMichael
AFOSR/NA
Wright Patterson AFB, OH 45433-6583

**10. SPONSORING/MONITORING AGENCY REPORT NUMBER**

**11. SUPPLEMENTARY NOTES**

**12a. DISTRIBUTION/AVAILABILITY STATEMENT**
Distribution Unlimited

**12b. DISTRIBUTION CODE**

**13. ABSTRACT** (Maximum 200 words)


## Abstract

The effect of a favorable pressure gradient on the turbulent flow structure in a Mach 2.9 boundary layer ($R_e/m \approx 1.5 \times 10^7$) is investigated experimentally. Conventional flow and hot film measurements of turbulent fluctuation properties have been made upstream of and along an expansion ramp. Upstream measurements were taken in a zero pressure gradient boundary layer 44 cm from the nozzle throat in a 6.35 cm square test section. Measurements are obtained in the boundary layer, above the expansion ramp, 71.5 cm from the nozzle throat. Mean flow and turbulent flow characteristics are measured in all three dimensions. Comparisons are made between data obtained using single and multiple-overheat cross-wire anemometry as well as conventional mean flow probes. Conventional flow measurements were taken using a Pitot probe and a 10 degree cone static probe. Flow visualization was conducted via imaging techniques (Schlieren and shadowgraph photographs). Results suggest that compressibility effects, as seen through the density fluctuations in the Reynolds shear stress are roughly 10% relative to the mean velocity and are large relative to the velocity fluctuations. This is also observed in the total Reynolds shear stress; compressibility accounts for $50-75\%$ of the total shear. This is particularly true in the favorable pressure gradient region, where though the peak fluctuation intensities are diminished, the streamwise component of the mean flow is larger, hence the contribution of the compressibility term, $\overline{u\rho' v'}$, is significant in the Reynolds shear.


**14. SUBJECT TERMS**
Turbulent Flow, Mach 3, Favorable Pressure Gradient, Hot-Wire Anemometry, Separated Turbulence Quantities

**15. NUMBER OF PAGES**
114

**16. PRICE CODE**

| 17. SECURITY CLASSIFICATION OF REPORT | 18. SECURITY CLASSIFICATION OF THIS PAGE | 19. SECURITY CLASSIFICATION OF ABSTRACT | 20. LIMITATION OF ABSTRACT |
|---|---|---|---|
| UNCLASSIFIED | UNCLASSIFIED | UNCLASSIFIED | UL |

NSN 7540-01-280-5500

Standard Form 298 (Rev. 2-89)
Prescribed by ANSI Std Z39-18
298-102